3-26-2015

Dynamic Response Analysis of an Icosahedron Shaped Lighter Than Air Vehicle

Lucas W. Just

DYNAMIC RESPONSE ANALYSIS OF AN ICOSAHEDRON SHAPED LIGHTER THAN AIR VEHICLE

THESIS
MARCH 2015

Lucas W. Just, Captain, USAF

AFIT-ENY-MS-15-M-216

DEPARTMENT OF THE AIR FORCE
AIR UNIVERSITY

AIR FORCE INSTITUTE OF TECHNOLOGY

Wright-Patterson Air Force Base, Ohio

AFIT-ENY-MS-15-M-216

DYNAMIC RESPONSE ANALYSIS OF AN ICOSAHEDRON SHAPED LIGHTER THAN AIR VEHICLE

THESIS

Presented to the Faculty

Department of Aeronautics and Astronautics

Graduate School of Engineering and Management

Air Force Institute of Technology

Air University

Air Education and Training Command

In Partial Fulfillment of the Requirements for the

Degree of Master of Science in Aeronautical Engineering

Lucas W. Just, BS

Captain, USAF

March 2015

AFIT-ENY-MS-15-M-216

DYNAMIC RESPONSE ANALYSIS OF AN ICOSAHEDRON SHAPED LIGHTER THAN AIR VEHICLE

Lucas W. Just, BS
Captain, USAF

Committee Membership:

Dr. Anthony Palazotto
Chair

Dr. Marina Ruggles-Wrenn
Member

Lt. Col. Anthony M. Deluca, PhD
Member

AFIT-ENY-MS-15-M-216

Abstract

The creation of a lighter than air vehicle using an inner vacuum instead of a lifting gas is considered. Specifically, the icosahedron shape is investigated as a design that will enable the structure to achieve positive buoyancy while resisting collapse from the atmospheric pressure applied. This research analyzes the dynamic response characteristics of the design, and examines the accuracy of the finite element model used in previous research by conducting experimental testing. The techniques incorporated in the finite element model are confirmed based on the experimental results using a modal analysis. The experimental setup designed will allow future research on the interaction between the frame and skin of icosahedron like structures using various combinations of materials and construction methods. Additionally, a *snapback* behavior observed in previous static response analysis is further investigated to determine nonlinear instability issues with the design. Dynamic analysis of the structure reveals chaotic motion is present in the frame of the icosahedron under certain loads and boundary conditions. These findings provide information critical to the design of an icosahedron shaped lighter than air vehicle using an inner vacuum.

Acknowledgments

I would like to thank Dr. Palazotto for his unending support throughout the research process. He was continuously available and provided expertise during all phases of the thesis, and without him none of it would have been possible. Also, the help of Brian Cranston and Ruben Adorno-Rodriguez was greatly appreciated. Dr. Cobb and Mr. Anderson have my gratitude in helping to build and setup the experimental portion of the research. Without them, that portion of the research certainly could not have been completed. I would like to thank Dr. Wolf, of Cooper Union in New York, for his time explaining the concept of chaos and his guidance on the determination of it in a system. Thank you Dr. Ruggles-Wrenn and Lt. Col. Deluca for taking your time providing recommendations to make this thesis better, and for all of the work that is required of a committee member. Finally, thanks to Dr. Stargel of AFOSR for giving an interest in the subject and providing the funding necessary to complete the research.

Lucas W. Just

Table of Contents

Page

Abstract iv
Acknowledgments v
Table of Contents vi
List of Figures viii
List of Tables xii
Nomenclature xiii
I. Introduction 1
Chapter Overview 1
Objective 1
Motivation 2
Background 4
Methodology 5
Overview 6
II. Theory 8
Chapter Overview 8
Previous Research of LTAV Subjected to Vacuum 8
Finite Element Analysis and the Dynamic Response 17
Frequency Response Functions and Power Spectral Density Functions 22
Chaotic Behavior 25
Summary 30
III. Model Development 31
Chapter Overview 31
Icosahedron Design 31

Decomposition of Icosahedron....35
Experimental Test Setup....41
Equivalent Stiffness Study....49
Time Step Study....53
Summary....58
IV. Analysis and Results....59
Chapter Overview....59
Experimental Results....59
Chaotic Behavior Analysis....72
Load Rate Analysis....75
Icosahedron Frame Boundary Condition Three....82
Icosahedron Frame Boundary Condition Two....93
Icosahedron Frame and Skin Boundary Condition Three....101
Summary....107
V. Conclusions and Recommendations....109
Chapter Overview....109
Conclusions of Research....109
Significance of Research....111
Recommendations for Future Research....111
Appendix....113
Bibliography....127

List of Figures

Page

Figure 1: Forces Acting on Half-Sphere 10

Figure 2: Icosahedron Frame (on Right) with Membrane Skin (on Left)..... 13

Figure 3: Beam Cross-section for Icosahedron Frame 14

Figure 4: Applied Pressure versus Max Von Mises Stress for the Frame 15

Figure 5: Applied Pressure versus Max Von Mises Stress for the Skin 16

Figure 6: Single Pendulum System (Top) and Phase-plane Trajectory (Bottom) 26

Figure 7: Double Pendulum System with Different Initial Conditions (Left) and the Trajectories of the Two Points Corresponding to Each System (Right) 27

Figure 8: Phase Space Diagram of Single Pendulum Motion Decaying to *Attractor* 28

Figure 9: Abaqus View of Baseline Icosahedron Frame 32

Figure 10: Abaqus View of Baseline Icosahedron with Skin 33

Figure 11: Degrees of Freedom for Shell and Membrane Elements 34

Figure 12: Decomposition of Standalone Frame Model 36

Figure 13: Decomposition of Frame-Skin Model 36

Figure 14: Illustration of Pseudo-clamped Boundary Condition and Elastic Foundation 42

Figure 15: Abaqus Representation of Experimental Test Specimen without Membrane (Left) and with Membrane (Right) 43

Figure 16: Experimental Setup 47

Figure 17: Test Specimen – Frame Only (Left) and Frame-Skin (Right)..... 47

Figure 18: Experimental Analysis Process 48

Figure 19: Equivalent Stiffness Comparison Process 50

Figure 20: Mode Shape Difference for Icosahedron Frame and Equivalent Stiffness Beam 52
Figure 21: Similar Mode Shapes for Icosahedron Frame and Equivalent Stiffness Beam 52
Figure 22: Boundary Conditions and Initial Displacement for Time Step Study 54
Figure 23: Displacement versus Time for First Four Time Step Values 56
Figure 24: Displacement versus Time for Last Three Time Step Values 56
Figure 25: PSD for Time Step of 1e-4 seconds 57
Figure 26: PSD for Time Step of 1e-6 Seconds 57
Figure 27: Modes 1 through 6 – FEA Experimental Triangle (Frame) 60
Figure 28: Points of Measurement for Experimental Triangle 61
Figure 29: Experimental Triangle Mode Shapes and Natural Frequencies (Frame) 62
Figure 30: Frequency Response Plot for Experimental Triangle (Frame) 63
Figure 31: Mode Shapes Associated with Experimental Triangle 66
Figure 32: Modes 1 through 8 – FEA Experimental Triangle (Frame-Skin) 67
Figure 33: Experimental Triangle Mode Shapes and Natural Frequencies (Frame-Skin) 69
Figure 34: Frequency Response Plot for Experimental Triangle (Frame-Skin) 70
Figure 35: Mode Shapes Associated with Experimental Triangle with Skin 72
Figure 36: *Snapback* Behavior Observed in Unsymmetrical Boundary Conditions 74
Figure 37: Boundary Condition and Load Applied for Load Study 76
Figure 38: Follower Force (Left) and Non-follower Force (Right) 77
Figure 39: Various Loading Conditions for Load Study 78
Figure 40: Displacement versus Time Curves for Various Loading Conditions 78
Figure 41: Loads above *Snapping* Load 80

Figure 42: Displacement versus Time Curves above *Snapping* Load 81

Figure 43: Load 1, BC3, $\boldsymbol{\lambda_1}$= -0.0121 bits/orbit, Displacement Curve 84

Figure 44: Load 1, BC3, $\boldsymbol{\lambda_1}$= -0.0121 bits/orbit, Phase Plane Trajectory 84

Figure 45: Load 1, BC3, $\boldsymbol{\lambda_1}$= -0.0121 bits/orbit, PSD 85

Figure 46: Load 1, BC3, $\boldsymbol{\lambda_1}$= -0.0121 bits/orbit, Lyapunov Exponent Convergence Plot 85

Figure 47: Delay Reconstructed *Attractor* for Load 1, BC3, $\boldsymbol{\lambda_1}$= -0.0121 bits/orbit..... 87

Figure 48: Load 2, BC3, $\boldsymbol{\lambda_1}$= -0.0137 bits/orbit, Displacement Curve 88

Figure 49: Load 2, BC3, $\boldsymbol{\lambda_1}$= -0.0137 bits/orbit, Phase Plane Trajectory 88

Figure 50: Load 2, BC3, $\boldsymbol{\lambda_1}$= -0.0137 bits/orbit, PSD 89

Figure 51: Load 2, BC3, $\boldsymbol{\lambda_1}$= -0.0137 bits/orbit, Lyapunov Exponent Convergence Plot 89

Figure 52: Load 3, BC3, $\boldsymbol{\lambda_1}$= 3.8814 bits/orbit, Displacement Curve 91

Figure 53: Load 3, BC3, $\boldsymbol{\lambda_1}$= 3.8814 bits/orbit, Phase Plane Trajectory 91

Figure 54: Load 3, BC3, $\boldsymbol{\lambda_1}$= 3.8814 bits/orbit, PSD 92

Figure 55: Load 3, BC3, $\boldsymbol{\lambda_1}$= 3.8814 bits/orbit, Lyapunov Exponent Convergence Plot 92

Figure 56: Load 4, BC2, $\boldsymbol{\lambda_1}$= 0.303 bits/orbit, Displacement Curve 94

Figure 57: Load 4, BC2, $\boldsymbol{\lambda_1}$= 0.303 bits/orbit, Phase Plane Trajectory 95

Figure 58: Load 4, BC2, $\boldsymbol{\lambda_1}$= 0.303 bits/orbit, PSD 95

Figure 59: Load 4, BC2, $\boldsymbol{\lambda_1}$= 0.303 bits/orbit, Lyapunov Exponent Convergence Plot .. 96

Figure 60: Load 5, BC2, $\boldsymbol{\lambda_1}$= 0.371 bits/orbit, Displacement Curve 96

Figure 61: Load 5, BC2, $\boldsymbol{\lambda_1}$= 0.371 bits/orbit, Phase Plane Trajectory 97

Figure 62: Load 5, BC2, $\boldsymbol{\lambda_1}$= 0.371 bits/orbit, PSD 97

Figure 63: Load 5, BC2, $\boldsymbol{\lambda_1}$= 0.371 bits/orbit, Lyapunov Exponent Convergence Plot .. 98

Figure 64: Load 6, BC2, $\boldsymbol{\lambda_1}$= 19.67 bits/orbit, Displacement Curve 99

Figure 65: Load 6, BC2, $\boldsymbol{\lambda_1}$= 19.67 bits/orbit, Phase Plane Trajectory 99

Figure 66: Load 6, BC2, $\boldsymbol{\lambda_1}$= 19.67 bits/orbit, PSD 100

Figure 67: Load 6, BC2, $\boldsymbol{\lambda_1}$= 19.67 bits/orbit, Lyapunov Exponent Convergence Plot 100

Figure 68: Load 7, BC3, $\boldsymbol{\lambda_1}$= -0.00291 bits/orbit, Displacement Curve 102

Figure 69: Load 7, BC3, $\boldsymbol{\lambda_1}$= -0.00291 bits/orbit, Phase Plane Trajectory 103

Figure 70: Load 7, BC3, $\boldsymbol{\lambda_1}$= -0.00291 bits/orbit, PSD 103

Figure 71: Load 7, BC3, $\boldsymbol{\lambda_1}$= -0.00291 bits/orbit, Lyapunov Exponent Convergence Plot 104

Figure 72: Load 8, BC3, $\boldsymbol{\lambda_1}$= -0.0119 bits/orbit, Displacement Curve 104

Figure 73: Load 8, BC3, $\boldsymbol{\lambda_1}$= -0.0119 bits/orbit, Phase Plane Trajectory 105

Figure 74: Load 8, BC3, $\boldsymbol{\lambda_1}$= -0.0119 bits/orbit, PSD 105

Figure 75: Load 8, BC3, $\boldsymbol{\lambda_1}$= -0.0119 bits/orbit, Lyapunov Exponent Convergence Plot 106

Figure 76: Delay Reconstructed *Attractor* for Load 7, BC3, $\boldsymbol{\lambda_1}$= -0.00291 bits/orbit ... 106

List of Tables

Page

Table 1: Baseline Icosahedron Dimensionality 33

Table 2: Eigenvalues for Icosahedron Frame Decomposition – Triangle 38

Table 3: Eigenvalues for Icosahedron Frame Decomposition – Beam..... 38

Table 4: Eigenvalues for Icosahedron Frame and Skin Decomposition – Triangle with Beams and Skin..... 39

Table 5: Eigenvalues for Icosahedron Frame and Skin Decomposition – Triangle Skin. 40

Table 6: Experimental Triangle Dimensionality..... 45

Table 7: Natural Frequencies for Equivalent Stiffness Beam..... 51

Table 8: Analytical and Abaqus Calculated Natural Frequencies for Simple Beam..... 54

Table 9: PSD Calculated Natural Frequencies for Simple Beam 55

Table 10: Natural Frequencies of FEA Experimental Triangle Frame, Experimental Triangle Frame, and FEA Icosahedron Frame 65

Table 11: Eigenvalues of FEA Experimental Triangle Frame, Experimental Triangle Frame, and FEA Icosahedron Frame 71

Table 12: Loading Rates for Applied Pressure 82

Table 13: Lyapunov Exponent for Different Applied Loads..... 107

Nomenclature

Symbol	Description
A	Beam Cross-Sectional Area
AFIT	Air Force Institute of Technology
B	Buoyancy
BC	Boundary Condition
BCE	Before Current Era
c	Beam Thickness-to-Radius Ratio
C	Damping Matrix
CAD	Computer Aided Design
dt	Time Step
$D, \dot{D}, \ddot{D}$	Displacement, Velocity, and Acceleration Matrices, respectively
DARPA	Defense Advanced Research Projects Agency
DoF	Degree of Freedom
E	Modulus of Elasticity
ft	Feet
f	Function
F	Fourier Transform of Function
F_b	Buoyant Force
FEA	Finite Element Analysis
FEM	Finite Element Model
g	Acceleration of Gravity
GPa	Gigapascal
G	Frequency Response Function
HULA	Hybrid Ultra Large Aircraft
Hz	Hertz
in	Inches
I	Area Moment of Inertia
K	Stiffness Matrix
Kg	Kilogram
KPa	Kilopascal
l_{beam}	Beam Length
lb	Pound
L	Beam Length
L_p	Length Between Two Points in Reconstructed *Attractor*
$L_p{}'$	Evolved Length Between Two Points in Reconstructed *Attractor*
LTAV	Lighter Than Air Vehicle
m	Meter
M	Mass Matrix
MATLAB	Matrix Laboratory
MAV	Micro Air Vehicle
MPa	Megapascal
n	Mode Number
N	Number of Replacement Points

p	Ellipsoidal Principal Axis
P_a	Applied Pressure
$P_{air,i}$	Inner Air Pressure
$P_{air,o}$	Outer Air Pressure
P_{crit}	Critical Pressure
Pa	Pascal
PSD	Power Spectral Density
r	Icosahedron Radius
r_{beam}	Beam Radius
R	Sphere radius
RBM	Rigid Body Mode
R^*	Air Specific Gas Constant
R^{ext}	Externally Applied Load Vector
R^{int}	Internal Force Vector
R_x	Autocorrelation Function
s	Seconds
S_y	Yield Strength
S_x	Power Spectral Density Function
t_{beam}	Beam Thickness
t_{shell}	Shell Thickness
t	Time
$T_{air,i}$	Inner Air Temperature
$T_{air,o}$	Outer Air Temperature
u	X-axis Displacement Component
V_r	Reduction in Volume
V_{shell}	Shell Volume
V_{sphere}	Sphere Volume
W_{shell}	Shell Weight
W	Structure Weight
W/B	Weight-to-Buoyancy Ratio
x	System Response as a Function of Time
X	System Response as a Function of Frequency
λ_1	Lyapunov Exponent
ν	Poisson's Ratio
ρ	Density
ρ_a	Air Density
ρ_s	Shell Material Density
ρ_{frame}	Frame Material Density
ρ_{skin}	Skin Material Density
σ	Compressive Stress
τ	Time Delay
ϕ_n	Mode Shape (Eigenvector)
ω	Frequency
ω_n	Natural Frequency (Eigenvalue)

DYNAMIC RESPONSE ANALYSIS OF AN ICOSAHEDRON SHAPED LIGHTER THAN AIR VEHICLE

I. Introduction

Chapter Overview

The creation of a lighter than air vehicle (LTAV) was an important achievement that allowed the human endeavor of flight to be realized. Use of such a vehicle has proven relevant in both civilian and military applications. However, heavier than air vehicles have earned more attention over the past century and become the primary vehicle used in the air, largely due to the technological challenges present with LTAVs. Recently, technological advances have sparked a new interest in the use of LTAVs. Several new concepts have been considered which would increase the utility of LTAVs; of particular interest is the development of a LTAV that generates lift by evacuating the air inside of the structure and creating an inner vacuum.

There are many challenges in developing a vacuum LTAV, some of which this research will investigate. This chapter will describe the objectives for the research, highlight the motivation behind it, investigate the background leading to this point, briefly consider the analysis process to be used, and outline the remainder of the thesis.

Objective

Structures capable of withstanding atmospheric pressures with an inner vacuum have traditionally been designed with very thick walls to resist buckling. However, the typical wall thickness enabling these structures to avoid collapse also significantly increases the weight. Minimization of weight and maximization of structural strength are critical if the

structure is to achieve positive buoyancy. The design of such a structure requires a robust model of which the dynamic response characteristics are of particular interest.

The objectives of this thesis are to gain a better understanding of the dynamic response of an icosahedron shaped LTAV, verify the current model being used, and identify nonlinear instability problems present in the design. Specifically, the research objectives are listed below:

- Identify the inherent dynamic characteristics of the icosahedron LTAV in the form of natural frequencies and mode shapes.
- Determine if a reduced order volume can be designed that is representative of the more complex structure as a whole.
- Verify the computer model of the icosahedron LTAV by conducting an experimental modal analysis of the reduced order volume.
- Characterize the dynamic behavior of the icosahedron LTAV when subjected to various loading scenarios.

Motivation

A LTAV in general would have numerous applications, from military surveillance to civilian transportation. These possibilities have already been exploited by LTAVs using a lifting gas (hydrogen, helium, hot air), but those vehicles require storage for the gas while the vehicle is not in use, and the gas is occasionally in low supply. Additionally, the use of a lifting gas causes a challenging vehicle control problem, which is usually solved by incorporating a heavy ballast system into the vehicle reducing the usable payload [1]. If a vehicle could be developed that required only a vacuum, many of the disadvantages to

existing LTAVs would be alleviated, but no current design can withstand atmospheric pressure and remain light enough to achieve positive buoyancy.

In January 2014, *Popular Mechanics* published an article titled, "Ship of Dreams" that discussed a renewed interest in LTAVs. The article investigates some of the reasons LTAVs became largely irrelevant over the past half century after proving to be useful in the past. Heavy ballast systems that take away from potential payload weight are referenced in addition to technological advancements made by airplanes. The article also states some advantages LTAVs have over airplanes, including cost. It states, "Airships would ultimately cost about a third as much to build as a 747 and would use a third as much fuel" [2]. The knowledge of the cost savings potential LTAVs possess inspired the Defense Advanced Research Projects Agency (DARPA) to start the Walrus Hybrid Ultra Large Aircraft Program (HULA), which "sought to develop an airship that could cover 12,000 nautical miles in seven days, with a payload of at least 450 tons" [2].

The Walrus HULA program investigated the possibility of using LTAVs for transportation, but other uses for a vacuum LTAV can easily be envisioned. A much smaller version could be developed to perform search-and-rescue or surveillance missions. In this regard, the vacuum LTAV would be comparable to the Micro Air Vehicle (MAV), of which much research has been recently conducted.

The creation of a vacuum LTAV would have numerous military and civilian uses, but before any design is manufactured and tested, high fidelity computer models must be created to understand the challenges a vacuum LTAV presents. This thesis seeks to determine what types of analysis techniques are needed to be representative of a real-life LTAV under a vacuum, and how that structure will respond to various loading scenarios.

Background

Humans have taken an interest in flight for millennia, and have been attempting to conquer the air dating back to the invention of the kite by the Chinese around 1000 BCE. These kites were even used to carry men into scout positions to identify enemy troops. From these early beginnings, the evolution of flight took an additional 3,000 years to make another significant advance. In 1783, the Montgolfier brothers successfully achieved flight using a hot-air balloon. While this was not the first time a LTAV had been imagined, it was the first time one had been successfully built and flown [3].

Hot-air balloons are able to stay afloat in the atmosphere by displacing a volume of air whose weight is greater than the balloon assembly itself, creating positive buoyancy [1]. This concept is identical to a boat floating on water with the exception of the medium which the vehicle floats in. Every functional LTAV created has used some type of lifting gas to achieve the ability to float in air by having more buoyant lifting force than weight. Heating the air inside of a balloon decreases the density of the air inside and decreases the total weight of the balloon, while the volume stays the same and therefore the amount of displaced air remains the same. Another approach to creating a LTAV is by filling the inside of the structure with a lifting gas like hydrogen or helium, which creates the same effect as heated air. While this approach allows the structure to be non-rigid, and has proven to work, it also has significant disadvantages.

The same idea of creating lift by displacing more weight than the structure itself weighs can be achieved by removing all gases inside the structure creating a vacuum. During the 17th century, Francesco Lana de Terzi theorized a design that did not use an internal pressure, but instead achieved positive buoyancy by using a vacuum [4]. His

design used copper spheres with a thin outer shell and a vacuum inside, but it was later proven no currently available homogeneous material could withstand the atmospheric pressure, and also be light enough to float [5]. Therefore, some type of rigid support has to be incorporated into the LTAV to avoid structural failure. A. Akhmeteli and A. Gavrilin proposed a design to create a layered shell to "achieve sufficient compressive strength, buckling stability, and positive buoyancy" [5]. Another possibility is to create a frame and skin structure where the frame resists the majority of the atmospheric pressure, while the skin provides stability, and prevents air leakage. An icosahedron frame is an intriguing choice because it has symmetry, simplicity, and is nearly spherical in shape.

This design was considered by T. Metlen and R. Adorno-Rodriguez during previous research at the Air Force Institute of Technology (AFIT) [6] [7]. It consists of an icosahedron frame with a thin membrane-like skin covering the gaps of the frame. An icosahedron is made up of 20 equilateral triangles with 12 vertices where each triangle comes together. This design has been pursued because of its symmetry, and because it is nearly spherical. This allows it to displace larger amounts of fluid for its weight, and distribute equal loading on each member of the frame.

Methodology

A Finite Element Model (FEM) capable of analysis where fast, non-linear, transient effects dominate the solution is required to examine the instability characteristics and dynamic response of the proposed LTAV. Abaqus is the Finite Element Analysis (FEA) computer program used in analyzing the structure, because it is well suited in solving

non-linear problems of this nature. It is used to determine the modal characteristics of the structure and analyze its response to different dynamically applied loads.

The proposed design is composed of an inner rigid frame and an outer membrane-like skin attached to the frame creating an enclosed structure nearly spherical in shape. Initial analysis seeks to obtain the natural frequencies and mode shapes of the structural frame of the LTAV. The skin is then incorporated into the model to give a better understanding of the interaction between the two main components, and reveal the modal response characteristics of the entire model. Computing the eigenvalues and eigenvectors of the complete structure will indicate frequencies likely to cause failure as a harmonic resonance occurs near the natural frequencies which leads to very large oscillations. A decomposition of the complex structure into its simpler parts allows the development of a representative structure that can be constructed and tested. In the case of both the standalone frame and the entire frame-skin model, an experimental test is conducted to verify the FEM. Finally, various loading scenarios are applied to the model to determine the dynamic response and instability characteristics of the structure.

Overview

- Chapter I: States the objective of this thesis, introduces the background and motivation behind it, and develops an analysis plan for completion.
- Chapter II: Review of the theory related to the analysis of the icosahedron shaped LTAV.
- Chapter III: Details the model development and methodology of the analysis and the FEA modeling techniques used.

- Chapter IV: Presents the results of the analysis for the various scenarios considered.
- Chapter V: A summary of the findings and future recommendations.

II. Theory

Chapter Overview

Mechanics can be split into two categories: the first is statics, which studies all of the forces acting in equilibrium; and the second is dynamics, which investigates the structure in motion [8, p. 4]. Previous research of an icosahedron shaped LTAV by Ruben Adorno-Rodriguez and Trent Metlen provides a good understanding of the static response of the structure to atmospheric pressure, and establishes a baseline of the research conducted in this thesis. To better understand the total structural behavior due to various forces, a dynamic response of the LTAV must be examined.

This chapter will provide a summary of the research on an icosahedron shaped LTAV that has been carried out to date, and details the analysis tools and theory used to obtain the dynamic response characteristics of the structure. FEA techniques, modal analysis, and chaotic behavior will be described in this section as they apply to the overall structure.

Previous Research of LTAVs Subject to a Vacuum

While the concept of using a vacuum to achieve positive buoyancy is centuries old, the idea of using an icosahedron frame with a membrane-like skin as a structure is relatively new. Therefore, little literature has been published on the subject. Two theses were previously completed by AFIT students concerning an icosahedron frame structure which can withstand atmospheric pressure and remain light enough to float in air, and they provide a baseline of information for this research. The icosahedron frame concept originated with Trent T. Metlen's investigation of the LTAV "to become viable methods

of transportation" [6, p. iv]. Metlen's thesis research was completed in 2013 and Ruben Adorno-Rodriguez's was completed in 2014. The remainder of this section is largely a summary of the research completed by Metlen and Adorno-Rodriguez.

In the background section of the introduction chapter, it was stated that the optimal shape to achieve positive buoyancy is a sphere. The section stipulates no currently available commercial material formed into a thin-shell sphere can withstand the pressure of the atmosphere if all of the air is evacuated. A brief summary, based on Akhmeteli and Gavrilin's calculations of the equations and reasoning leading to this conclusion follows.

Spheres are symmetric, and the pressure exerted on the sphere under consideration acts uniformly; therefore, half of a sphere can be analyzed using the assumption that each half will see identical internal and external forces. A half-sphere with the static forces is shown in Figure 1 [5]. In the figure, σ represents the compressive stress and P_a represents the externally applied pressure acting on the sphere.

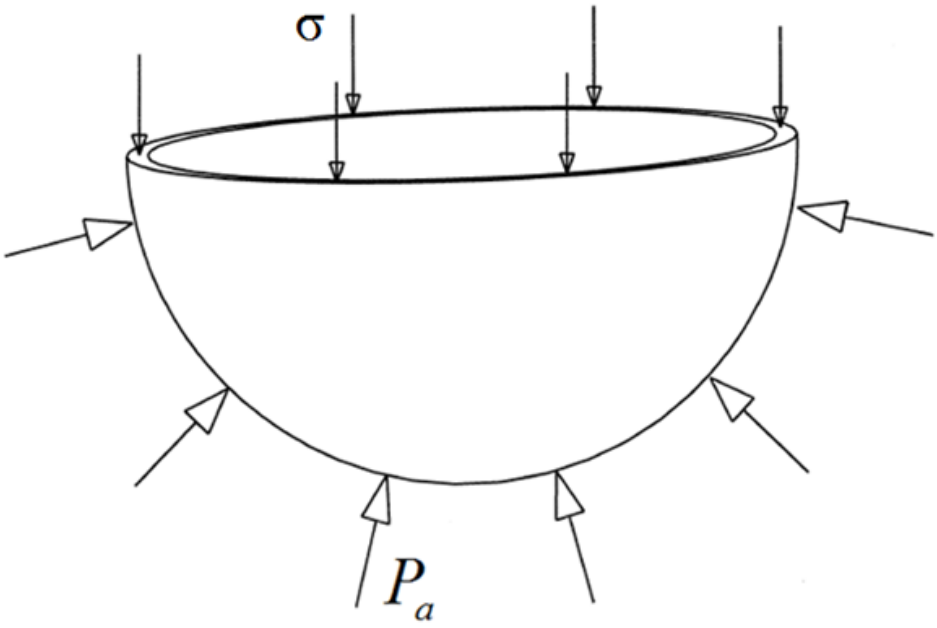

Figure 1: Forces Acting on Half-Sphere [5]

The sphere has a volume shown in Equation (1) and the thin shell has a volume shown in Equation (2) [5]. In order for the structure to obtain positive buoyancy, the mass of the air displaced by the sphere must be greater than the mass of the thin shelled sphere, as shown in Equation (3). The masses are obtained by multiplying the volume of the sphere and the volume of the thin shell by their corresponding densities. Equating the mass of the shell to the displaced air mass will determine the required thickness of the shell in terms of the densities of the air and the shell material. The thickness of the shell that is necessary for positive buoyancy is shown in Equation (4).

$$V_{sphere} = \frac{4}{3}\pi R^3 \tag{1}$$

$$V_{shell} = 4\pi R^2 t_{shell} \tag{2}$$

$$F_b \geq (W_{shell} = V_{shell}\rho_s g) \tag{3}$$

$$t_{shell} \leq R\rho_a/(3\rho_s) \tag{4}$$

where:

F_b = buoyant force

g = acceleration of gravity

R = sphere radius

t_{shell} = shell thickness

V_{shell} = shell volume

V_{sphere} = sphere volume

W_{shell} = shell weight

ρ_a = density of air

ρ_s = density of shell material

Collapse "is a geometric phenomenon where the structure suddenly loses its capacity to resist the applied loading and its geometry distorts; at that point the structure becomes globally unstable" [7]. From classical buckling theory, a critical pressure can be calculated that will cause the shell to collapse, which is shown in Equation (5) [9, p. 3]. Finally, Equation (4) can be substituted into Equation (5) in order to relate the required material properties necessary to achieve positive buoyancy by evacuating the air from a thin shelled sphere [5]. This relationship is shown in Equation (6).

$$P_{crit} = \frac{2Et_{shell}^2}{\sqrt{3(1-\nu^2)}}\frac{1}{R^2} \tag{5}$$

$$\frac{E}{\rho_s^2} = \frac{9P_{crit}\sqrt{3(1-\nu^2)}}{2\rho_a^2} \tag{6}$$

where:

E = modulus of elasticity

P_{crit} = critical pressure that will cause collapse

ν = Poisson's ratio

The United States standard atmospheric air pressure at sea level is known to be 101,325 Pascals and the density is 1.225 kg/m^3 [10, p. 20]. Substituting these values of P_{crit} and ρ_a into Equation (6), and using a Poisson's ratio of 0.3, a value for E/ρ_s^2 of about 500,000 $m^7/(kg \cdot s^2)$ is calculated. This value suggests that even a material such as defect free graphene, one of the least dense ($\rho_s = 1800\ kg/m^3$) and highest modulus (E = 1E12 Pascals) materials known, would not be able to withstand atmospheric pressure without collapse, as the ratio E/ρ_s^2 would be too small [11] [12].

With current commercially available materials a homogenous shell could not be used to create a LTAV subjected to a vacuum. Metlen proposed two concepts which theoretically could achieve positive buoyancy under a vacuum. His two design ideas were an isogrid sphere and a geodesic sphere. The isogrid sphere is not of particular interest in this research, and will not be discussed, but the geodesic sphere is the foundation of this research. Figure 2 shows the icosahedron design, which is a specific version of the geodesic sphere under consideration [7]. Using this general shape, Metlen revealed a LTAV using an internal vacuum is possible with certain materials [6].

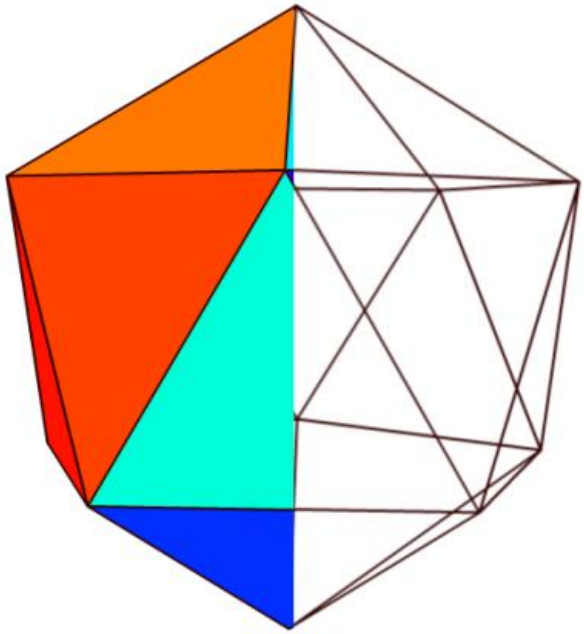

Figure 2: Icosahedron Frame (on Right) with Membrane Skin (on Left) [7]

Adorno-Rodriguez utilized Metlen's geometric model and completed a static analysis revealing the optimal materials, beam size, and membrane thickness for the structure. His research investigated several ideas not investigated by Metlen, including what beam cross-sectional shape should be used for the icosahedron frame, material selection for both the beams and skin, the effect of incorporating the skin on the model, the effect of large displacements on the buoyancy of the structure, possibility of achieving positive buoyancy with a partial vacuum, and the effect of varying altitudes on the buoyancy of the structure. Adorno-Rodriguez determined the ideal cross-section of the beams that make up the frame, which is shown in Figure 3 [7].

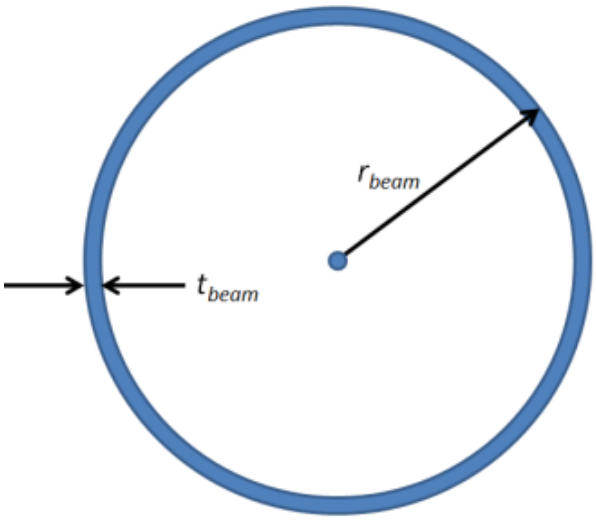

Figure 3: Beam Cross-section for Icosahedron Frame [7]

In his research, Adorno-Rodriguez determined an equation for selecting a material that will satisfy the weight-to-buoyancy ratio (W/B) necessary to achieve lift. His calculation accounted for the atmospheric effects, and is shown in Equation (7) [7].

$$\frac{W}{B} = \frac{9.5745 t_{skin} r^2 \rho_{skin} + 99.098(2c - c^2) r_{beam}^2 r \rho_{frame}}{[2.5362 r^3 - V_r]\left(\frac{P_{air,o}}{R^* T_{air,o}}\right)} + \frac{P_{air,i} T_{air,o}}{P_{air,o} T_{air,i}} \quad (7)$$

where:

B = buoyancy of the structure

c = beam thickness-to-radius ratio ($c = t_{beam}/r_{beam}$)

$P_{air,i}$, $P_{air,o}$ = inner and outer air pressure, respectively

R^* = air specific gas constant

r = radius of icosahedron ($0.9511 \cdot l_{beam}$)

$T_{air,i}, T_{air,o}$ = inner and outer air temperature, respectively

W = structure weight

V_r = volume reduction

$\rho_{frame}, \rho_{skin}$ = frame and skin densities, respectively

He plotted W/B for seven different models constructed with three different combinations of materials. The relationships of the applied pressure to the max Von Mises stresses of his results are shown in Figure 4 and Figure 5 [7]. The horizontal lines represent lines of positive buoyancy indicating a threshold which the applied stress on the structure must exceed for the structure to float in air. Several vertical dashed lines are also shown in the plot, which represent the yield strength of the material the beams and skin are constructed with.

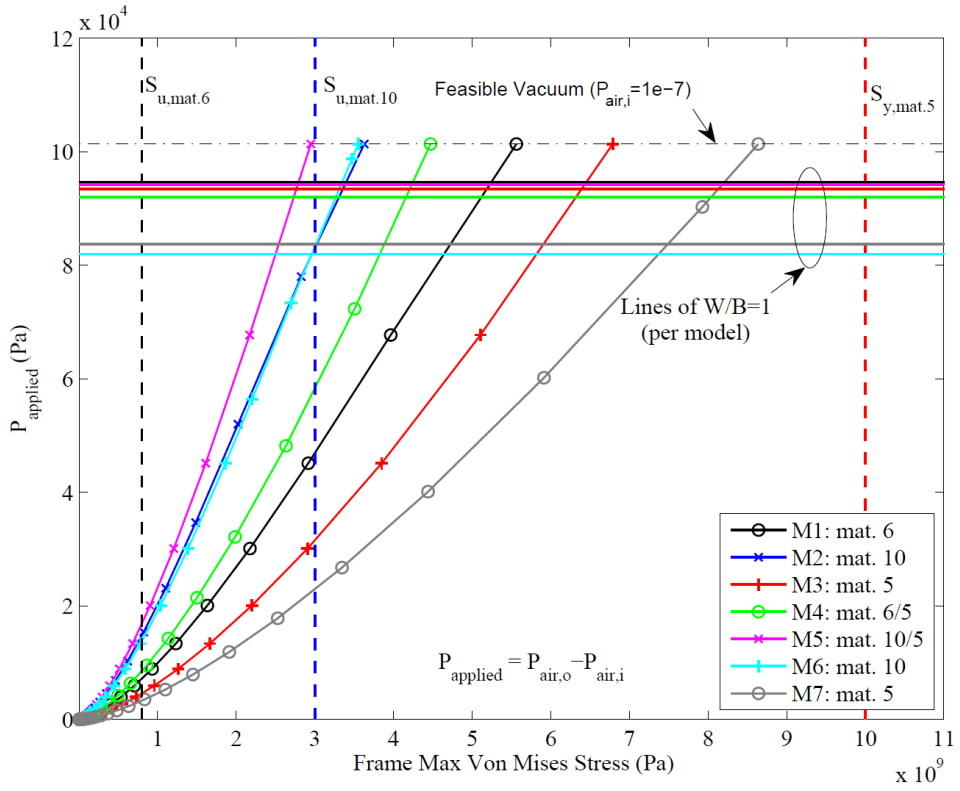

Figure 4: Applied Pressure versus Max Von Mises Stress for the Frame [7]

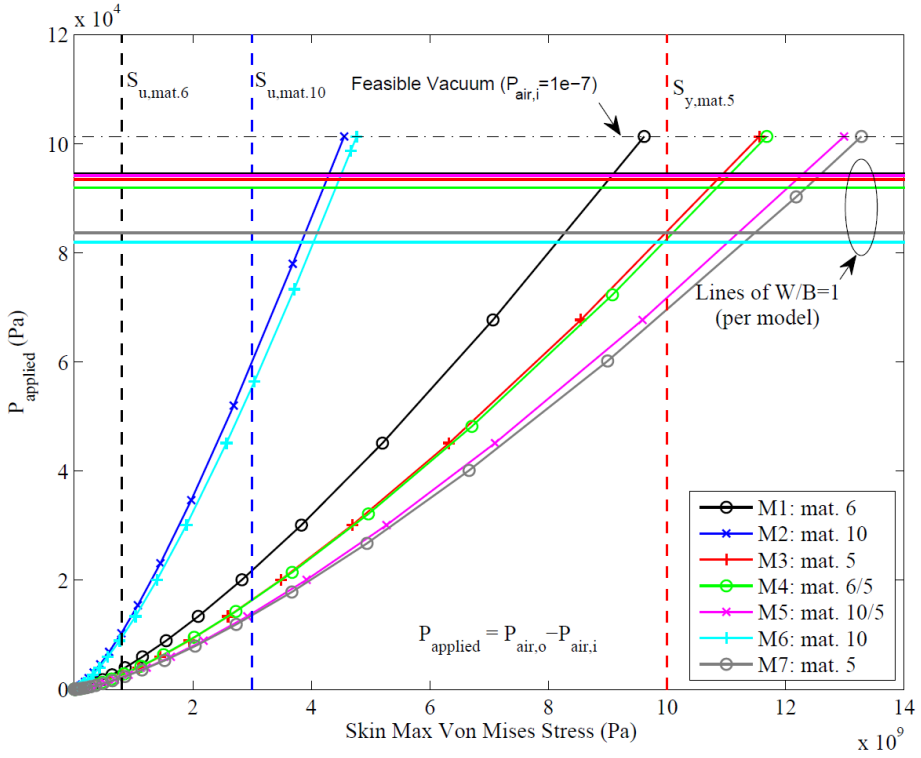

Figure 5: Applied Pressure versus Max Von Mises Stress for the Skin [7]

The research used to produce Figure 4 and Figure 5 was conducted using a static analysis. Both plots show the frame and the skin have significant internal stresses that are, for most of the models considered, above the yield strength of the material and not likely to withstand the applied pressure required to achieve positive buoyancy. However, two of the models considered (M3 and M7) are able to withstand the required applied pressure prior to reaching their corresponding material yield strength. This indicates, using certain materials, an icosahedron shaped LTAV can achieve positive buoyancy using an internal vacuum. The material in Figure 4 and Figure 5 that avoids collapse in both models is Nanocyl NC7000 Thin Multi-Wall Carbon Nanotubes [7]. While this finding is highly encouraging, the material is not readily produced or commercially manufactured, and is therefore not considered in the remainder of this research. The

material that is considered from Adorno-Rodriguez's model is Beryllium. It is a currently available material with well known material properties, and while it isn't likely able to withstand the necessary applied pressure required to achieve positive buoyancy, it is useful in studying to understand the structural characteristics of the design as a basis for future materials.

In addition, Adorno-Rodriguez made improvements to the computer model used in analyzing the structure, and enhanced the accuracy of the calculations on the structure. He conducted a comparison between membrane and plate elements in FEA, and compared the results to the accepted analytical solution. He also performed a convergence test that verified the correct number of elements to use in the model. The results obtained by Adorno-Rodriguez form the baseline model used throughout this research, and specific details on the baseline model are stated in Chapter III.

Finite Element Analysis and the Dynamic Response

"The power and usefulness of the finite element method is … in modeling and solving complicated parts and structures that do not have closed-form solutions" [13, pp. 575-576]. FEA is essential in determining the dynamic response of the icosahedron shaped LTAV because it is a complex structure without a closed-form solution. The dynamic response of a structure can be obtained by using Finite Element Analysis to solve Equation (8) (or Equation (9) if the material is linearly elastic) shown below [14]:

$$[M]\{\ddot{D}\} + [C]\{\dot{D}\} + \{R^{int}\} = \{R^{ext}\} \tag{8}$$

$$[M]\{\ddot{D}\} + [C]\{\dot{D}\} + [K]\{D\} = \{R^{ext}\} \quad (9)$$

where:

C = damping matrix

$D, \dot{D}, \ddot{D}$ = nodal position, velocity, and acceleration, respectively

K = stiffness matrix

M = mass matrix

R^{ext}, R^{int} = externally applied loads and internal force vector, respectively

Free vibrations of the structure are first computed by solving the undamped matrix equation shown in Equation (10). The solution to the matrix gives the natural frequencies (eigenvalues) and mode shapes (eigenvectors) of the structure used in subsequent calculations of the dynamic response [15]. Many simple structures have analytical solutions for the natural frequencies derived from the equations of motion; however, more complex structures require FEA to solve the eigenvalue problem shown in Equation (12). For example, a simply supported beam has natural frequencies shown in Equation (11), derived from solving the Euler-Bernoulli beam equations of motion [13]. These values can easily be checked against the values determined from solving the undamped eigenvalue problem of Equation (12). Determining the natural frequencies and mode shapes of a structure reveals the inherent dynamic characteristics of the system. The natural frequencies indicate the resonant frequency of a system, where the amplitude of oscillation reaches a maximum. The mode shapes indicate the patterns of deformation that occur when the system is oscillating at a natural frequency. Different mode shapes

occur for every unique natural frequency. Repeated natural frequencies have identical mode shapes, and usually indicate symmetry in a structure. The eigenvalues problem of Equation (12) shows that natural frequencies and mode shapes of an undamped system are based on the stiffness and mass of the structure [16].

$$[M]\{\ddot{D}\} + [K]\{D\} = \{0\} \tag{10}$$

$$\omega_n = \frac{\left(EI/\rho A\right) n^4 \pi^4}{L^4} \tag{11}$$

$$(-\omega_n^2[M] + [K])\{\phi_n\} = \{0\} \tag{12}$$

where:

A = cross-sectional area of the beam

E = modulus of Elasticity

I = area moment of inertia

L = length of beam

n = natural frequency number

ρ = density

ω_n= natural frequency value (eigenvalues)

ϕ_n = mode shape (eigenvector)

A solution to the dynamic response problem of Equation (9) can be determined by implicit direct integration or explicit direct integration. A distinction needs to be made about the type of problem under consideration to choose which solution technique is

more appropriate; specifically, whether the problem is a wave propagation type or structural dynamics type. The problem considered in this thesis structural dynamics oriented which is best suited to solve by implicit direct integration. As stated by Cook, et al., "Implicit direct integration is suited to structural dynamics problems [and] nonlinearity can be accommodated without great trouble" [14, p. 409]. The implicit direct integration technique will be used in the remainder of the research, and therefore the methodology behind explicit direct integration will not be discussed. Additional information on the previously mentioned methods is provided by Cook, et al. [14].

The implicit direct integration method can increase computational time significantly, and requires more storage space than the explicit direct integration method. However, it is unconditionally stable unlike the explicit direct integration method, and therefore does not require a critical time step that will provide a correct solution to the problem. While a critical time step is not necessary for a solution, using too large of time step will reduce the accuracy of the solution, and therefore care must be exercised in selecting the proper time step.

$[K]$ can change with time in the case of nonlinearity and the dynamic response infers time dependence, so Equation (8) can be manipulated to Equation (13), where *n* indicates each time increment [14].

$$[M]\{\ddot{D}\}_n + [C]\{\dot{D}\}_n + \{R^{int}\}_n = \{R^{ext}\}_n \tag{13}$$

The method of implicit direct integration calculates future response values based on the current and past response values. A general form of the solution is shown below in Equation (14) [14]:

$$\{D\}_{n+1} = f\left(\{\dot{D}\}_{n+1}, \{\ddot{D}\}_{n+1}, \{D\}_n, \{\dot{D}\}_n, \{\ddot{D}\}_n, \ldots\right) \tag{14}$$

Specific forms of Equation (14) exist that can be used in calculating a response to the structure at each time increment. The different forms will not be revealed here, but the reader is encouraged to refer to Cook, et al. [14] for a detailed discussion on them. In a nonlinear analysis, Abaqus computer software uses an iterative scheme in solving the problem. According to the Abaqus documentation,

> The solution is found by specifying the loading as a function of time and incrementing time to obtain the nonlinear response. Therefore, Abaqus breaks the simulation into a number of time increments and finds the approximate equilibrium configuration at the end of each time increment [17].

The user determines the type of time increment to be used, whether fixed or automatic. If an automatic solution is desired, Abaqus automatically adjusts the size of the time increments to solve the nonlinear problems efficiently based on algorithms within the program [17]. Alternatively, a fixed solution can be obtained by forcing the program to use the same time increment to solve the problem. If equilibrium cannot be achieved using the fixed time increment selected, an error will occur and the user is required to reduce the size of the time increment in order to obtain a solution. An automatic time step will continuously change size until a solution is determined, or the maximum number of iterations specified is exceeded. Therefore, an automatic time increment solution usually

provides a faster convergence to the solution; however, the response may not have the number of data points required for further analysis, and a fixed time increment approach may be required.

In addition to the time response outlined above, FEA can be used to analyze the frequency response of a structure. This type of response analysis can be important, because identifies certain operating frequencies likely to cause failure of the structure.

Frequency Response Functions and Power Spectral Density Functions

The frequency response is an important aspect to study when determining the overall structural response of a system because it can reveal additional information to what can be extracted from the time response. Unlike the time domain response, which only represents the response to a single excitation frequency, the frequency domain response reveals information for all excitation frequencies with a periodic external force. Frequency response functions are the ratio of the output response of a structure due to an externally applied force [18, p. 1].

The determination of the frequency response due to an arbitrary excitation requires a Fourier transformation. A forcing function, like the one shown on the right hand side of Equation (8), can be represented by a Fourier series or Fourier integral, where a function in the time domain can be expressed in terms of frequency. The general complex form relationship between time and frequency of an arbitrary excitation force is shown in Equation (15). Similarly, the response of the system to that excitation force can be written in terms of the frequency by way of a Fourier transform, as shown in Equation (16).

Finally, the frequency response function can be represented by the relationship shown in Equation (17) [19, pp. 703-705].

$$F(\omega) = \int_{-\infty}^{\infty} f(t) e^{-i\omega t} dt \tag{15}$$

$$X(\omega) = \int_{-\infty}^{\infty} x(t) e^{-i\omega t} dt \tag{16}$$

$$G(\omega) = \frac{X(\omega)}{F(\omega)} \tag{17}$$

where:

$f(t)$ = forcing function applied as a function of time, t

$F(\omega)$ = Fourier transform of $f(t)$ as a function of frequency, ω

$G(\omega)$ = frequency response function

$x(t)$ = system response as a function of time, t

$X(\omega)$ = Fourier transform of $x(t)$ as a function of frequency, ω

$e^{-i\omega t} = \cos(\omega t) - i \sin(\omega t)$ = complex representation of a function

The transformation from the time domain to the frequency domain results in complex valued numbers, where the function in the frequency domain contains real and imaginary components. The real and imaginary parts of the function can be analyzed in terms of magnitude and phase. Magnitude is the absolute value of the complex valued number, and is typically plotted in decibels. Phase angle is the argument of the complex valued number, and is typically plotted in radians or degrees. The magnitude and phase are important representations for any frequency domain function, and when used in unison,

can provide valuable information regarding the dynamics of a system. The magnitude is of particular interest when it is plotted as a function of frequency. The location of the peaks of the magnitude plot represents the eigenvalues of the system, indicating the natural frequencies where the structure resonates. Plotting the peak amplitude of the imaginary part of the frequency response function reveals the mode shapes of the system at the given natural frequency [18].

In the case of a random variable, a similar representation of frequencies that excite the system the greatest can be obtained via the power spectral density (PSD) function. The power spectral density function displays similar information with the exception that only the response as a function of time is required rather than the input forcing function as well. In obtaining the power spectral density function, the autocorrelation function that relates the value of the variable at one time to the value of that variable at another time is used. The autocorrelation function is shown in Equation (18). The power spectral density function is simply the Fourier transform of the autocorrelation function, as shown in Equation (19).

$$R_x(\tau) = \lim_{T\to\infty} \frac{1}{T} \int_{-T/2}^{T/2} x(t)x(t+\tau)dt \tag{18}$$

$$S_x(\omega) = \int_{-\infty}^{\infty} R_x(\tau) e^{-i\omega\tau} d\tau \tag{19}$$

where:

$R_x(\tau)$ = autocorrelation function as a function of time shift, τ

$S_x(\omega)$ = power spectral density function in terms of frequency, ω

T = period of signal

The algorithms used throughout this research for calculation of the PSD function are provided by MATLAB and are shown in the Appendix.

Frequency responses deliver a wealth of information about the behavior of a structure under a dynamic load, and they can help characterize the behavior that is shown. Specifically, the frequency response can be useful in identifying what has been termed chaotic behavior. This is particularly useful in this thesis as previous research on an icosahedron LTAV has predicted a *snapback* behavior that is presumed to be chaotic. Therefore, in developing a better understanding of the structural behavior of the icosahedron shaped LTAV, a study of chaotic behavior is necessary.

Chaotic Behavior

Chaos is "the irregular and unpredictable time evolution of many nonlinear systems," in which that "system does not repeat its past behavior. Yet, despite their lack of regularity, chaotic dynamical systems follow deterministic equations such as those derived from Newton's second law" [20, p. 1]. Chaotic behavior only occurs when the governing equations of a system are nonlinear and the system has a time history with "sensitivity to initial conditions" [20, p. 1]. Several indicators show if a system displays chaotic behavior. An analysis of the phase-plane trajectory, power spectral density plots, and the calculation of Lyapunov exponents can distinguish chaotic motion from non-chaotic motion.

An explanation of two dynamical systems can help illustrate the difference between a chaotic system and a non-chaotic one. A simple pendulum with known initial conditions and boundary conditions has a predictable periodic time response, and changing the

initial conditions does not alter the nature of the response. It will still be periodic and predictable as shown in Figure 6. By adding another pendulum to the end of the first pendulum, a double pendulum is created. This system, unlike the first, exhibits wildly different responses to small changes in the initial conditions, and for certain initial conditions the motion is known to be chaotic [21]. Figure 7 shows the trajectories of the double pendulum for two different initial conditions. Clearly, slight changes in the initial conditions cause significant changes in the response of the system, indicative of chaotic motion.

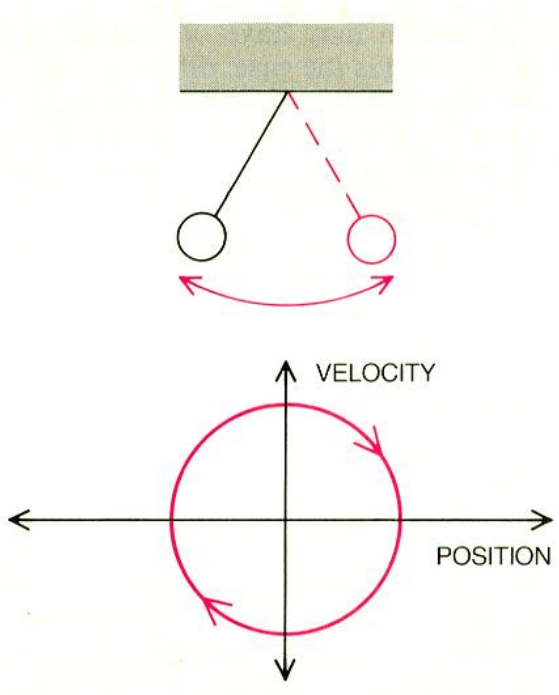

Figure 6: Single Pendulum System (Top) and Phase-plane Trajectory (Bottom) [22]

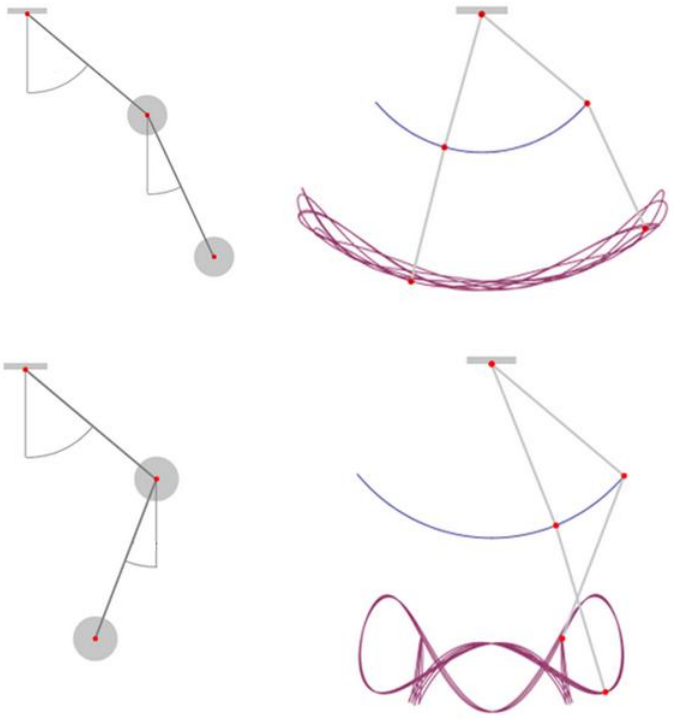

Figure 7: Double Pendulum System with Different Initial Conditions (Left) and the Trajectories of the Two Points Corresponding to Each System (Right) [23]

A phase-plane history plot shows velocity versus position for some point on the structure over time. If the system is in static equilibrium, the phase-plane plot appears as a single point. If the system is dynamically stable and has a periodic motion, the phase-plane plot has a trajectory appearing as a closed curve, known as an orbit. Considering the single pendulum with damping, a phase space diagram of the orbit is shown in Figure 8 [20]. The periodically decaying motion resulting from a single pendulum eventually converges to a single point, known as the *attractor*, no matter what the initial conditions are. "Attractors are geometric forms that characterize long-term behavior in the state space…it is what the behavior of a system settles down to, or is attracted to" [22]. *Attractors* can take on various forms, with the simplest being the single point shown at

the origin of Figure 8. The next most complicated *attractor* is a closed loop, then a torus. These three *attractors* are predictable and non-chaotic; however, chaotic *attractors* have more complicated geometric forms [22]. If the system displays chaotic behavior, the phase-plane plot consists of "orbits whose trajectories tend to fill up a portion of the phase space" [24].

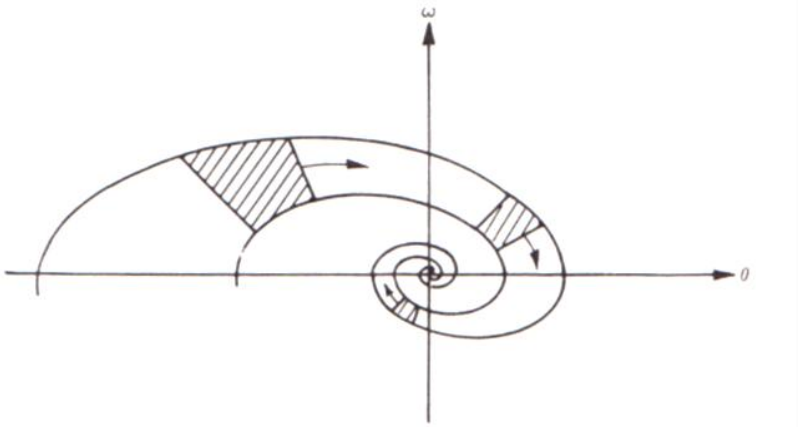

Figure 8: Phase Space Diagram of Single Pendulum Motion Decaying to *Attractor* [20]

Power spectral density plots indicate the presence of chaotic behavior as well. Alone, they are not a good indicator alone to characterize chaos, when used in concert with the other tools mentioned; they can help in distinguishing a chaotic system from a non-chaotic one. Specifically, non-chaotic PSD plots tend to be fairly smooth with clear peaks at the frequencies of highest attenuation, while chaotic PSD plots tend to become more irregular without a discreet frequency associated with the motion [24].

A final measure to determine if a system exhibits chaotic behavior is the calculation of the Lyapunov exponents. "Lyapunov exponents [have] proven to be the most useful dynamical diagnostic for chaotic systems. [They] are the average exponential rates of divergence or convergence of nearby orbits in phase space…Any system containing at

least one positive Lyapunov exponent is defined to be chaotic" [25, p. 285]. Wolf, et al. presented Equation (20) to calculate the Lyapunov exponent from experimental data [25, p. 295]. An *attractor* is reconstructed using the time series data, and the trajectories of the reconstructed plot are analyzed to determine if convergence or divergence occurs from one orbit to the next. The trajectory is traversed and the distance between neighboring points on the trajectory is calculated, as well as evolved length between points to determine convergence or divergence. If a neighboring point happens to be on a different trajectory passing by in a crossing fashion, a replacement point is determined to ensure the correct trajectory is followed. A more thorough explanation of the process can be found in the *Determining Lyapunov Exponents from a Time Series* paper by Wolf, et al. As Equation (20) shows, the value of the Lyapunov exponent changes with each time step, and the final value is the sum of all previously calculated time increments. If the value of the calculated Lyapunov exponent is negative or equal to zero, periodic motion is indicated. If the value is positive, chaotic motion is indicated and two trajectories with nearly identical initial conditions will diverge. Moreover, the magnitude of the Lyapunov exponent indicates the amount of chaos present in the system [24].

$$\lambda_1 = \frac{1}{t_N - t_0} \sum_{k=1}^{N} \log_2 \frac{L_p'(t_k)}{L_p(t_{k-1})} \tag{20}$$

where:

$L_p(t_{k-1})$ = length between two points on the trajectory

$L_p'(t_k)$ = evolved length between two points at a later time

N = total number of replacement steps

t_N = time of current replacement step

t_0= initial time

λ_1 = Lyapunov exponent

The algorithms used to calculate the Lyapunov exponents in this research are provided in a MATLAB code written by Wolf, et al., and are shown in the Appendix.

Summary

Initial research necessary in determining the possibility of an icosahedron shaped LTAV has been completed by Metlen and Adorno-Rodriguez. Metlen introduced the concept for the geometric shape; while Adorno-Rodriguez optimized the design, and proved that a W/B could be achieved resulting in positive buoyancy prior to collapse of the structure. His model provides a baseline for the remainder of this thesis; however, modifications are necessary to study the dynamic response. The FEA equations used in calculating the natural frequencies, mode shapes, and time-dependent dynamic solution were presented as well as the method of implicit direct integration as it is utilized in computing the dynamic response of the model. Additionally, frequency response interpretations were introduced as a method of characterizing the behavior of the structure. Finally, the idea of chaos and the methods of determining its presence were outlined. The following chapter will reveal the model development and methodology that will be used in determining a dynamic response to various loading conditions.

III. Model Development

Chapter Overview

A study of the dynamic response of an icosahedron shaped LTAV requires a robust model. Metlen and Adorno-Rodriguez created a model capable of producing important information about the static response of the icosahedron shaped LTAV, as described in Chapter II. This chapter will detail the specific FEA methods, model development, and the analysis process used in analyzing the models considered in this research.

The model developed by Adorno-Rodriguez was the baseline model used throughout this research, and is covered in detail in the first section. From the baseline model, natural frequencies and mode shapes were determined using the Abaqus modeling software. Next, the structure was dissected into individual components to investigate how each part of the model interacts to combine into the whole. The results of the original model were verified with an experimental setup. Additionally, an equivalent stiffness comparison of simpler structures was conducted in order to draw conclusions on the response characteristics of the icosahedron. Certain aspects must be considered when conducting a dynamic analysis which is not necessarily considered in a static analysis. Specifically, the time step value for the numerical integrator used to calculate the response is detailed in the final section of this chapter.

Icosahedron Design

The baseline icosahedron design was discussed previously in Chapter II, but the details of the design are reiterated here. Figure 9 depicts the icosahedron frame model used in Abaqus, and Figure 10 shows the frame with the skin attached. The dimensions of

the icosahedron, and the material properties for Beryllium, are listed in Table 1. This version of the model creates a weight-to-buoyancy ratio of one utilizing Equation (7). A W/B equal to one means the structure would float at sea-level, but not rise. Other versions of the model developed by Adorno-Rodriguez are capable of reaching W/B ratios lower than one; however, the other materials he used are not well understood, or even commercially available in large quantities at the current time. One goal of this research is to understand the dynamic structural properties of the design, and therefore only the model shown below is considered.

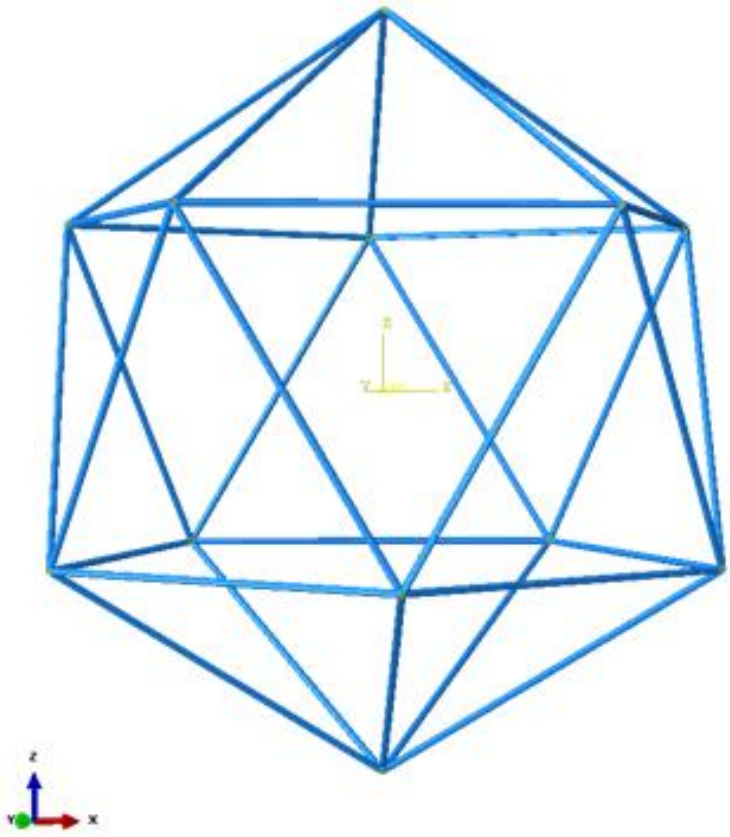

Figure 9: Abaqus View of Baseline Icosahedron Frame

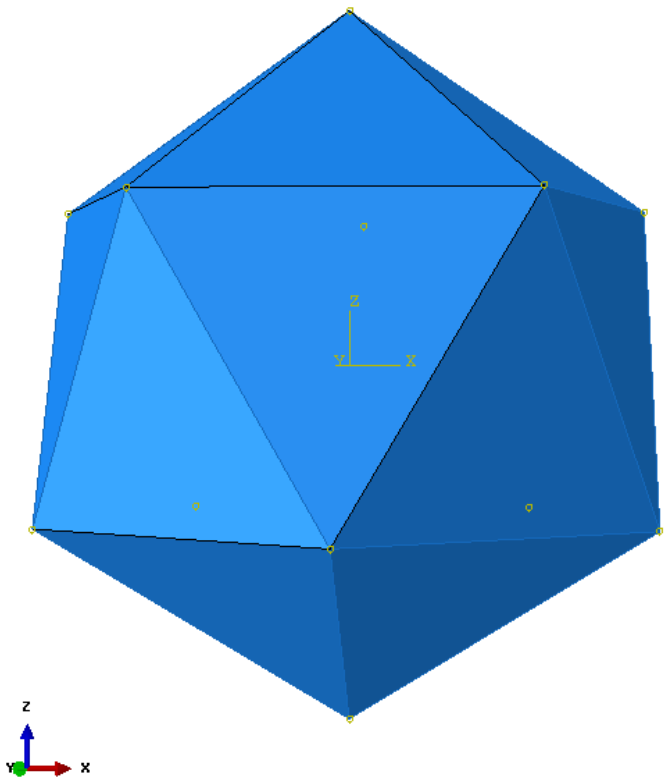

Figure 10: Abaqus View of Baseline Icosahedron with Skin

Table 1: Baseline Icosahedron Dimensionality

	Dimension	Units
Radius (center to vertex)	1.0 (0.3048)	ft (m)
Beam Cross-Section Radius	5.995e-02 (1.523e-03)	in (m)
Beam Cross-Section Thickness	2.998e-03 (7.614e-05)	in (m)
Beryllium Density	115.12 (1844.0)	lb/ft^3 (kg/m^3)
Beryllium Modulus of Elasticity	6.33 (303.0)	lb/ft^2 (GPa)
Beryllium Poisson's Ratio	0.18	unit less
Skin Thickness	4.3952e-04 (1.11638e-05)	in (m)

Adorno-Rodriguez conducted a convergence study to determine the discretization of the model, and determined each beam in the frame should be constructed using at least eight B32 beam elements [7]. B32 beams in Abaqus are Timoshenko beams that allow for transverse shear deformation and use a quadratic interpolation between nodes [17]. Similarly, he concluded that 270 M3D3 membrane elements were sufficient to discretize one of the triangular skins of the icosahedron. In the previous research, S3R shell elements were compared to the M3D3 membrane elements. For very small thicknesses, a minimal difference was calculated between the two in terms of displacement and stress [7]. This is important because S3R elements must replace M3D3 elements in this research to calculate the eigenvalues and mode shapes because a membrane does not possess initial stiffness when subjected to a force perpendicular to the membrane. The solution to Equation (12) is singular without a stiffness matrix, and therefore a shell element has to be utilized for the calculation. The difference in the shell element degrees of freedom and those of the membrane are shown in Figure 11. The shell elements provide stiffness in all degrees of freedom (DoF), while the membrane is restricted to the translational DoF [7].

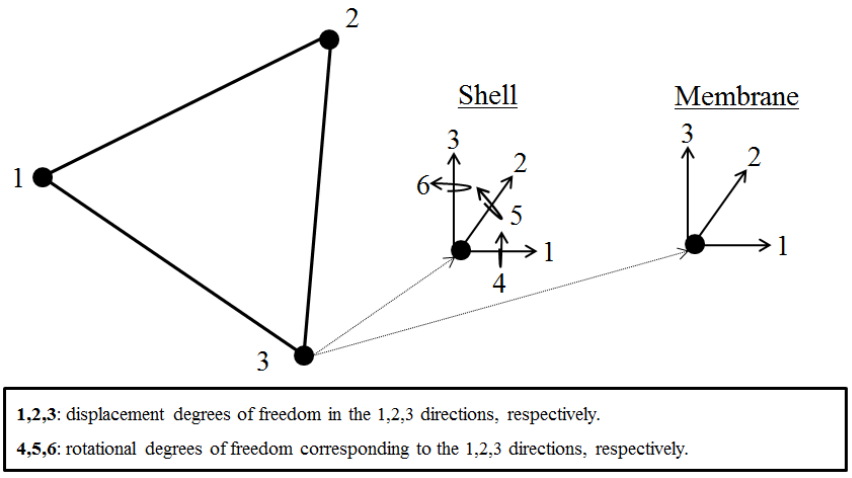

Figure 11: Degrees of Freedom for Shell and Membrane Elements [7]

Decomposition of Icosahedron

A method to verify the baseline model presented in the previous section was desired to confirm the results obtained from the computer simulations are accurate. This section explains the decomposition of the icosahedron into individual parts to simplify the structure for the process of verification. An icosahedron structure is challenging to build and test; however, the subcomponents it is made of are much simpler, and more easily constructed on which testing can be conducted. A modal analysis was used in comparing the characteristics of the structures under consideration.

Natural frequencies and mode shapes of the standalone frame as well as the frame-skin model were calculated using the Abaqus *Frequency* eigensolver. The frequency solution in Abaqus is simply a calculation of the undamped natural frequencies as explained in Chapter II by solving Equation (12). The first twenty modes were determined for each model (frame only and frame with skin) for the free boundary condition. A high number of modes were calculated because the icosahedron has twenty sides, and the natural frequencies associated with the modes seem to come in sets of twenty, corresponding to the number of sides.

With the mode shapes and natural frequencies evaluated for the entire icosahedron, the structure was decomposed into its basic components to draw a comparison between the individual parts and the structure as a whole. The first component considered was a single triangle of the icosahedron. Next, the equilateral triangle membrane alone was considered without the beams supporting the edges. Finally, a single beam of the frame was evaluated. The decomposition from the whole structure into the individual components is shown in Figure 12 and Figure 13 for the standalone frame and the frame-

skin model, respectively. The steps in the figures refer to the step of decomposition. For example, the first step of decomposition for the frame is to a single triangle, and the second step is from the single triangle to the single beam.

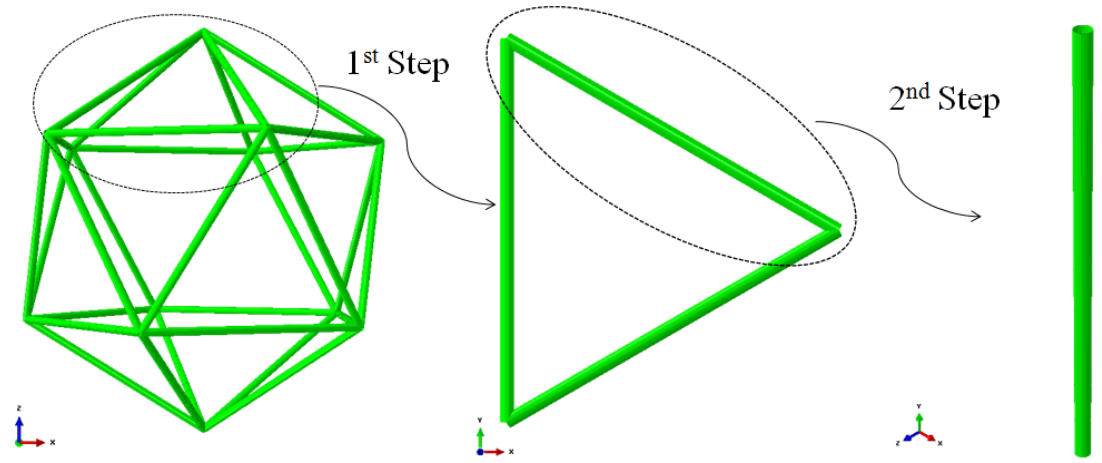

Figure 12: Decomposition of Standalone Frame Model

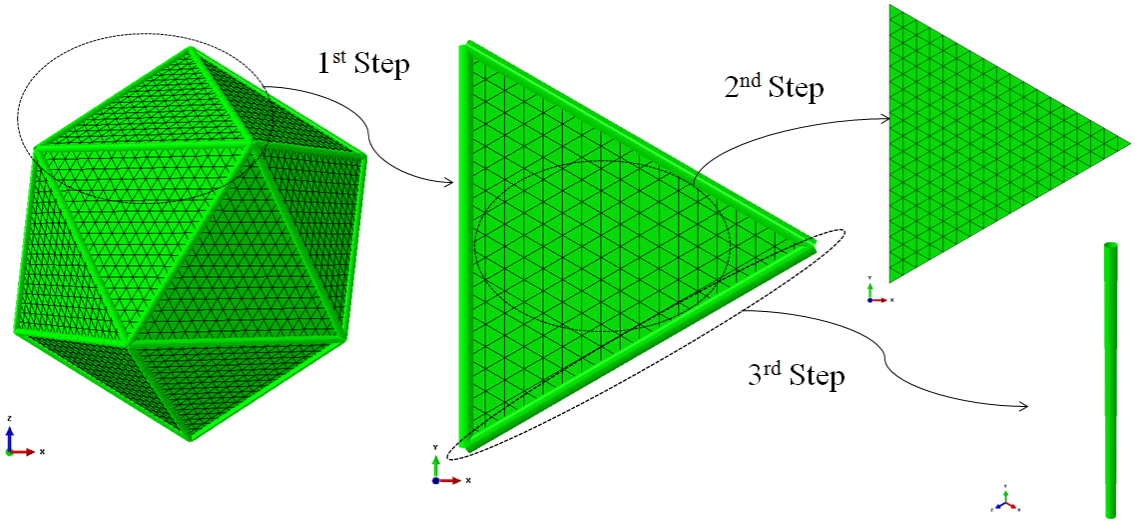

Figure 13: Decomposition of Frame-Skin Model

Table 2 through Table 5 show the natural frequencies calculated for the entire frame, and frame-skin icosahedron models, as well as the individual components the model is comprised of. All of the values shown in the tables are in units of Hertz. Table 2 corresponds to the first step in Figure 12 and Table 3 corresponds to the second step shown in Figure 12. Similarly, Table 4 corresponds to the first step shown in Figure 13, while Table 5 corresponds to the second step of the icosahedron structure decomposition as shown in Figure 13. Step three of Figure 13 is not shown in any table because it is the same beam of the frame, and has equivalent eigenvalues. In each step of the decomposition, the natural frequencies of the component being analyzed were determined for three different boundary conditions: free, simply supported, and clamped at the vertex of the triangle or end of the beam. The three different boundary conditions were applied in an attempt to characterize the interaction at the vertices of the icosahedron to the individual triangles, and an illustration of the boundary conditions is shown in Figure 14. The two dimensional depiction explains the difference between a clamped boundary condition and a simply supported boundary condition, as they are applied to an individual beam. The rigid body modes that arise from the free boundary condition placed on the icosahedron, and occur for natural frequencies of zero, are not shown in the tables.

Table 2: Eigenvalues for Icosahedron Frame Decomposition – Triangle

Mode #	Frame	Single Triangle of Frame – Free	Single Triangle of Frame – Simply Supported	Single Triangle of Frame – Clamped
1	1022.02	1310.01	822.12	1857.08
2	1022.02	1310.01	1035.65	1857.08
3	1022.04	1344.22	1035.65	1857.08
4	1022.04	1344.22	1052.87	1857.08
5	1049.94	1855.95	1052.87	1857.09
6	1049.95	1859.88	1857.09	1857.09
7	1049.95	3841.60	3266.98	5087.01
8	1049.97	3917.15	3266.99	5087.01
9	1049.97	4547.76	3278.12	5087.01
10	1096.96	4547.77	3841.60	5087.01
11	1096.96	4550.54	4562.84	5087.03
12	1096.97	4550.55	4562.85	5087.03
13	1178.22	8219.36	7314.85	9890.33
14	1178.22	8219.37	7497.42	9890.33
15	Rigid Body Modes Omitted		7497.44	9890.33
16			7988.77	9890.33
17			7988.79	9890.37
18			9890.34	9890.37
19			12711.40	16181.90
20			12711.50	16181.90

Table 3: Eigenvalues for Icosahedron Frame Decomposition – Beam

Mode #	Frame	Single Beam of Frame – Free	Single Beam of Frame – Simply Supported	Single Beam of Frame – Clamped
1	1022.02	1863.35	822.80	1858.25
2	1022.02	1863.35	822.80	1858.25
3	1022.04	5116.93	3280.87	5093.55
4	1022.04	5116.93	3280.87	5093.55
5	1049.94	9986.21	7349.31	9923.51
6	1049.95	9986.21	7349.31	9923.51
7	1049.95	16439.90	13004.90	16310.70
8	1049.97	16439.90	13004.90	16310.70
9	1049.97	24499.90	20247.60	24273.40

10	1096.96	24499.90	20247.60	24273.40
11	1096.96	26043.30	26043.30	26043.30
12	1096.97	34243.70	29122.70	33889.60
13	1178.22	34243.70	29122.70	33889.60
14	1178.22	40008.40	45326.90	40008.40
15	Rigid Body Modes Omitted		39739.60	45326.90
16			39739.60	52091.70
17			40008.40	58904.10
18			52091.70	58904.10
19			52284.90	75837.00
20				75837.00

Table 4: Eigenvalues for Icosahedron Frame and Skin Decomposition – Triangle with Beams and Skin

Mode #	**Icosahedron**	**Single Triangle of Icosahedron – Free**	**Single Triangle of Icosahedron – Simply Supported**	**Single Triangle of Icosahedron – Clamped**
1	18.22	14.80	13.51	13.51
2	18.50	49.71	48.04	48.04
3	18.89	54.91	52.67	52.68
4	19.20	57.36	55.85	55.86
5	19.69	134.22	133.03	133.06
6	19.97	136.96	135.28	135.31
7	20.02	140.61	140.14	140.18
8	28.75	158.65	156.76	156.77
9	29.00	176.67	174.88	174.89
10	30.15	270.00	268.25	268.38
11	31.30	331.61	331.50	331.56
12	33.84	352.84	350.67	350.78
13	34.73	391.68	389.42	389.58
14	35.57	406.48	406.38	406.58
15	Rigid Body Modes Omitted		432.49	432.77
16			487.61	488.51
17			499.39	499.86
18			720.25	722.22
19			795.36	795.79
20			802.42	861.54

Table 5: Eigenvalues for Icosahedron Frame and Skin Decomposition – Triangle Skin

Mode #	Icosahedron	Single Triangle of Icosahedron (Skin Only) – Free	Single Triangle of Icosahedron (Skin Only) – Simply Supported	Single Triangle of Icosahedron (Skin Only) – Clamped
1	18.22	9.17	2.23	3.23
2	18.50	10.63	5.84	9.26
3	18.89	10.66	5.85	9.37
4	19.20	24.53	15.34	21.50
5	19.69	24.58	15.36	22.02
6	19.97	32.93	20.89	24.49
7	20.02	47.16	38.08	39.74
8	28.75	52.30	38.30	46.23
9	29.00	53.20	38.56	46.76
10	30.15	53.76	52.74	64.83
11	31.30	80.01	65.04	75.90
12	33.84	80.80	65.28	76.58
13	34.73	92.63	68.89	77.82
14	35.57	120.58	105.22	110.87
15	Rigid Body Modes Omitted		105.47	120.32
16			106.52	121.17
17			125.90	132.94
18			153.19	166.94
19			155.29	174.26
20			156.29	175.83

The decomposition of the icosahedron into its components shows a relationship between each of the individual parts that make up the icosahedron and the entire structure itself. In almost every case of decomposition, the natural calculated for the individual part being analyzed are not exactly the same as the entire structure, regardless of the boundary condition applied. However, for most of the decomposition cases, the first natural frequency of the entire structure typically lies between the first natural frequency of the individual parts for the simply supported and clamped boundary conditions. Higher order modes quickly diverge because the icosahedron has twenty sides, and therefore, has repeated eigenvalues for the first twenty modes. This relationship of the natural

frequencies is intuitive because the vertices of the icosahedron are not rigidly supported, but they do restrict the motion of the individual components more than a simply supported boundary condition. Therefore, the vertices of the icosahedron likely present a boundary condition that lies between the clamped condition and the simply supported condition. To replicate the boundary condition presented by the vertices of the icosahedron, a modified clamped boundary condition was devised and tested.

Experimental Test Setup

The construction and testing of an icosahedron is a difficult challenge; however, the construction of its components is significantly easier. Based on the decomposition study of the icosahedron, a single triangle of the structure has natural frequencies that lie between a clamped structure and a simply supported structure at each of the vertices. In reality, boundary conditions often lie between a simply supported condition and a clamped condition as "perfect" boundary conditions are impossible to implement.

To achieve a boundary condition stiffer than a pinned end, and softer than a clamped end, translational and rotational springs can be applied to the end to be more indicative of the true boundary condition. Figure 14 shows this application for a single beam with only three degrees of freedom. In the case of the experimental triangle, all six degrees of freedom are considered. Additionally, an elastic foundation can be applied to an entire surface if that surface is not rigidly tied to the surface upon which it sits, as shown in the bottom of Figure 14.

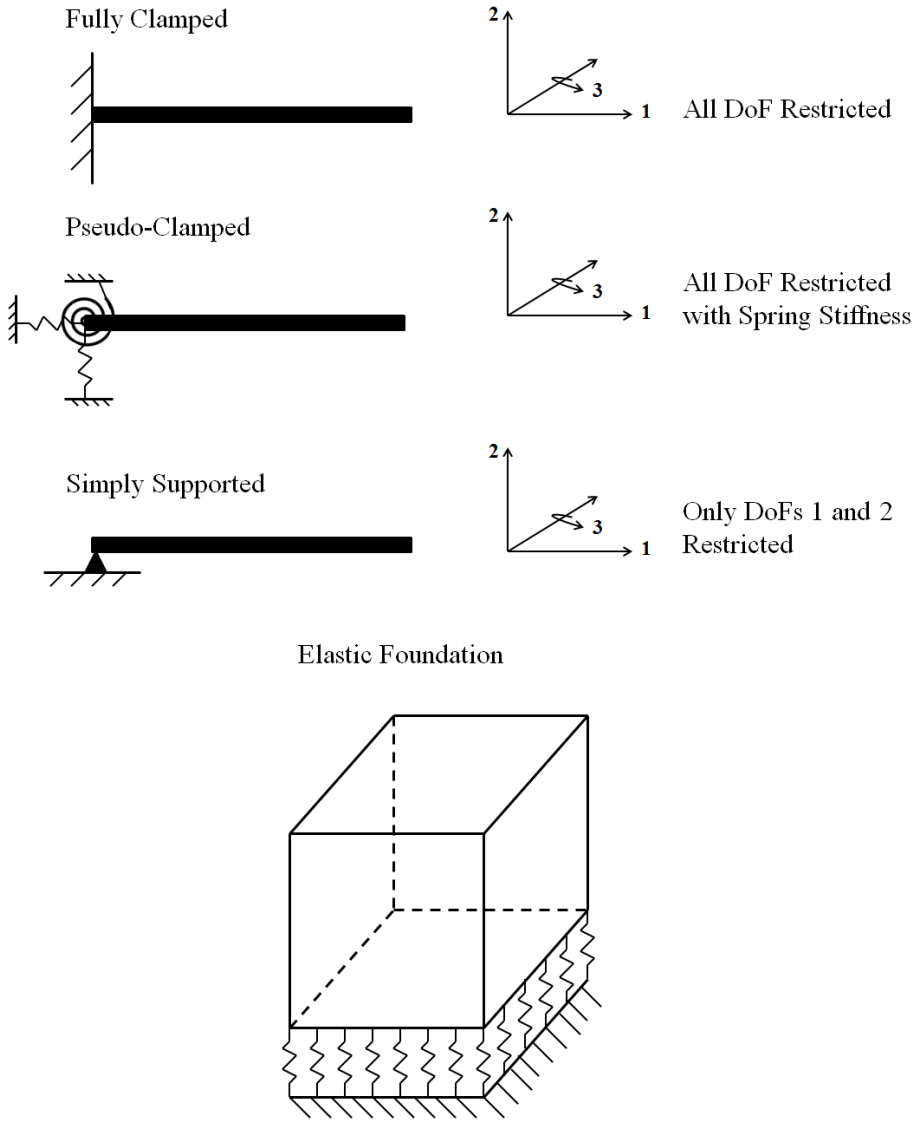

Figure 14: Illustration of Pseudo-clamped Boundary Condition and Elastic Foundation

An experimental design had to imitate the boundary conditions of the vertices of the icosahedron. To produce a boundary condition that lies between the clamped condition and the simply supported condition, support blocks were constructed at each vertex of the triangle. The support blocks have a mass significantly larger than the beams of the triangle, and act as a pseudo-clamped boundary condition. However, the blocks are free

to move so the behavior of the frame is representative of the triangle that is part of the icosahedron structure. Figure 15 shows the Abaqus representation of the experimental triangle designed to replicate one of the triangles of the icosahedron.

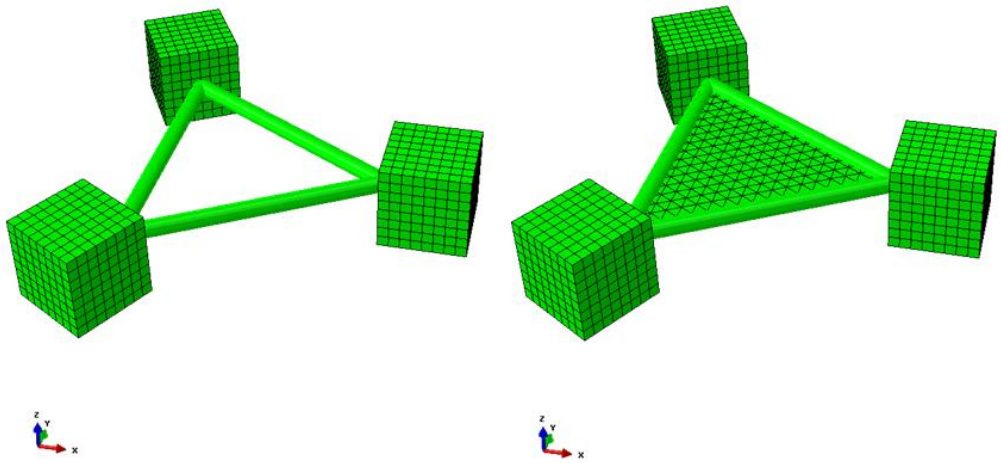

Figure 15: Abaqus Representation of Experimental Test Specimen without Membrane (Left) and with Membrane (Right)

At the base of the support blocks, translational and rotational springs were applied as described in the beginning of the section to replicate the pseudo-clamped boundary condition, and the interaction between the test base and the blocks. In an iterative process of testing the triangle and modeling it in Abaqus, values for the spring stiffness's were determined based on the rigid body mode natural frequencies. An elastic foundation was utilized in Abaqus on the bottom surface of the support blocks to act as the connection with the speaker upon which it was tested. The stiffness per area best representative of the speaker was 1.27 MPa. Additionally, rotational and translational springs were applied to the center node of the bottom surface to represent the correct interaction. The stiffness

of these springs was determined to be 6.8 KPa each. With all of the springs applied to the experimental triangle model, the natural frequencies and mode shapes of the rigid body motion matched with good accuracy as can be seen in the results of Chapter IV. As with the baseline icosahedron model, the beams were modeled using B32 elements, and the membrane was modeled using the S3R elements. Also, the block supports were modeled using a solid 20 node quadratic element designated C3D20R. A total of 1914 elements were used, with 54 elements used for the beams, 324 elements used for the skin, and 1536 elements used for the solid blocks.

A 3-dimensional printer was used to build the experimental triangle and the printing material was VeroBlue plastic. The skin material used to replicate the membrane of the baseline model was Kapton tape. The experimental triangle had three major differences from a single triangle of the previously discussed icosahedron model analyzed in Abaqus: dimensionality, material properties, and beam cross-section. The dimensions of the experimental triangle were constrained by the test setup and the capability of the 3-D printer. To determine the experimental triangle eigenvalues, an input force had to be applied to the structure, and the method chosen was a standard 6-inch speaker. The support blocks of the experimental triangle had to set on the lip of the speaker, and therefore the experimental triangle had to be smaller in dimension than the baseline icosahedron triangle model. Additionally, the 3-D printer could not print a hollow beam, such as the beam of the baseline model, without risking damage to the structure. Therefore, instead of a hollow beam, the experimental triangle had solid beams. Finally, the material used in constructing the experimental triangle was VeroBlue plastic, rather than the Beryllium used in the baseline FEA model. These three major differences did not

change the modal characteristics of the experimental model because the determining factor driving the natural frequencies for the structure is its basic geometric properties, such as long slender beams and an equilateral triangular frame, which was preserved. The dimensions of the experimental triangle and the material properties are listed in Table 6 below.

Table 6: Experimental Triangle Dimensionality

	Dimension	**Units**
Block Support (Height, Width, and Length)	1.1515 (0.02925)	in (m)
Beam Length	3.5335 (0.08975)	in (m)
Beam Radius	0.114 (2.9e-03)	in (m)
VeraBlue Density	0.043 (1190.0)	lb/in^3 (kg/m^3)
VeraBlue Modulus of Elasticity	~362594.3 (~2.50)	lb/in^2 (GPa)
VeraBlue Poisson's Ratio	0.35 (est.)	unit less
Kapton Thickness	0.0059 (1.5e-04)	in (m)
Kapton Density	0.0513 (1420)	lb/in^3 (kg/m^3)
Kapton Modulus of Elasticity	362594.3 (2.5)	lb/in^2 (GPa)
Kapton Poisson's Ratio	0.34	unit less

A standard 6-inch speaker was used to apply a force on the structure, and a laser vibrometer was used to detect the vibration response of the structure due to the input force. Figure 16 displays the entire experimental setup with the test specimen placed

below the laser vibrometer, and the computer hardware utilized to analyze the signal to the left. The vibrometer hardware and software used was manufactured by Polytec. Specifically, the Polytec hardware models for the controller, junction box, scanning head, and PC were: OFV-5000, PSV-E-401, PSV-I-400, and PSV-W-401, respectively. The Polytec software used was version 8.8. Figure 17 shows a closer view of the frame only experimental triangle as well as the frame-skin experimental triangle setup. A periodic chirp signal was input into the speaker at ±2 Volts from 0-2000 Hertz for the frame, and from 0-500 Hertz for the frame-membrane. The Polytec theory manual states,

> Periodic Chirp is designed to excite all FFT (Fast Fourier Transform) lines of the measured spectrum. The time signal is generated out of the spectrum by an inverse Fourier transformation. Typically the magnitude is set for all frequencies to the same value. The phase is generated by an algorithm which maximizes the energy for a given maximum amplitude.
>
> After waiting for steady state conditions the excitation and the response are measured without leakage effects. As all frequencies of interest are excited simultaneously no averaging is required. This is very useful in order to do fast measurements. However, for precise measurements averaging can be used in order to increase the signal-to-noise ratio [26].

Ten averages of displacement were taken at each point to reduce the signal-to-noise ratio using a sample time of 3.2 seconds for the frame, and 6.4 seconds for the frame-skin model in constructing the frequency response plot.

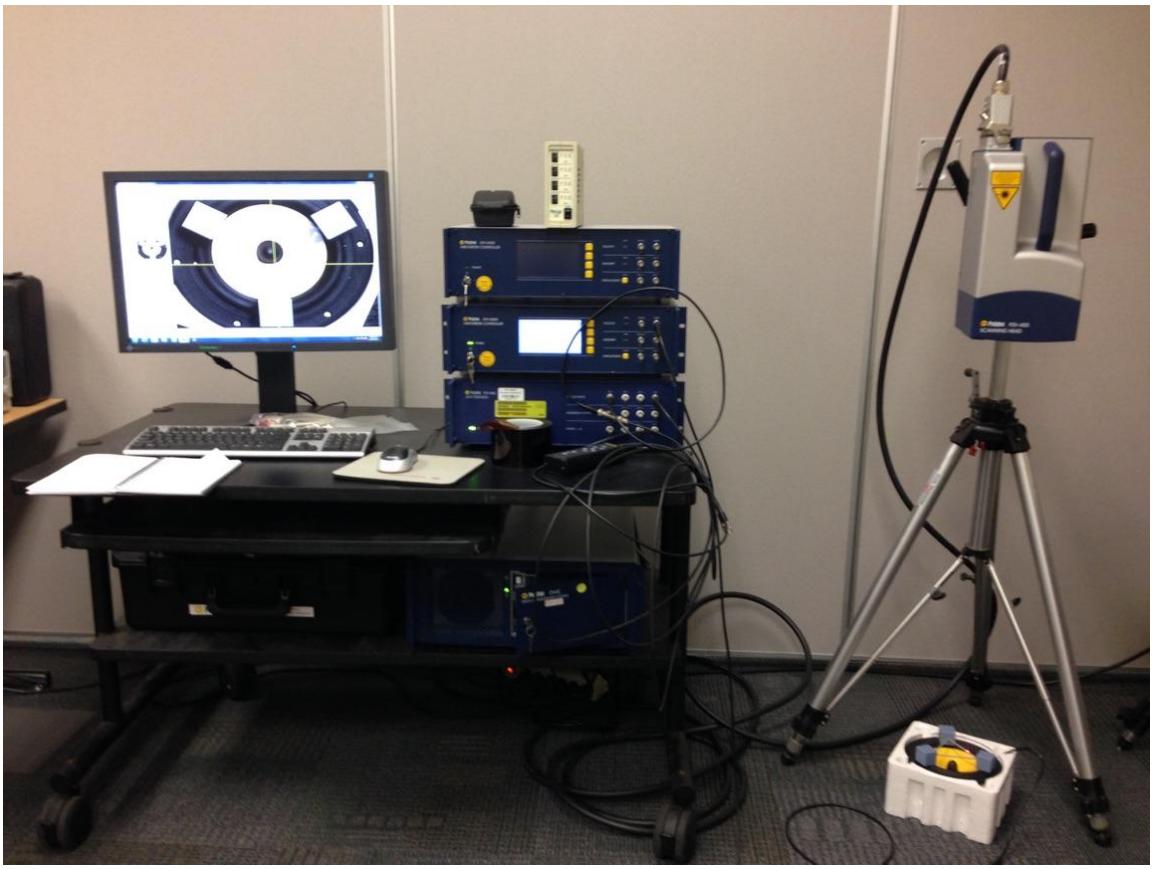

Figure 16: Experimental Setup

Figure 17: Test Specimen – Frame Only (Left) and Frame-Skin (Right)

The process of obtaining the eigenvalues and eigenvectors of the experimental setup is shown in Figure 18. First, the model was created using the Solidworks Computer Aided Design (CAD) software and the 3-D printer. Next, the experiment was setup using the Polytec software, and measurement points were selected for analysis. A periodic chirp signal was input into the speaker, and the laser vibrometer measured the displacement of the selected points on the experimental triangle. The input signal to the speaker and the output signal from the laser vibrometer are analyzed by the software through a Fast Fourier Transform, and the frequency response plot was developed. Additionally, the eigenvectors are displayed by the Polytec software. Results of this process are shown in the following chapter.

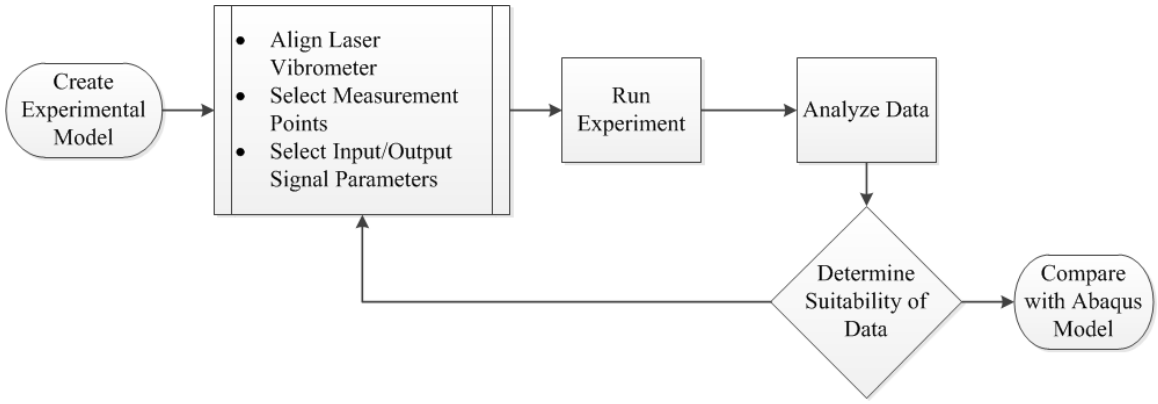

Figure 18: Experimental Analysis Process

Equivalent Stiffness Study

In addition to decomposing the icosahedron into individual parts, a comparison was made to a simple beam structure using an equivalent stiffness to characterize the dynamic behavior of the icosahedron model. This comparison was made to identify similarities to structures with known dynamical behavior, similar to the decomposition of the icosahedron. If similarities could be identified then experiments could be carried out using the simplified model to obtain information on the behavior that would be present in the icosahedron design.

Figure 19 depicts the process of which the comparison of a complex structure can be compared to a simple beam through an equivalent stiffness. Abaqus was used to impart an initial displacement (*D*) on the icosahedron structure and obtain the reaction force (R^{ext}). In a static analysis, force is equal to stiffness multiplied by displacement, or $R^{ext} = KD$ (refer to Equation (9)). With the force and displacement known, stiffness can be calculated. To compare the stiffness of the icosahedron to a simple beam, the known stiffness equation for a beam was utilized. To ensure dynamic similarities, the mass of the icosahedron frame and the equivalent stiffness beam had to be equal as well. Holding the stiffness and mass equal allows for the solution of the beam dimensions and the development of a beam model that can be analyzed.

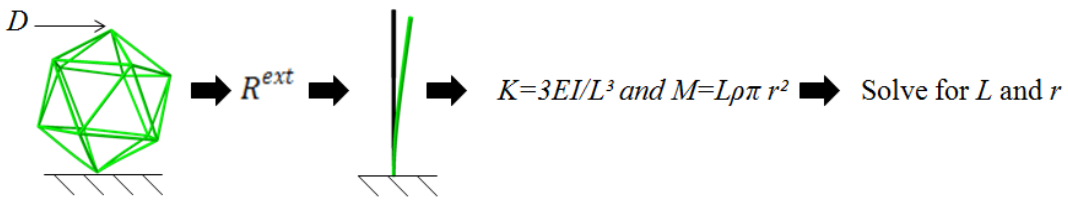

Figure 19: Equivalent Stiffness Comparison Process

The dimensions of the beam with equivalent stiffness and mass to the icosahedron were computed to be 0.3313 meters in length, and 0.0018 meters for the cross-sectional radius. Table 7 shows the natural frequencies calculated for both the simply supported, and the clamped boundary conditions. All values are in units of Hertz. The difference between some of the natural frequencies calculated for the icosahedron frame and for the equivalent stiffness beam is relatively small for certain modes (1.5% error between mode 5 of the clamped frame and the clamped beam). However, the mode shapes associated with those eigenvalues reveal no similarity between the two structures as shown in Figure 20. The first bending mode of the clamped icosahedron frame and the clamped beam have similar mode shapes, as shown in Figure 21, but the eigenvalue is off by 25.8%. The comparison between the icosahedron frame natural frequencies and those of the equivalent stiffness beam did not reveal a relationship strong enough to consider further diagnosis.

Table 7: Natural Frequencies for Equivalent Stiffness Beam

Mode	Icosahedron - Clamped	Beam - Clamped	Icosahedron - Simply Supported	Beam - Simply Supported
1	47.03	59.17	0.00	0.00
2	47.03	59.17	1021.90	166.08
3	83.94	370.68	1021.95	166.08
4	1021.90	370.68	1021.97	664.07
5	1021.97	1037.28	1022.09	664.07
6	1033.62	1037.28	1049.73	1493.16
7	1033.71	2030.85	1049.83	1493.16
8	1048.28	2030.85	1050.07	2652.03
9	1049.73	3353.30	1050.16	2652.03
10	1049.83	3353.30	1053.25	4138.86
11	1096.76	5002.23	1096.76	4138.86
12	1096.87	5002.23	1096.86	5951.37
13	1128.24	6295.90	1097.12	5951.37
14	1162.04	6975.07	1177.59	8086.82
15	1162.07	6975.07	1177.63	8086.82
16	1178.18	9268.81	1178.18	10542.10
17	1178.22	9268.81	1178.22	10542.10
18	1215.03	9671.95	1178.72	12591.80
19	1215.04	11880.00	1304.00	13313.60
20	1232.33	11880.00	1314.99	13313.60

The equivalent stiffness study was conducted as an alternative way to develop a reduced order volume that could be built and tested in lieu of the entire icosahedron. The decomposition of the icosahedron model into its individual parts revealed strong similarities between the single face of the icosahedron and the structure as a whole. However, the equivalent stiffness method was determined to be non representative of the entire icosahedron.

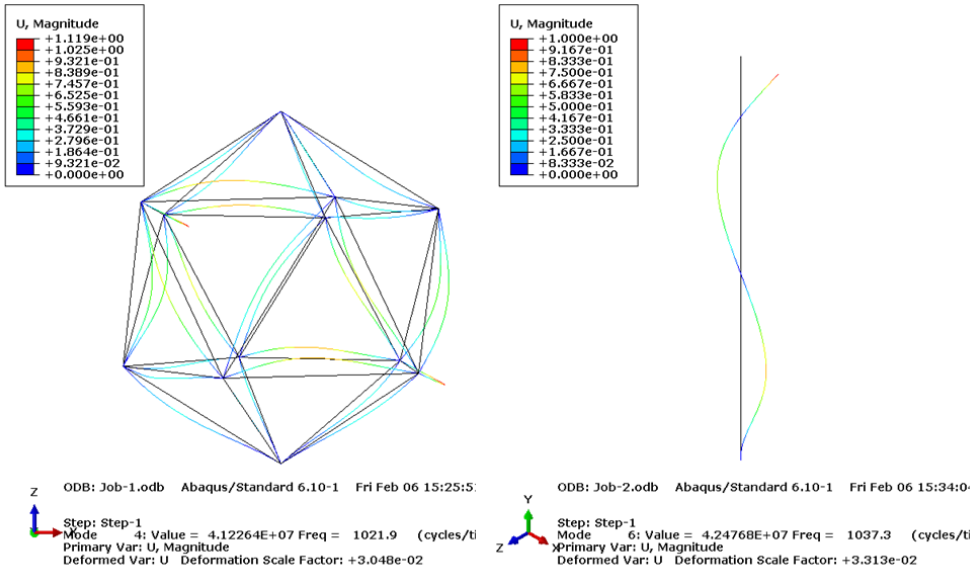

Figure 20: Mode Shape Difference for Icosahedron Frame and Equivalent Stiffness Beam

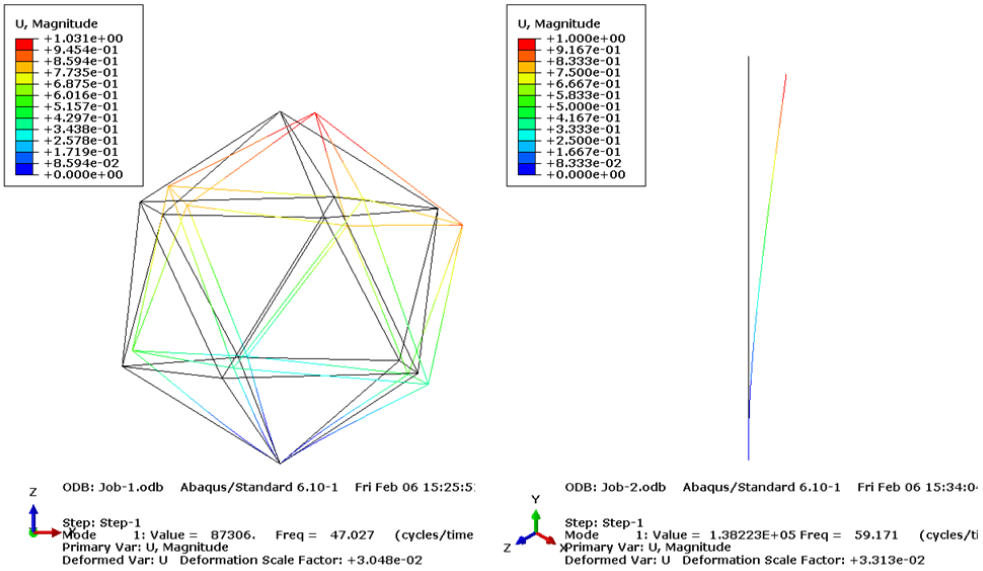

Figure 21: Similar Mode Shapes for Icosahedron Frame and Equivalent Stiffness Beam

Time Step Study

A complete dynamic analysis using FEA requires a sufficient number of elements in the model, the correct type of elements for the structure, and the appropriate integration time step size for calculating the solution. The type of elements used, and the number necessary to calculate an accurate solution was presented in previous sections. This section establishes the time step required for calculating the solution. Referring to Equation (14), the numeric solution to the structural analysis problem is dependent upon the size of the time step. If the specified time step is too large a solution may be indeterminable, or inaccurate.

A common method used to select the correct time step is to obtain the displacement results for varying time steps, and utilize the power spectral density function to analyze the eigenvalues admitted from the solution. In this research, the time step variation analysis was executed using a single beam of the icosahedron discretized into eight B32 beam elements. Simple supports at each end were the boundary conditions for the beam, and an initial displacement of ~0.6% of the length of the beam was placed at the quarter beam position. The initial displacement was chosen so the response would remain in the linear range. The nonlinear solution option was selected in Abaqus, although the same results would have been obtained if a linear response was requested, because of the size of the initial displacement. The initial displacement was removed and the free response of the beam as a function of time was generated using Abaqus. This simple problem allowed for a comparison to the analytical values of the eigenvalues found in the literature. Figure 22 displays the simple beam setup input to Abaqus, and Table 8 shows the beam natural frequencies calculated analytically, and through FEA using Abaqus.

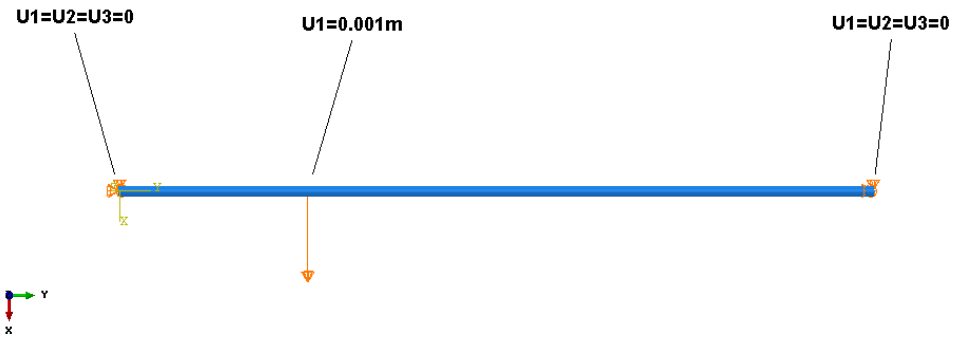

Figure 22: Boundary Conditions and Initial Displacement for Time Step Study

Table 8: Analytical and Abaqus Calculated Natural Frequencies for Simple Beam

Mode#	Analytical	Abaqus	%Error
1	824.0	822.83	0.14
2	3296.02	3282.34	0.42
3	7416.04	7365.15	0.69
4	13184.08	13088.0	0.73
5	20600.12	20541.3	0.29

Table 9 shows the beam natural frequencies calculated using the PSD method. The accuracy of the calculated eigenvalues clearly increases as the time step decreases, with less than one percent error calculated for all natural frequencies using a time step of 1e-6 seconds. Using a time step of 1e-5 seconds produces the first three eigenvalues with an error of less than 2.5%, although the accuracy declines at the higher number modes. The fifth natural frequency calculated using a time step of 1e-5 seconds has an error of 12.3%. Error percentages for both Table 8 and Table 9 were calculated based on the analytical values. Eigenvalues are not presented in Table 9 for the fourth mode because of the location which the displacement data was analyzed, called the reference point. The

reference point in this case is the quarter beam position, and the fourth mode shape has a node directly at that point. As Avitabile states in *Experimental Modal Analysis*, "the reference point cannot be located at the node of a mode otherwise that mode will not be seen in the frequency response function measurements and the mode cannot be obtained" [18].

Table 9: PSD Calculated Natural Frequencies for Simple Beam

Mode#	dt = 1e-4 s	dt = 5e-5 s	dt = 1e-5 s	dt = 5e-6 s	dt = 1e-6 s	%Error
1	801.78	823.1	822.41	822.31	822.24	0.21
2	2516.7	3003.3	3267.4	3289.3	3288.96	0.21
3	3608.02	5250.3	7223.8	7334.15	7355.7	0.81
4	Undetected	Undetected	Undetected	Undetected	Undetected	N/A
5	Undetected	Undetected	18048.5	19780.0	20511.6	0.43

Displacement plots for the various time step values are shown in Figure 23 and Figure 24. Table 9 showed the solutions dependence on choice of time step in the accuracy of the response. The displacement plots also show the importance of selecting a proper time step. Larger value time steps result in inaccurate data that decrease in amplitude over the course of the simulation. The displacement plot in Figure 24 shows that a time step of 1e-5 seconds or less produces an almost identical response. Figure 25 and Figure 26 show the PSD plots as a function of decreasing time step. These plots clearly show a certain time step is required for an accurate solution; too large of time step leads to displacement plots not representative of the correct response, and the values of the natural frequencies obtained by the PSD plots vary by significant amounts, or do not appear at all. Additionally, Figure 25 shows the PSD plot is cut off before a frequency of interest (20 kHz) because of the lack of data points.

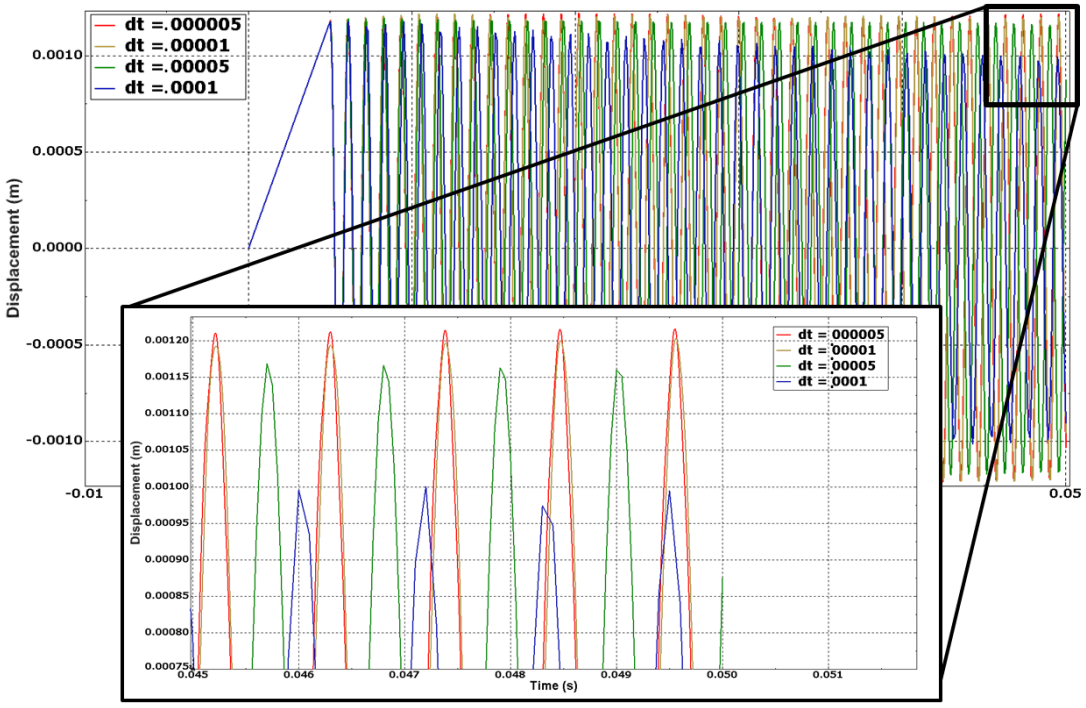

Figure 23: Displacement versus Time for First Four Time Step Values

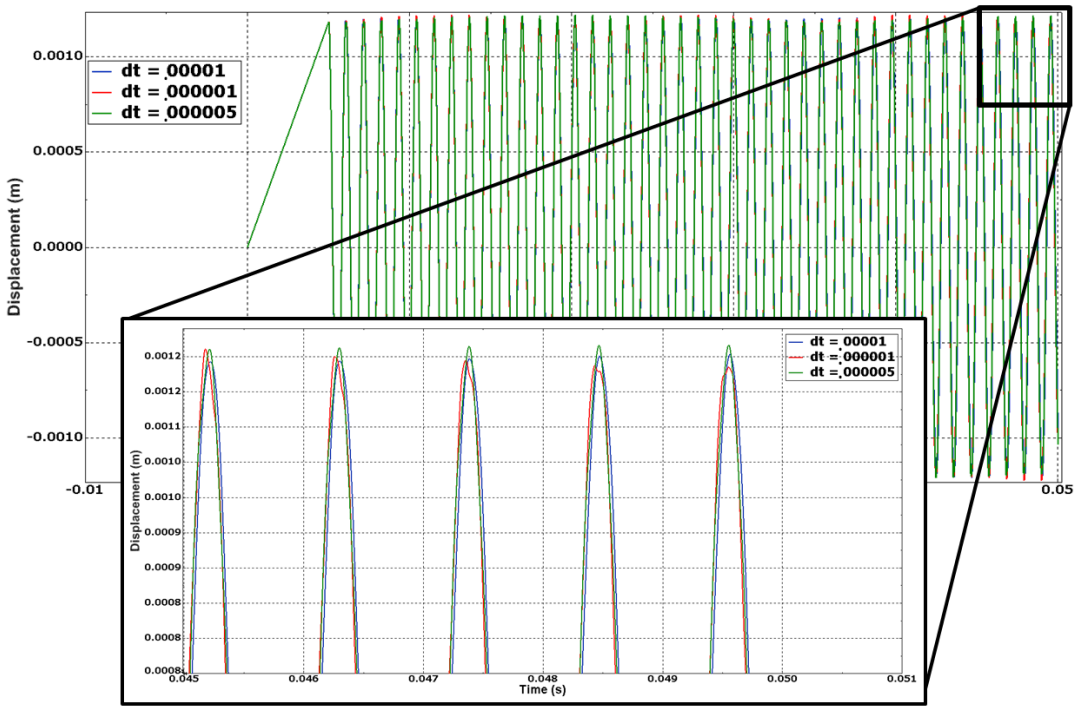

Figure 24: Displacement versus Time for Last Three Time Step Values

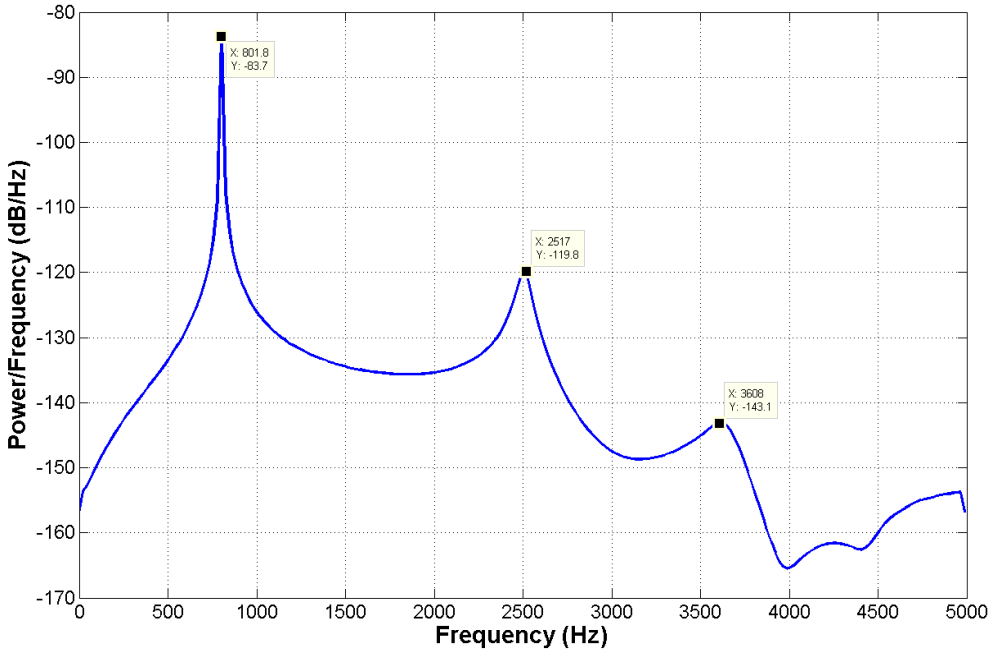

Figure 25: PSD for Time Step of 1e-4 seconds

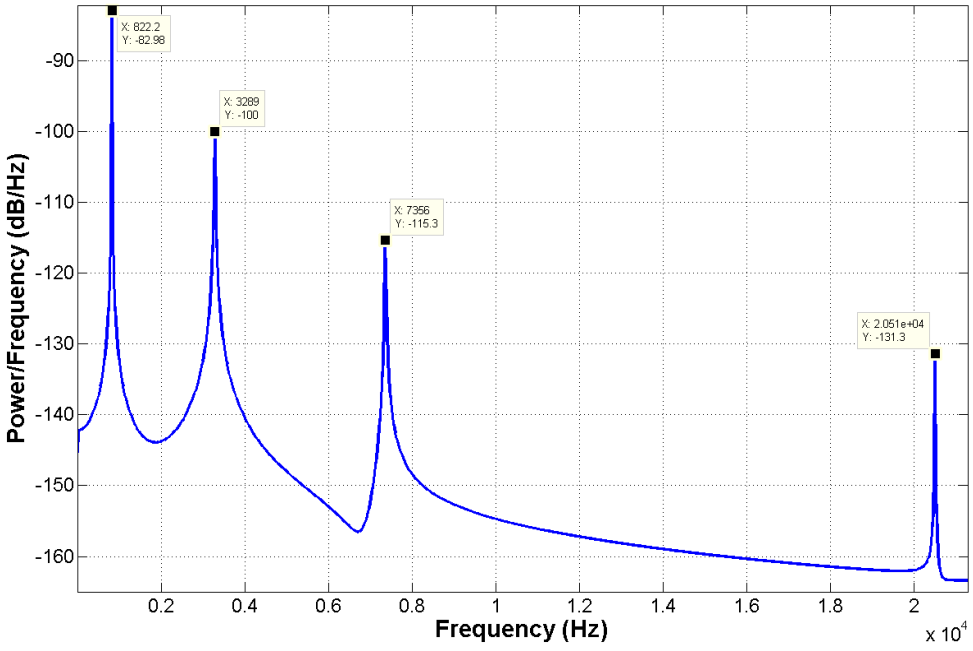

Figure 26: PSD for Time Step of 1e-6 Seconds

Some error can be expected in running computer simulations because the Abaqus dynamic/implicit solver "generally introduces some degree of numerical damping" that could be responsible for the difference in natural frequency determined using the power spectral density [17]. Further decreasing the time step value would likely lead to more accurate results; however, a significant amount of computational power and memory is required to decrease the value more than 1e-6 seconds and will not be done for this research as a percentage error of less than one percent was considered sufficient. In most cases, only the first few natural frequencies and mode shapes are compared to determine similarities. Therefore, a time step value of 1e-5 seconds or less was used for the remainder of the analysis in this thesis.

Summary

This chapter presented the development of a dynamic model starting with the baseline model originally developed by Adorno-Rodriguez for a static analysis. The icosahedron was decomposed into its individual parts to simplify the structure, and obtain a representable model that could be used in experiments because the full is challenging to construct. An experimental setup was detailed as an attempt to verify the accuracy of the solutions obtained using the Abaqus FEA program. Additionally, an equivalent stiffness method was discussed to simplify the complex icosahedron into a well-understood structure. Finally, the time step necessary for a dynamic analysis was considered to ensure the accuracy of the model.

IV. Analysis and Results

Chapter Overview

Modeling techniques for analyzing the icosahedron structure dynamically were detailed in the previous chapter as well as a method for verifying the computer model experimentally. This chapter will describe the results of those methods as they were applied, and consider the relevance of the information in terms of three basic questions:

- Can a simplified model be created to test a representable structure in reality?
- At what applied load and load rate do the response characteristics of the structure become dominated by dynamics?
- What is the behavior of the structure when subjected to dynamical loading for various boundary conditions?

The results of the experimental tests are presented along with comparisons to the related computer models in the first section. Next, an analysis of the loading rate is considered in order to impart a dynamic response. Finally, various loading scenarios are developed and the behavior of the response is characterized.

Experimental Results

Given the relationship between the icosahedron frame and the frame-skin models to the single triangle of the icosahedron, an experimental setup was created to test a representable volume in an effort to validate the FEA model that has been the basis of the research. The experimental setup was explained in detail in the previous chapter, and the results are provided in this chapter.

The results of decomposing the icosahedron into its individual parts and analyzing the natural frequencies and mode shapes of each component using various boundary conditions led to an experimental triangle that was explained previously. In an iterative process, the experimental triangle was created, tested, and the FEA model was updated to reflect the results of the testing. A final FEA model was developed matching the first several mode shapes and natural frequencies of the test specimen. Figure 27 displays the first six mode shapes observed in testing calculated by Abaqus. Only the relevant modes are displayed, related to the speaker's vertical translation input force.

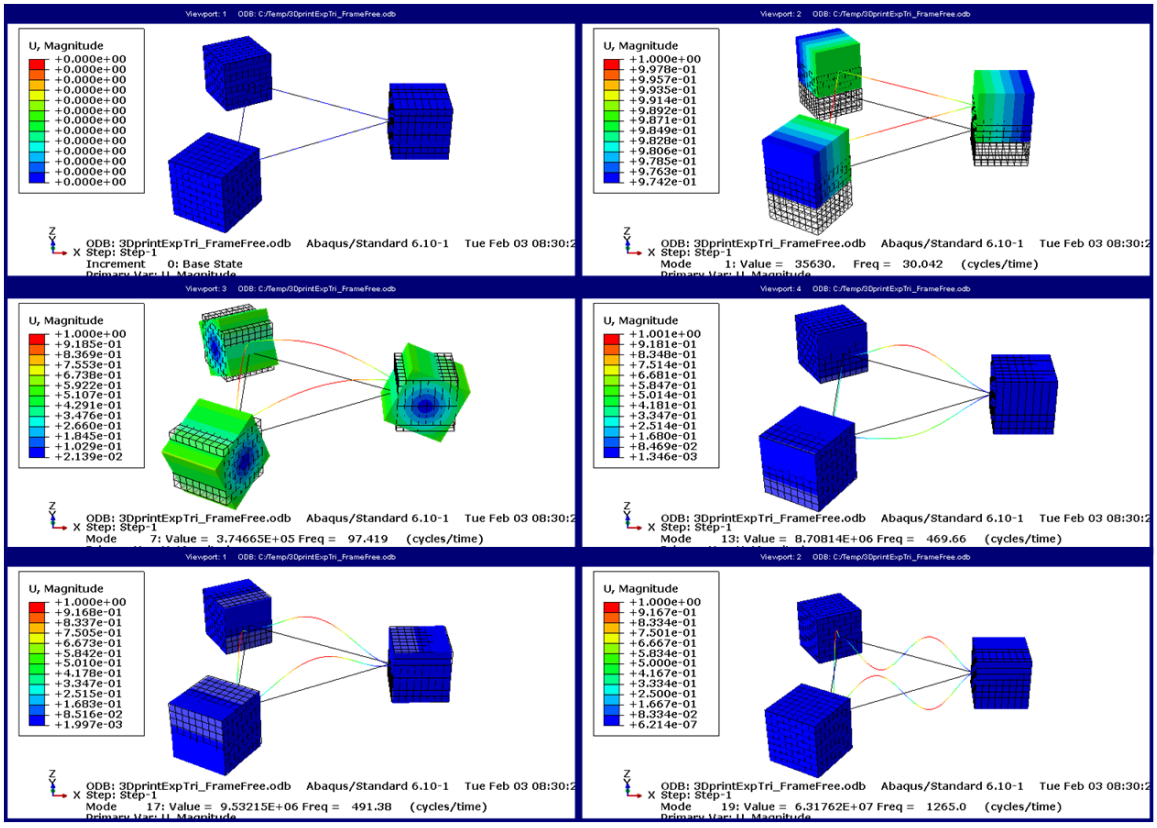

Figure 27: Modes 1 through 6 – FEA Experimental Triangle (Frame)

Figure 28 shows the points of measurement for the experimental triangle setup, as well as the view seen from the laser vibrometer position. As the drive signal is input to the speaker, the vibrometer measures displacement at each point over a number of periods of the input signal. The software takes the average output movement of the triangle and creates a frequency response plot for the entire structure. The mode shapes of the experimental triangle are shown in Figure 29, and the frequency response plot is shown in Figure 30. In Figure 29, the top picture for each natural frequency is the movement as the triangle beams move away from the speaker, while the bottom picture is the movement into the speaker to show the full range of motion at a given frequency. The black dots in Figure 29 represent the initial point on the structure before any displacement, and the color of the squares represent the distance from the original position. Red is the greatest positive distance from the reference point, and blue is the greatest negative distance from the reference position. The color graduated bars in between the extremes mirrors the scale used by the FEA plots shown in Figure 27.

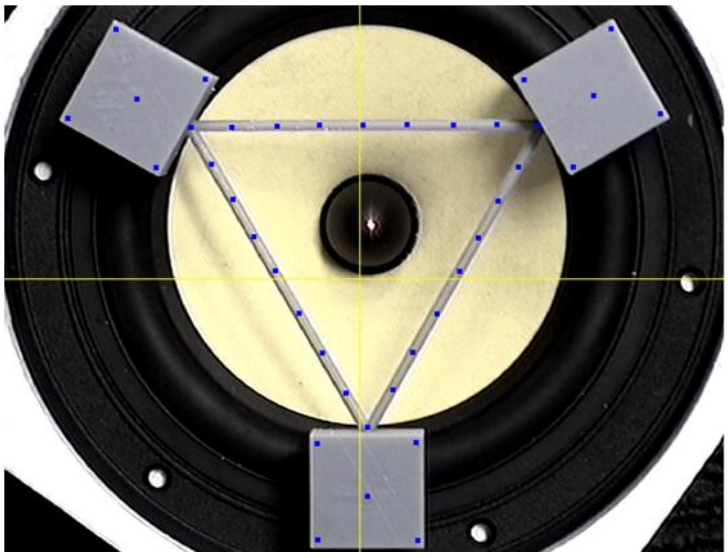

Figure 28: Points of Measurement for Experimental Triangle

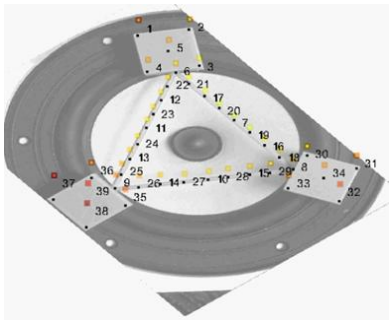

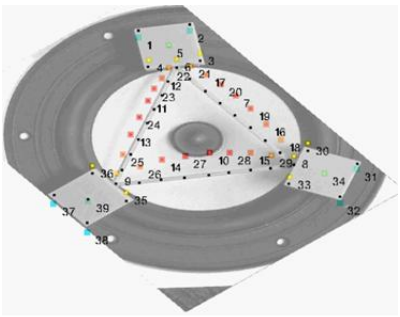

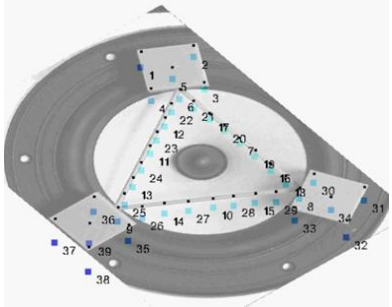

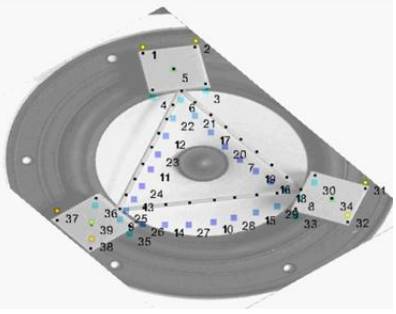

Mode #1: 29.6875 Hz	Mode #2: 97.1875 Hz

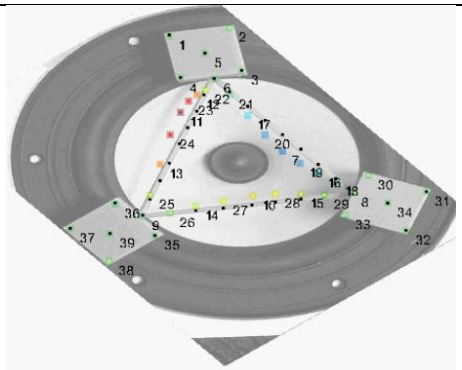

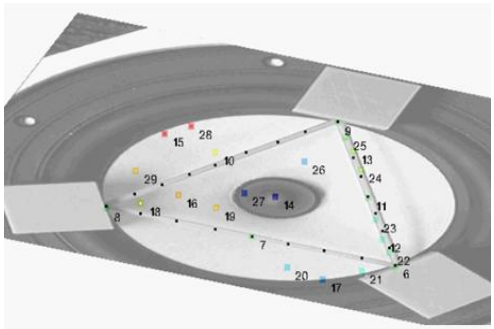

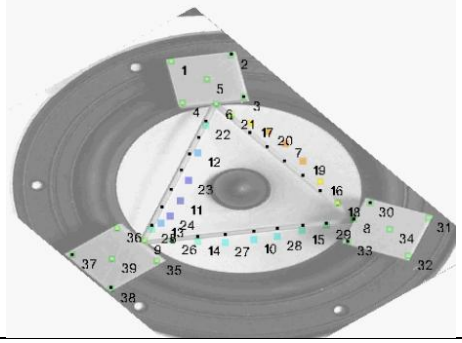

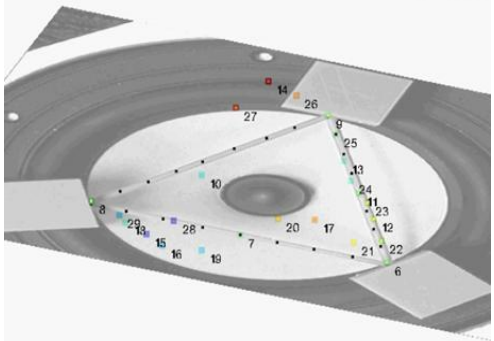

Mode #3: 464.0625 Hz	Mode #5: 1280.938 Hz

Figure 29: Experimental Triangle Mode Shapes and Natural Frequencies (Frame)

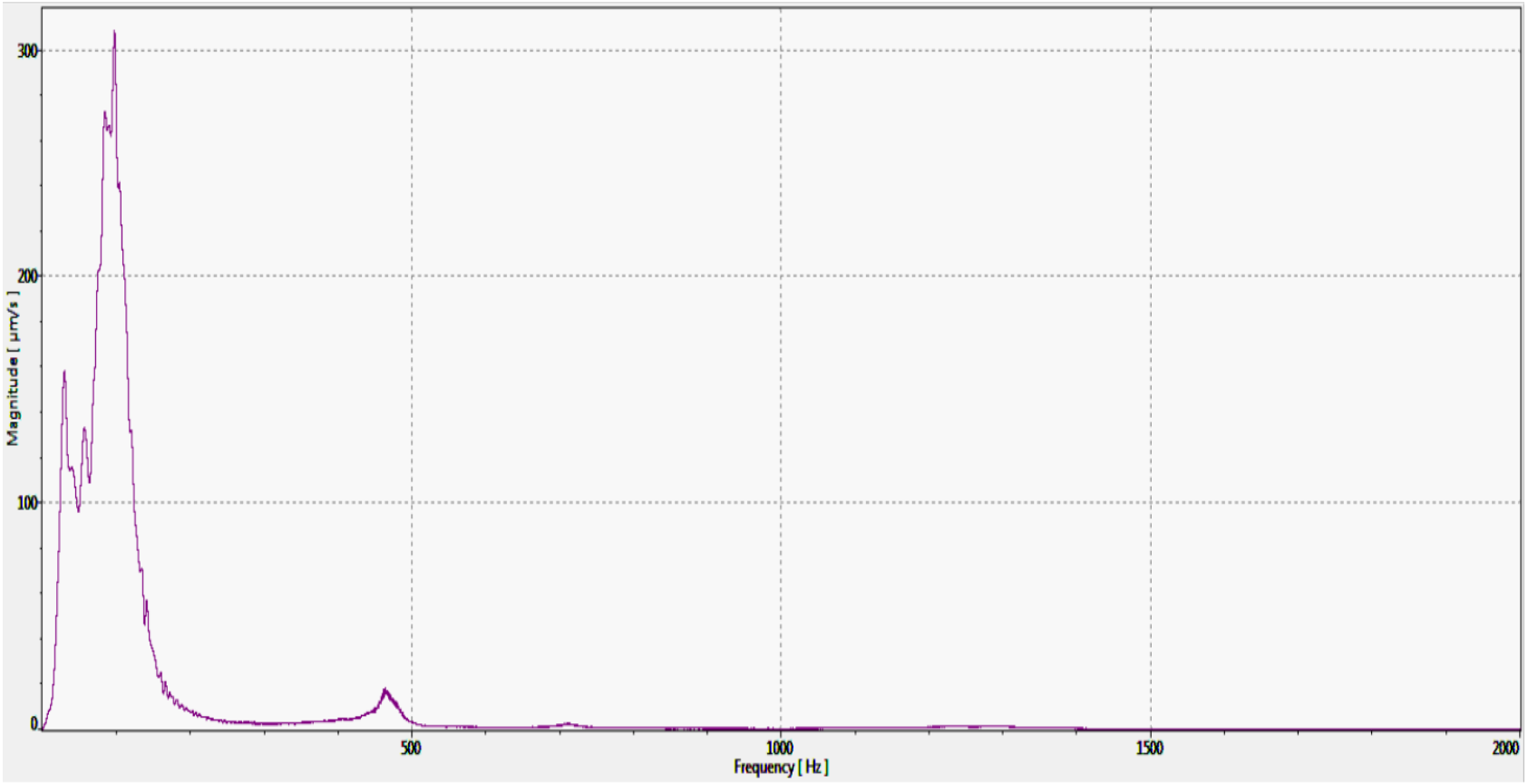

Figure 30: Frequency Response Plot for Experimental Triangle (Frame)

A variety of factors impacted the accuracy of the results obtained from this experiment, including noise and input signal parameters. Variations on the parameters did not have a large effect on the natural frequencies and mode shapes detected by the laser vibrometer, but there was some difference. Using ten averages at each point reduced the effect of noise; however, it cannot be eliminated. The experimental triangle and the FEA triangle produced very similar natural frequencies and mode shapes with the exception of the fifth mode shown in Figure 27. The first bending mode (491 Hz) of the frame beam was not detected in the experiment. A likely explanation for the lack of detection of the first bending mode is the difference between natural frequencies and operating deflection shapes arising from the experimental data. Operating deflection shapes are the mode shapes that are determined given all of the outlying circumstances. In a perfect experiment the operating deflection shapes would be the same as the true mode shapes. Factors such as noise, input parameters, and modal coupling can cause differences between the two. The first bending mode of the frame beams (mode 5 shown in Figure 27) lies very close to the mode before it, where two beams bend in opposite direction while the third beam remains nearly stationary. In the experimental setup there could be coupling between these modes and there could be a lack of input signal necessary to generate the mode described as the first bending of the frame beam.

In addition to comparing the experimental triangle with the FEA triangle, a reconstruction of the entire icosahedron frame was conducted to determine if the experimental triangle was truly representative of the whole icosahedron frame. The icosahedron frame was reconstructed in Abaqus using the material properties of the 3-D printer material and the geometric dimensions were the same as the triangle. Table 10

displays the related eigenvalues of each model in Hertz. The first two rows of the table show the rigid body modes (RBM) that are associated with the speaker setup and therefore undetected on the icosahedron frame model.

Table 10: Natural Frequencies of FEA Experimental Triangle Frame, Experimental Triangle Frame, and FEA Icosahedron Frame

Mode #	Icosahedron Frame	Experimental Triangle Frame - Abaqus	Experimental Triangle Frame - Vibrometer
RBM	0.0	30.0418	29.6875
RBM	0.0	97.4186	97.1875
1	400.47	469.6590	464.0625
2	457.21	491.3780	Undetected
3	1260.000	1266.4200	1280.938

The information contained in Figure 27, Figure 29, and Table 10 demonstrates a strong relationship between the FEA experimental triangle model, the real experimental triangle, and the icosahedron frame they were designed to replicate. Figure 31 displays the mode shapes of the entire icosahedron frame, and a single triangle of the frame has the same mode shapes as the experimental triangle models of Figure 27 and Figure 29. The natural frequencies of the three designs varies by at most 16% from the icosahedron frame to the experimental triangle for the first mode; however, this difference can be explained by the various factors affecting the model as detailed earlier, and more accuracy could be achieved with a more rigorous test setup and model construction. Additionally, more accurate material properties may need to be applied to the FEA model to achieve less error between the Abaqus results and the experimental setup.

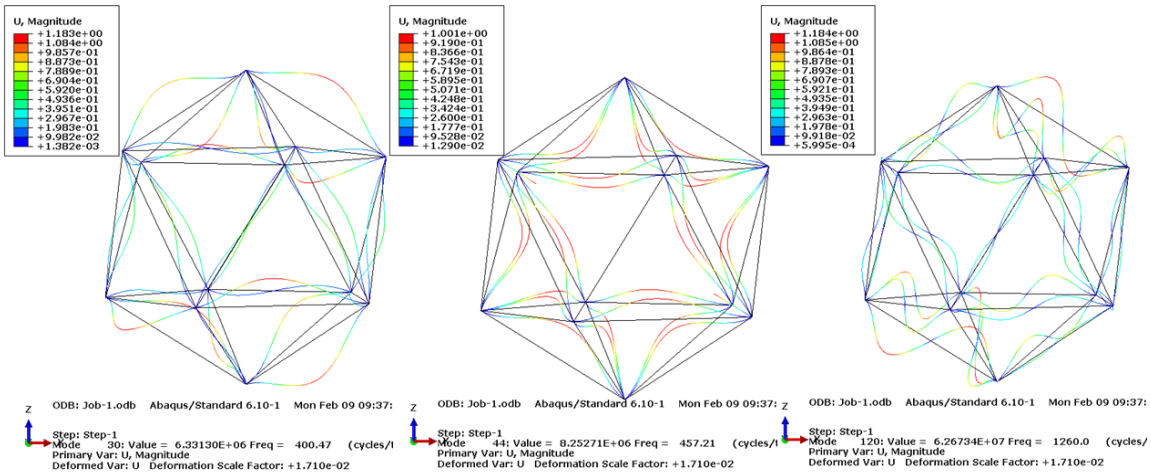

Figure 31: Mode Shapes Associated with Experimental Triangle

Similar to the experimental setup with the triangle frame, the same analysis was completed with the Kapton skin placed on the frame model. The experimental frame and skin model natural frequencies and mode shapes are shown in Figure 32 as computed by Abaqus. The points of measurement are shown along with the experimentally computed eigenvalues and eigenvectors in Figure 33. And the frequency response plot is shown in Figure 34.

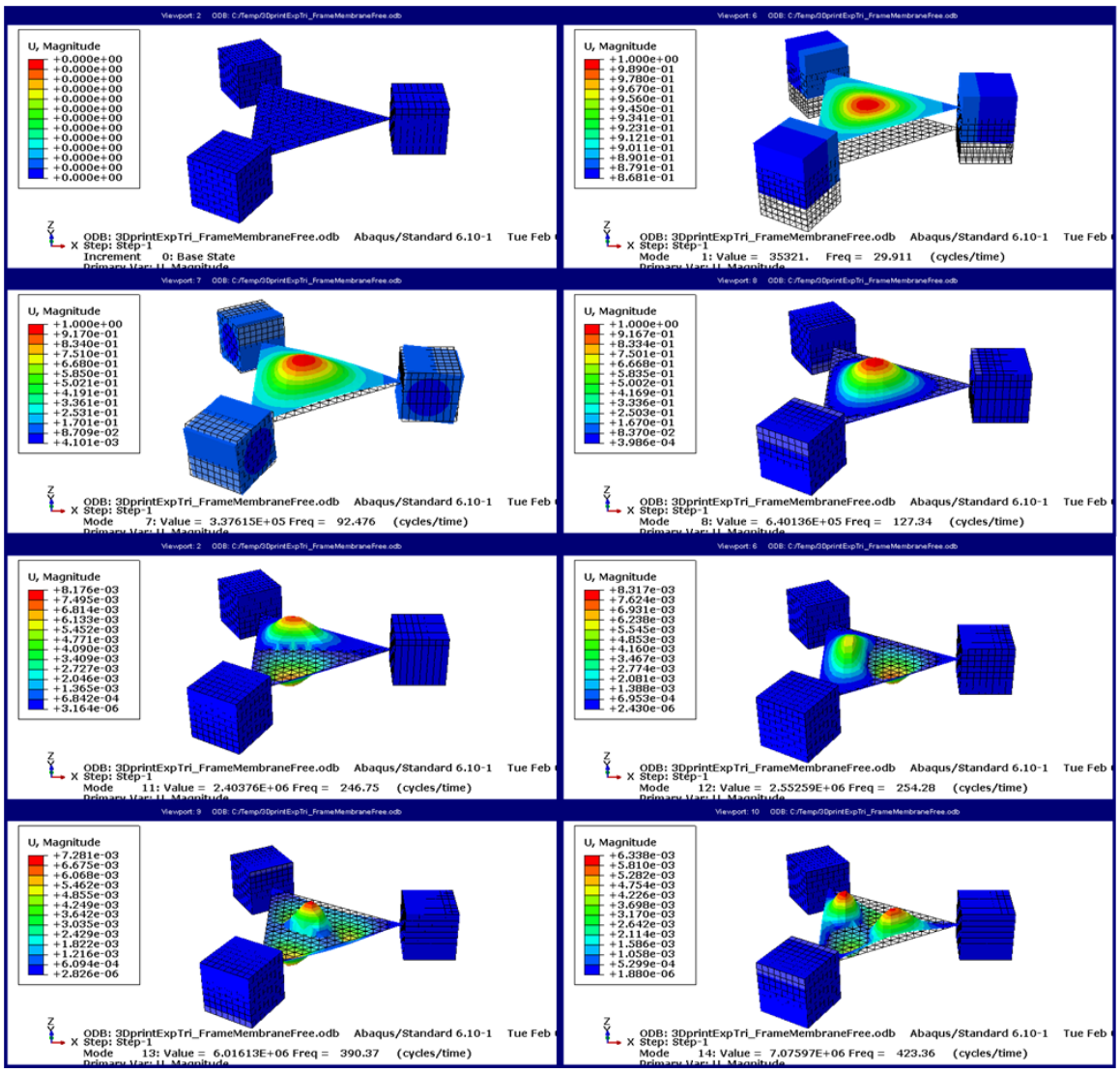

Figure 32: Modes 1 through 8 – FEA Experimental Triangle (Frame-Skin)

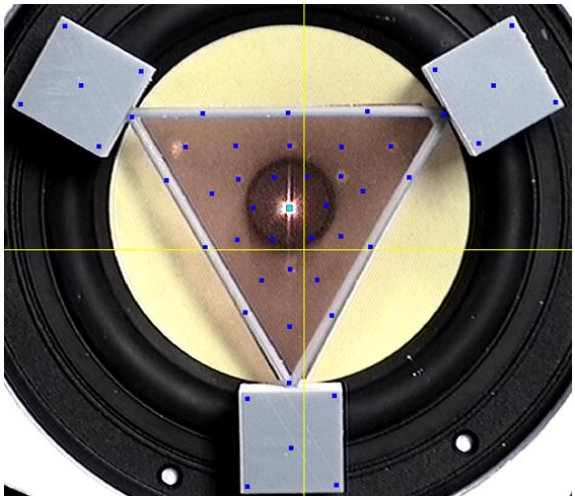

Measurement Points – Experimental Triangle with Skin

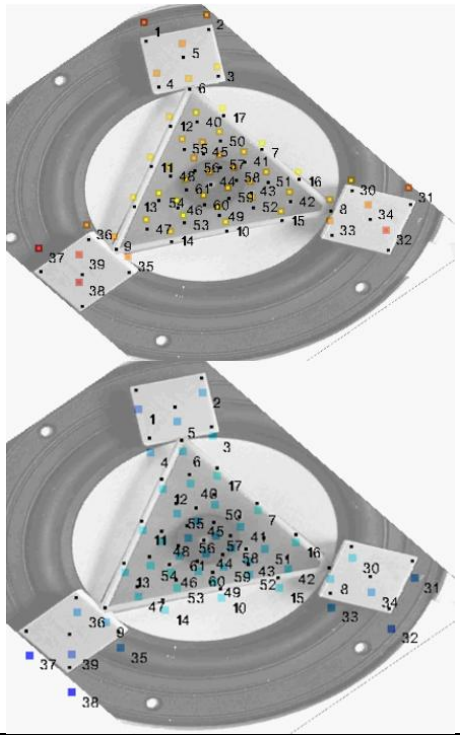

Mode #1: 36.25 Hz

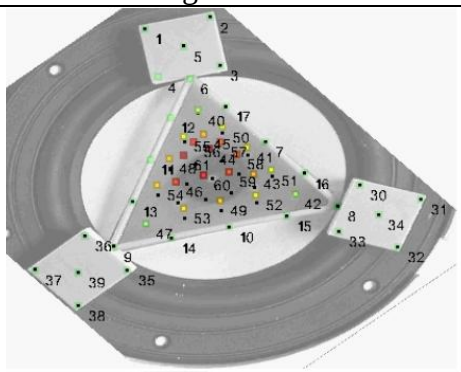

Mode #2: 122.03125 Hz

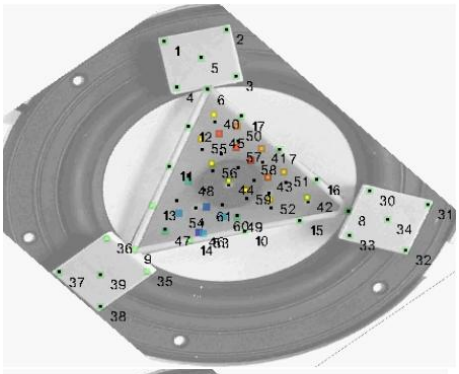

Mode #3: 216.5625 Hz

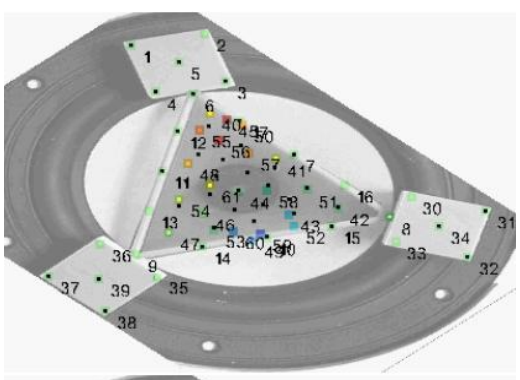

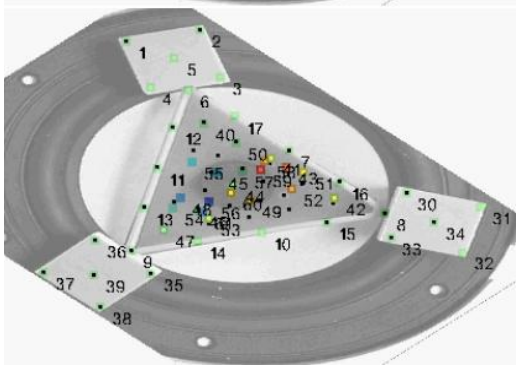

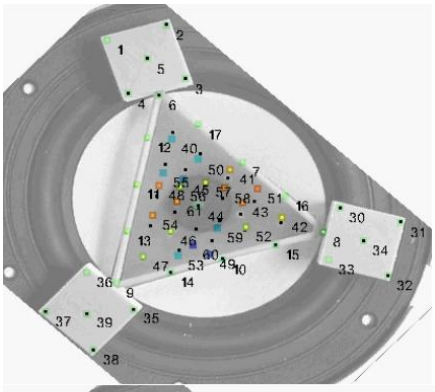

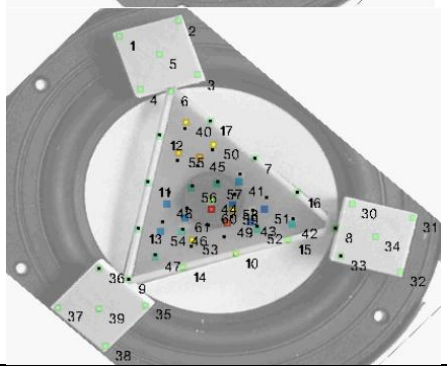

Mode #4: 240.9375 Hz	Mode #5: 361.5625 Hz

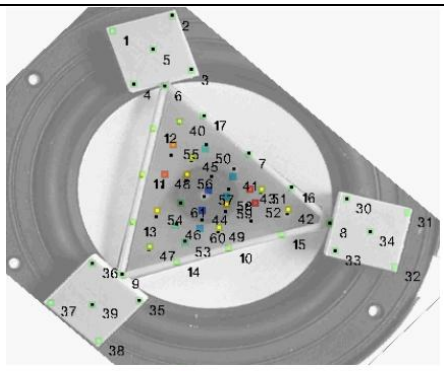

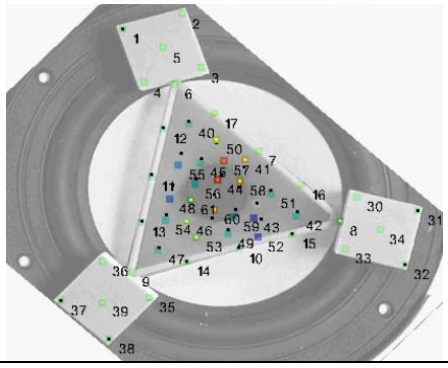

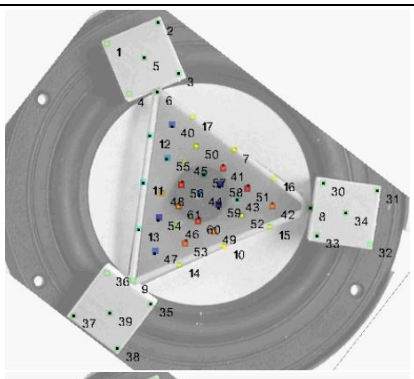

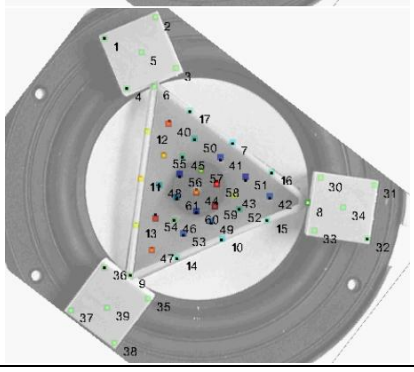

Mode #6: 380.46875 Hz	Mode #7: 472.34375 Hz

Figure 33: Experimental Triangle Mode Shapes and Natural Frequencies (Frame-Skin)

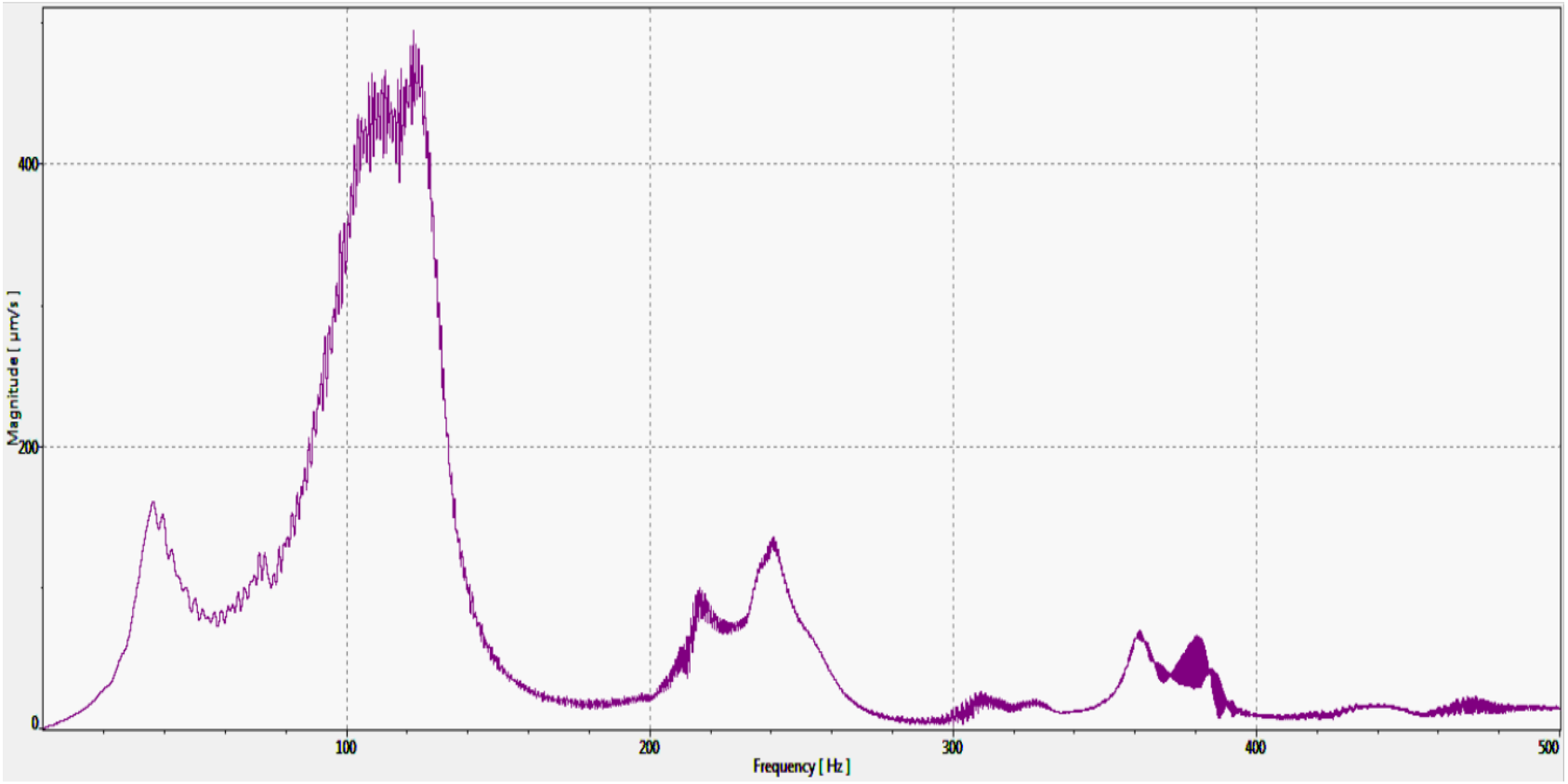

Figure 34: Frequency Response Plot for Experimental Triangle (Frame-Skin)

Table 11 lists the natural frequencies associated with the FEA experimental triangle with skin, true experimental triangle, and the icosahedron with skin. Figure 35 displays the mode shapes of the icosahedron. As with the frame only model, the relationship between the experimentally calculated operating deflection shapes and those of the FEA models is strong. Eigenvalues detected in the experimental analysis are shown in the FEA triangle and the icosahedron model as well, and the mode shapes associated are comparable between all three. Results of the experimental analysis imply a single triangle of the icosahedron is representable of the entire structure, and the modeling techniques used are accurate.

Table 11: Eigenvalues of FEA Experimental Triangle Frame, Experimental Triangle Frame, and FEA Icosahedron Frame

Mode #	Icosahedron	Experimental Triangle Frame and Skin - Abaqus	Experimental Triangle Frame and Skin - Vibrometer
RBM	0.0	29.9113	36.25
RBM	0.0	92.4764	Undetected
1	125.667	127.3380	122.03125
2	252.141	246.7550	216.5625
3	261.387	254.2790	240.9375
4	Undetected	Undetected	361.5625
5	411.452	390.3720	380.46875
6	478.173	423.3630	472.34375

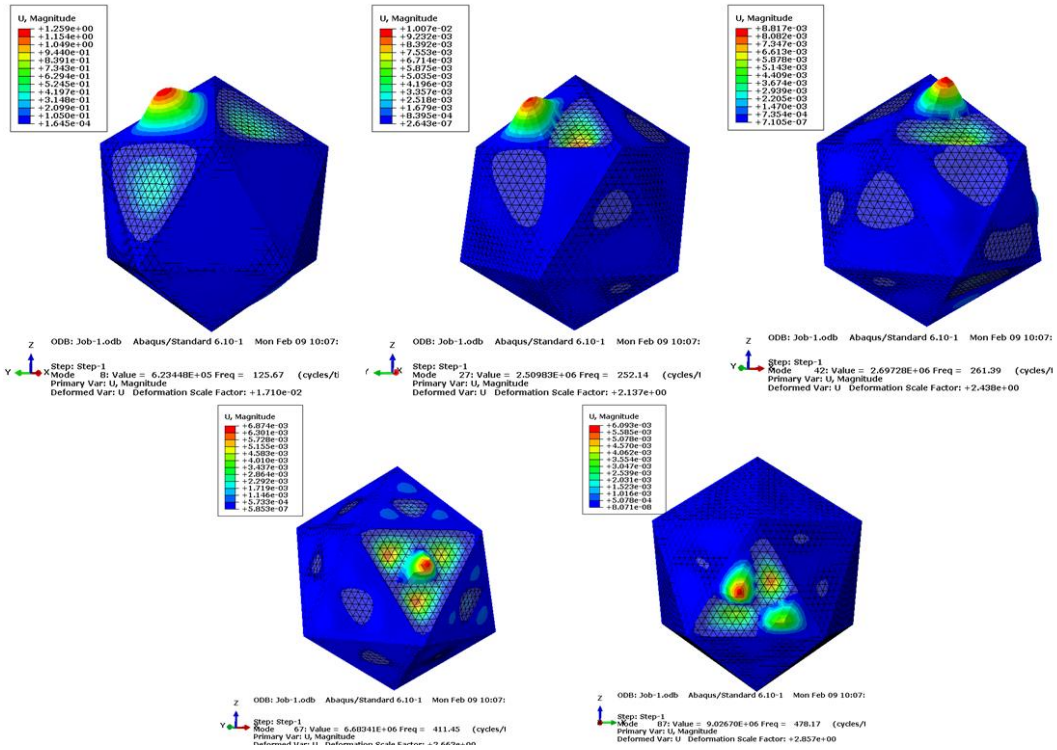

Figure 35: Mode Shapes Associated with Experimental Triangle with Skin

Chaotic Behavior Analysis

In addition to validating the baseline model developed in previous research, a dynamic analysis of the icosahedron frame *snapback* behavior reported by Adorno-Rodriguez is conducted to identify nonlinear instability characteristics of the design. Adorno-Rodriguez compares the *snapback* behavior to the buckling of a thin shell, where an instantaneous reversal of geometry occurs, but the structure retains a load-bearing capacity. In the previously mentioned research, the behavior was observed for two of the boundary conditions considered. Figure 36 shows the different boundary conditions considered, and the *snapback* behavior seen in the first and second boundary conditions for the static loading case. This behavior "indicates a beam withdrawal, or change in displacement direction, while still taking on load. Even though the slope reverses, there is

no softening, therefore the beam does not collapse" [7]. The results are hypothesized to be chaotic behavior present in the standalone frame model. To validate the theory of chaotic behavior in the icosahedron frame, a dynamic analysis is performed and the methods described in Chapter II are applied.

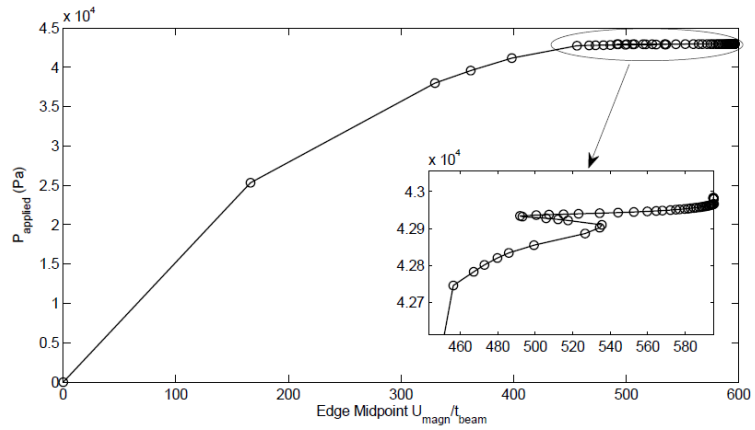

(a) Boundary Condition 1

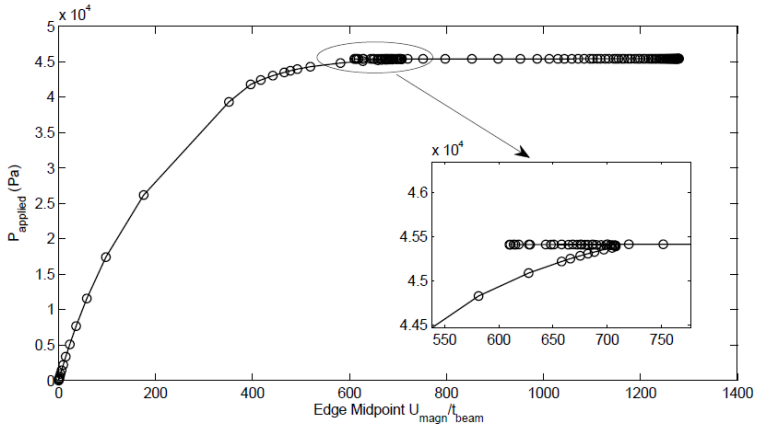

(b) Boundary Condition 2

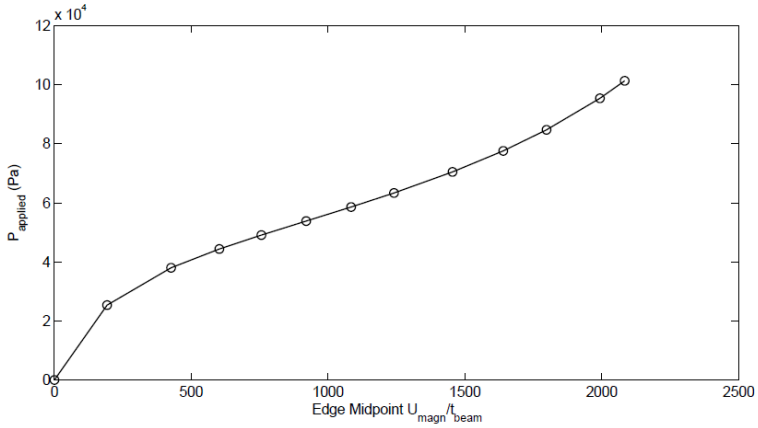

(c) Boundary Condition 3

Figure 36: *Snapback* Behavior Observed in Unsymmetrical Boundary Conditions [7]

Load Rate Analysis

One consideration necessary with a dynamic analysis, but not a static analysis, is the rate which a load is applied. In the case of a static analysis, the load is applied in a manner in which the structure is held in equilibrium and acceleration is equal to zero. A dynamic response will appear similar to the static response if the load is applied at a slow rate. Therefore, to evaluate the rate which a reasonable dynamic response could be produced and to define the line between dynamic and static loading, an analysis of ramped loads was considered.

The *snapback* behavior can be seen to occur at approximately 45% of Sea Level pressure (~45 kPa) for what is called "Boundary Condition 1" (BC1) and "Boundary Condition 2" (BC2) in the plot of the applied load versus displacement of Figure 36 [7]. "Boundary Condition 3" (BC3) does not display the same behavior at any point up to 100% of Sea Level pressure. Figure 37 shows BC3 and the loading applied to the icosahedron frame through reference points at the center of gravity of each triangle, as well as the midpoint node on the lower beam where all displacement data is collected. The midpoint node was used because the icosahedron deforms symmetrically, and all midpoint nodes on all beams have equivalent displacement. Also, it is the reference point referred to in previous research, and has the greatest displacement of any node on the structure. The concentrated load applied to the reference points was distributed to the beams using a coupling constraint in Abaqus. The coupling constraint allows the beams to experience an equivalent load to one that would be applied if a triangular skin with an applied pressure was tied along the edges. Adorno-Rodriguez conducted a study to ensure

the applied load experienced by the beams was identical using the reference point and coupling constraint method, or using a skin tied to the beams [7].

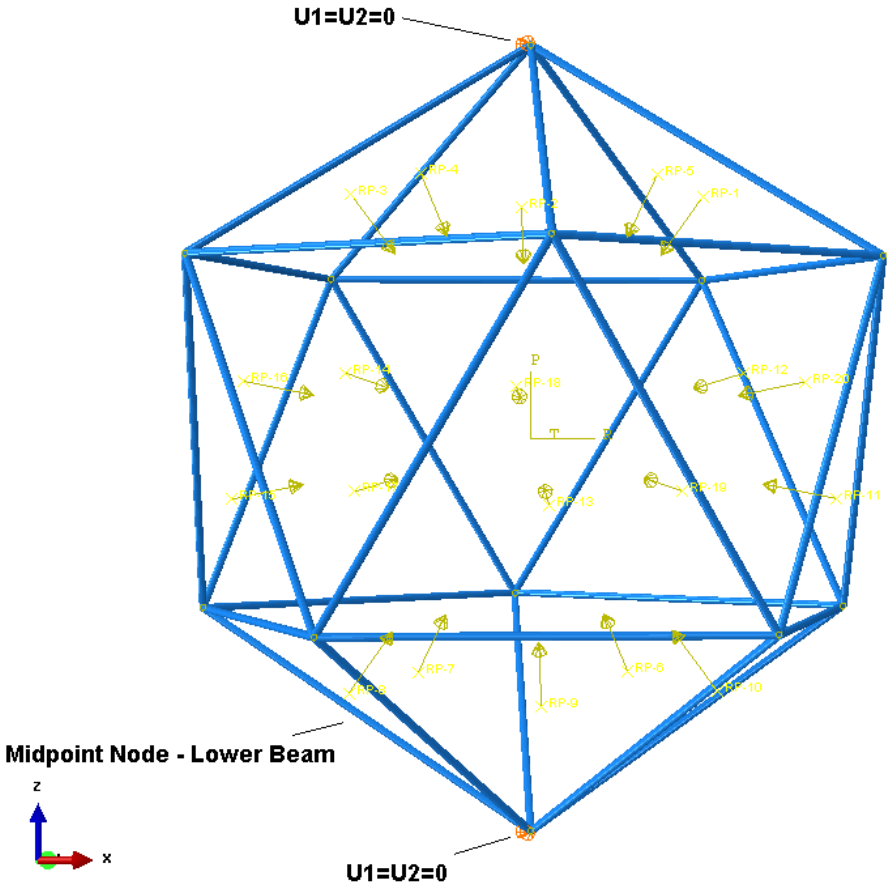

Figure 37: Boundary Condition and Load Applied for Load Study

Figure 37 shows the top and bottom nodes are restricted in the x and y direction, while all other degrees of freedom are free to move. The simple difference between BC3 and BC2 is all degrees of freedom are constrained at the bottom node in BC2 instead of only the x and y directions. BC1 has all degrees of freedom restricted at the bottom node, but none restricted at the top. BC3 was found to respond to the statically applied pressure in a symmetric behavior, while the other two boundary conditions produced nonsymmetrical behavior that led to a sudden change in slope of the applied pressure

versus displacement plots shown in Figure 36. The load which an instantaneous change in displacement direction occurs is referred to as the *snapping* load. When the load was applied dynamically, BC3 did not continue to respond in a symmetric fashion, but instead began spinning about the z-axis when the baseline icosahedron model was used. To achieve dynamic symmetry, the load at the reference point was changed to a follower force to replicate a pressure being applied, and eliminate the spinning motion. A follower force remains normal to the tangent plane of the surface where the load is applied on the structure. Figure 38 displays a simple example of a follower force applied to a cantilever beam. By definition, pressure is a follower force.

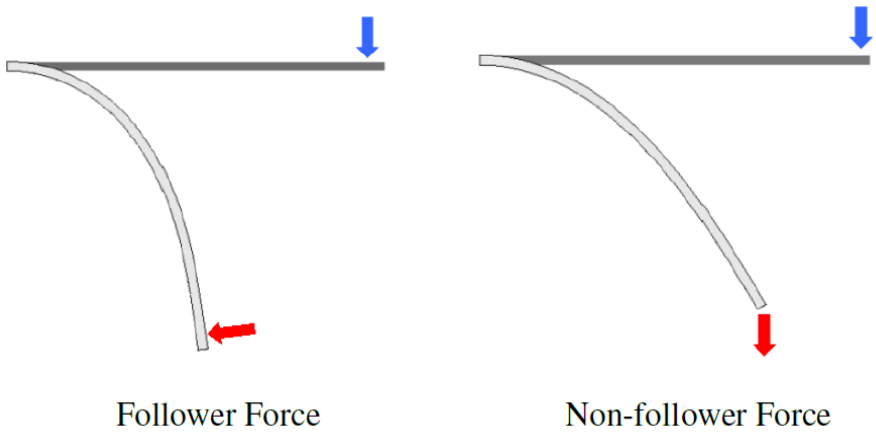

Figure 38: Follower Force (Left) and Non-follower Force (Right) [7]

The study of chaotic behavior in a system requires a dynamic response dependent on the initial conditions applied to that system. Previously, boundary conditions and symmetry were considered. Now, the effect of the rate of loading on the structure is considered. Various loading scenarios applied to the frame are shown in Figure 39. Each applied load is in the form of a ramp input, which can be written as $r(t) = t*u(t)$, where

u(t) is the step input function. The step input function is equal to unity for time greater than zero and zero for time less than zero [19]. The displacement response, also known as the ramp response, to the ramp input function is shown in Figure 40.

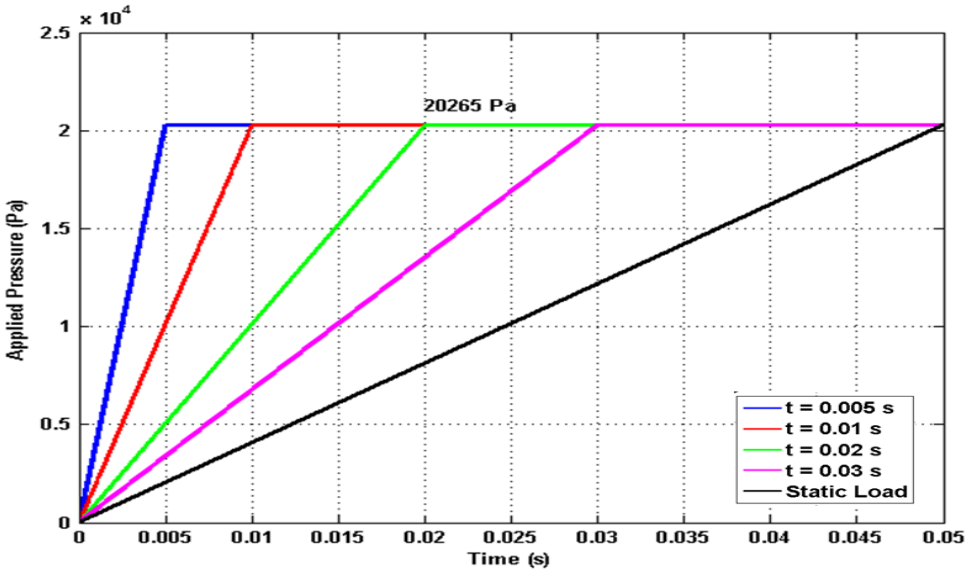

Figure 39: Various Loading Conditions for Load Study

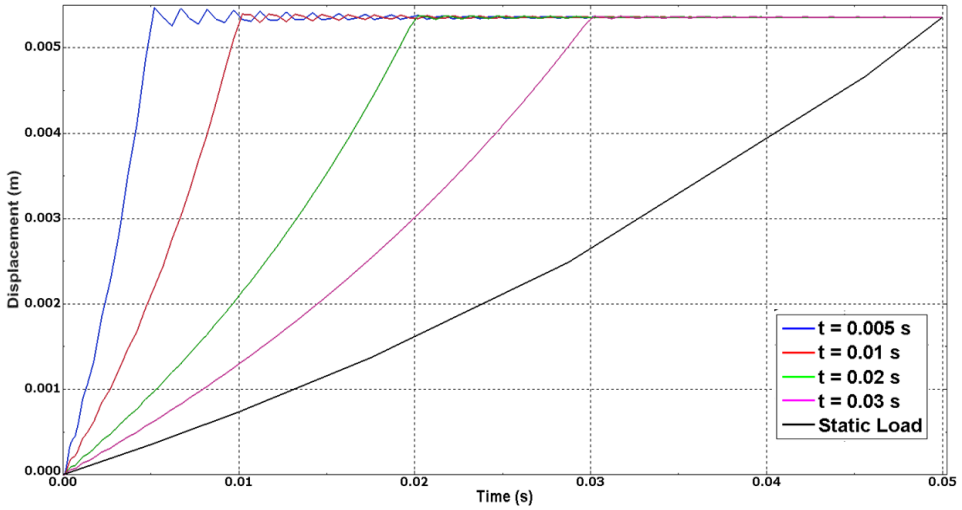

Figure 40: Displacement versus Time Curves for Various Loading Conditions

As the rate of loading is increased, the difference between the static response and the dynamic response is shown with more oscillations occurring once the full load is applied. A rise time of 0.005 seconds, corresponding to a load rate of 4.053 $MPa\text{-}s^{-1}$, sufficiently displayed the dynamic characteristics of interest in this research. A rate of at least that value is used for the remainder of this thesis in studying chaotic behavior.

Chaotic behavior is dependent on the initial conditions applied to a system, and the rates which loads are applied effectively change the initial velocity of the icosahedron frame, which changes the initial conditions. The initial slopes of the displacement curves in Figure 40 are the initial velocities, and increasing the initial velocity increases the oscillations that occur once the full load is applied. This makes sense as the increase in velocity is directly correlated to an increase in kinetic energy in the system. When the amount of energy applied to the system is too great for the structure to absorb, a *snapback* behavior occurs. However, if too little energy is applied to the system (too small of initial velocity), the response appears to be the same as the static response and chaos cannot be examined. The time step used in evaluating the varying loading scenarios was set to automatic, rather than fixed, for reasons stated in the previous time step study discussed in Chapter III. Applying the automatic time step in Abaqus allows the program to select an appropriate time step for that iteration, and it allows the program to change the time step over the course of solving the problem. The reason for this is a detailed response was not desired, only a definite point where the response changes from exhibiting static characteristics to dynamic characteristics, enabling a chaotic motion analysis.

The *snapback* behavior presented by Adorno-Rodriguez occurred in the first two boundary conditions that were deemed unsymmetrical. However, the *snapping* behavior developed for all boundary conditions, including BC3, when the load was applied dynamically. Additionally, the load that caused the *snapback* behavior to occur decreased when the load was applied dynamically instead of statically, and the value to which it decreased was dependent on the initial conditions (load rate). The ramp input load scenarios applied to the frame above the *snapping* load are shown in Figure 41, and the displacement versus time ramp response to those loads is shown in Figure 42.

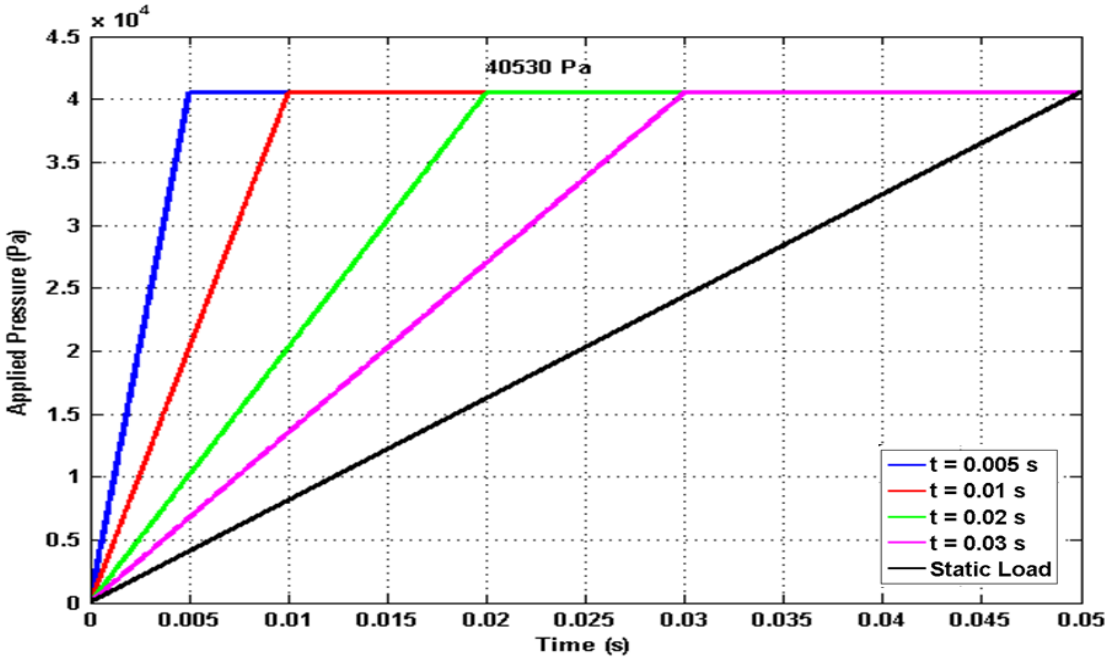

Figure 41: Loads above *Snapping* Load

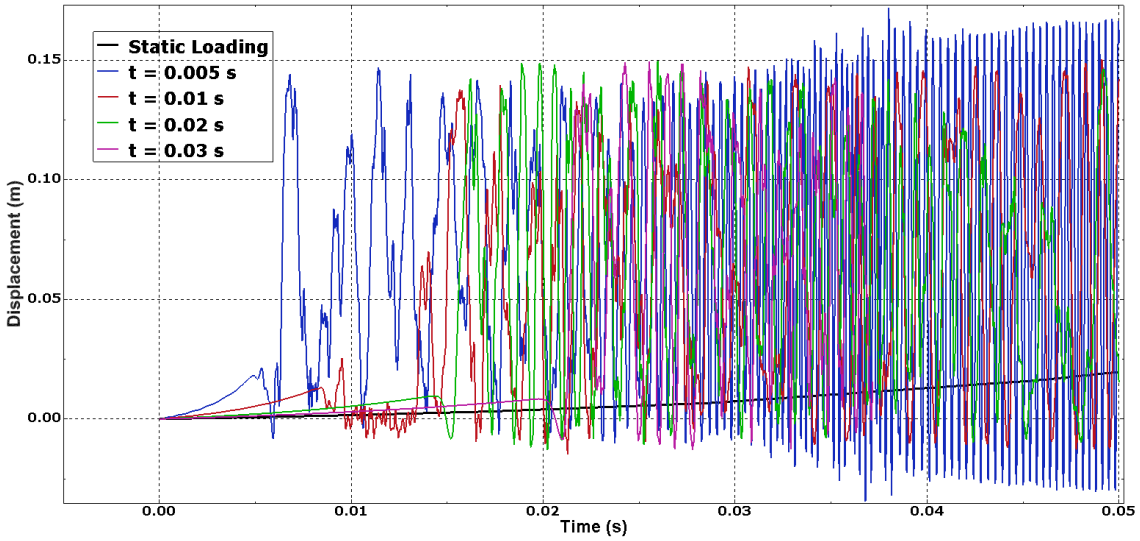

Figure 42: Displacement versus Time Curves above *Snapping* Load

The results of the load rate analysis shows the importance of what load is applied, and at what rate it is applied. These initial conditions drive the dynamics of the system, and for certain scenarios, lead to chaotic behavior. Clearly, Figure 40 shows the difference between a slowly applied load and a quickly applied load. The structure exhibits greater oscillatory behavior as the time over which the load is applied decreases. Also, Figure 42 displays what happens to the structure when the applied load is too large, regardless of the time over which the load is applied. These results are utilized in studying the chaotic behavior associated with the frame when an unsymmetrical boundary condition is applied, or the applied load is too great. Table 12 displays the various loading scenarios considered, and the boundary conditions of the frame to which they were applied. The last two load scenarios incorporated the skin with the frame to observe the effect it has on the instability characteristics of the model.

Table 12: Loading Rates for Applied Pressure

Load #	% of Sea Level Pressure Applied	Ramp Duration (s)	Load Rate (MPa-s^{-1})	Boundary Condition
1	10	0.002	5.0663	BC3 (Frame)
2	20	0.005	4.053	BC3 (Frame)
3	40*	0.005	8.106	BC3 (Frame)
4	10	0.002	5.0663	BC2 (Frame)
5	20	0.005	4.053	BC2 (Frame)
6	40*	0.005	8.106	BC2 (Frame)
7	40	0.005	8.106	BC3 (Frame-skin)
8	60	0.005	12.159	BC3 (Frame-skin)

**Above dynamic snapping load for frame determined for the applied load rate*

Icosahedron Frame Boundary Condition Three

In a static analysis, BC3 did not display the *snapback* behavior present in both BC1 and BC2. This section investigates the effect of dynamic loading on the structure using the same boundary condition. From Table 12, three dynamic loads are considered in determining if chaotic motion is present in the design. The first two loads are below the *snapping* load, while the third load is above.

For each load number, four plots were generated to determine if chaotic behavior exists. The first plot is the displacement versus time response for the given load. The second plot is the phase plane trajectory, displaying velocity versus displacement. The third plot is the power spectral density plot for the given load, and the fourth plot shows the convergence of the Lyapunov exponent calculated by Equation (20). Lyapunov exponent convergence plots were developed using MATLAB code provided by Wolf, et al., and the methods described in *Determining Lyapunov Exponents from a Time Series* article [25]. The MATLAB code is in the Appendix for reference.

The method developed by Wolf, et al. creates a delay reconstruction of the *attractor* described in Chapter II. It then cycles through the delay reconstructed data and calculates an estimate for the Lyapunov exponent at each evolution of the data. Delay reconstructions of the *attractor* were made using the delay parameter τ, which was varied in order to avoid producing a crossing or folding of the trajectories within the *attractor*. Crossing or folding of trajectories can lead to a false positive Lyapunov exponent. The algorithm cycles through the trajectory based on a number of input parameter values to calculate the Lyapunov exponent, as explained by Wolf, et al. [25].

Figure 43 through Figure 55 show the result of load numbers 1 through 3 as they were applied to the icosahedron frame with BC3. The results for load number 1 are displayed in Figure 43 through Figure 46. The applied load is well below the static and dynamic *snapping* load. As the plots show, the load does not cause a *snapback* behavior, and reaches a steady state oscillation which is purely periodic. There is no damping applied to the model, so the phase plane trajectory remains on a single orbit, rather than decreasing in size over time. The PSD plot shows the frequency response, and shows a dominant natural frequency at 1500 Hertz. This value is different than the Abaqus calculated value shown in Table 2 which lists the first natural frequency occurring around 1022 Hertz. However, this difference can be attributed to the addition of the load on the structure, and the change in boundary conditions. Finally, the convergence of the Lyapunov exponent to a negative number in Figure 46 indicates the response of the icosahedron frame for load number 1 is non-chaotic.

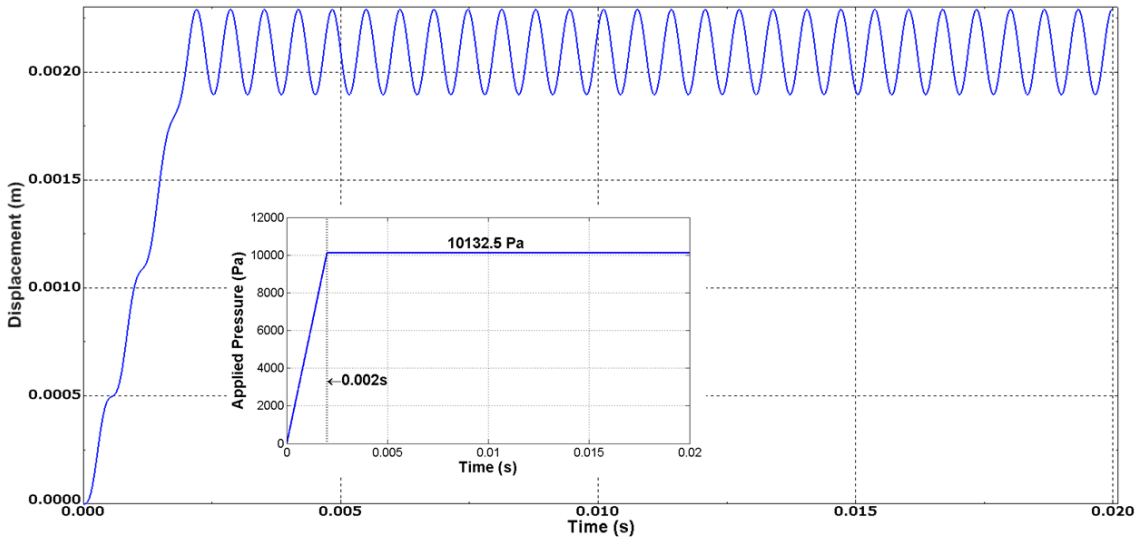

Figure 43: Load 1, BC3, $\boldsymbol{\lambda_1}$= -0.0121 bits/orbit, Displacement Curve

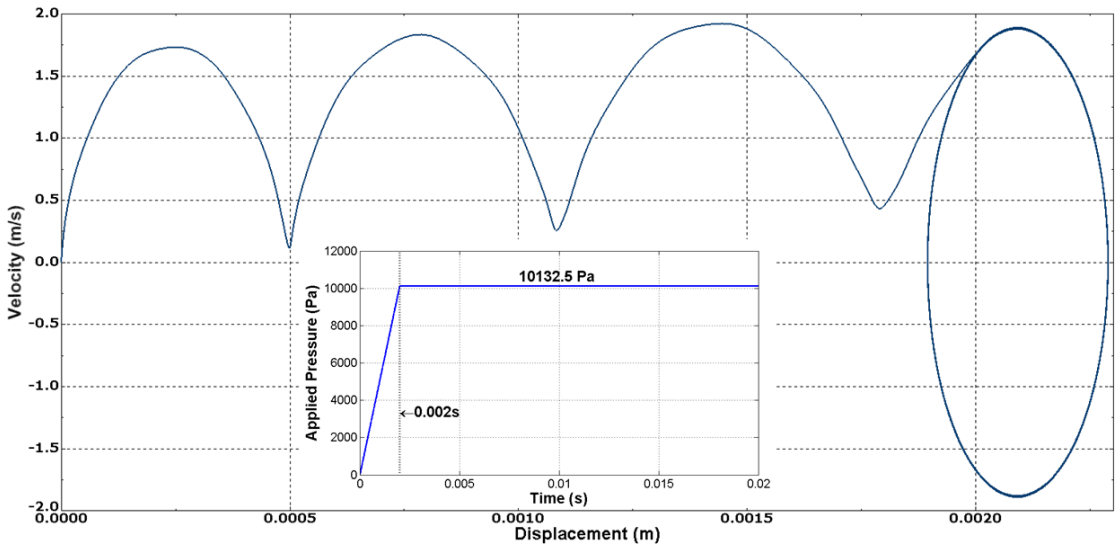

Figure 44: Load 1, BC3, $\boldsymbol{\lambda_1}$= -0.0121 bits/orbit, Phase Plane Trajectory

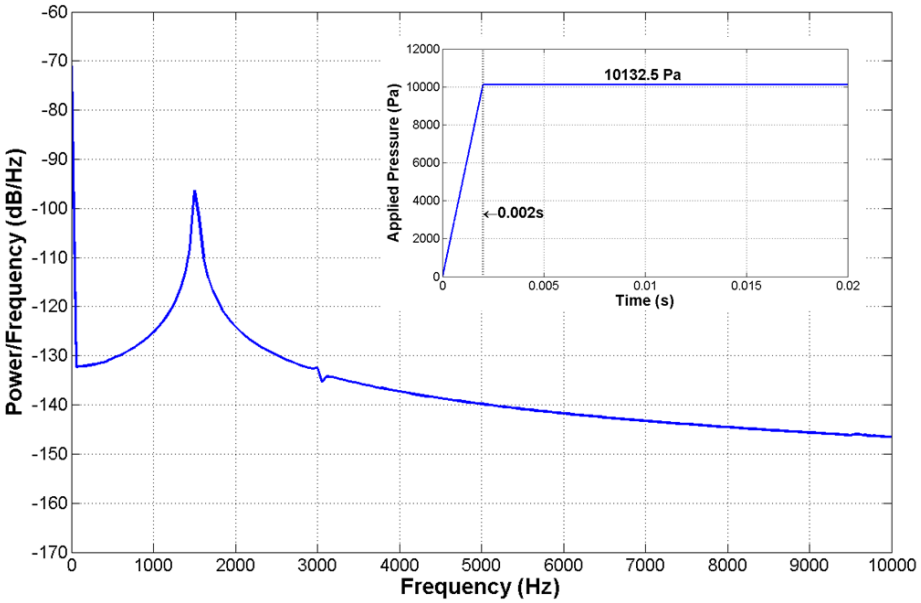

Figure 45: Load 1, BC3, $\boldsymbol{\lambda_1}$= -0.0121 bits/orbit, PSD

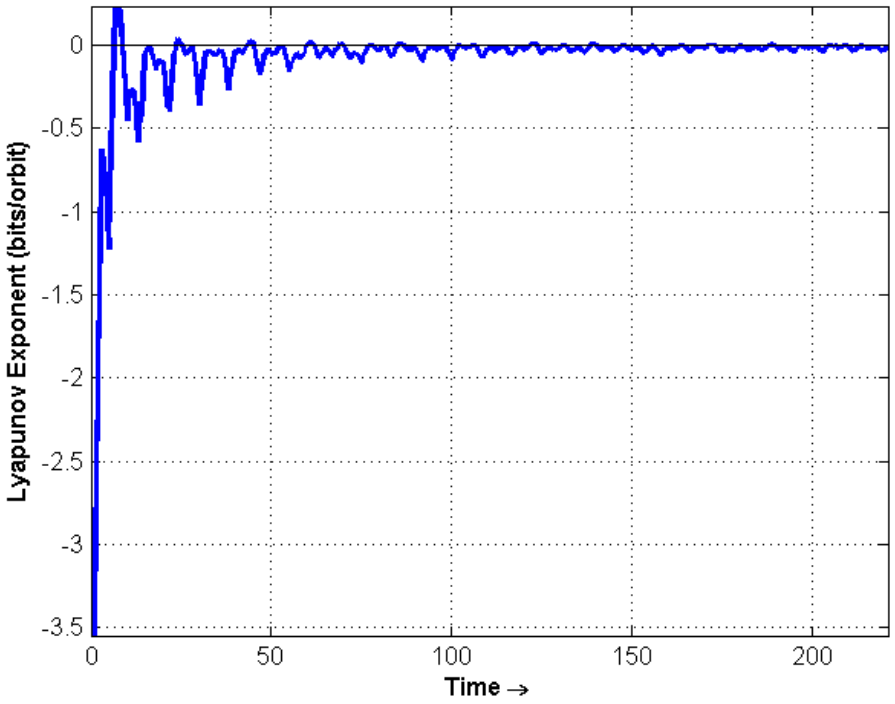

Figure 46: Load 1, BC3, $\boldsymbol{\lambda_1}$= -0.0121 bits/orbit, Lyapunov Exponent Convergence Plot

For load number 1, the Lyapunov exponent was calculated using 4500 data points spaced at 1e-5 second intervals. The initial 0.002 seconds of data corresponding to the ramped load is omitted from the calculation, as the transient response data is not desired. The following parameters were used in the MATLAB algorithm (see Wolf, et al.): *tau = 8, evolve = 8, dismin = 1e-8* and *dismax = 2e-4.* Figure 47 shows an example of the reconstructed *attractor* for load number 1. As expected, for a purely periodic response, the attractor is simply a closed curve. The attractor is reconstructed in three dimensions because the system is three-dimensional, and the plot is made of ordered triples comprised of the displacement data separated by the delay parameter, τ. For example, one point has coordinates of [$u1(t), u1(t+\tau), u1(t+2\tau)$]. The *dismax* parameter was selected based on the longest distance between points in the reconstructed *attractor* plot, and *dismin* was set to be smaller than the shortest distance between points. The *tau* and *evolve* parameters are chosen heuristically so the *attractor* does not appear to fold on itself which can lead to a false positive Lyapunov exponent calculation.

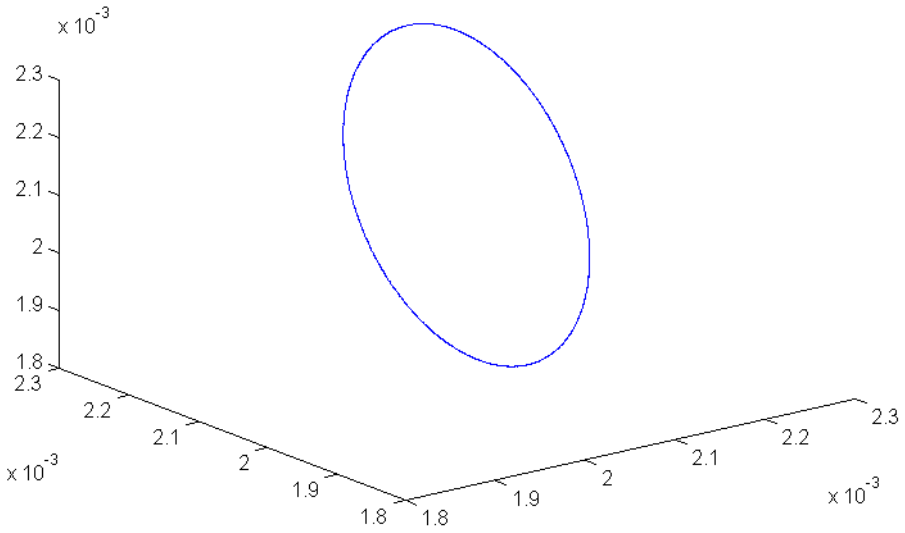

Figure 47: Delay Reconstructed *Attractor* for Load 1, BC3, $\boldsymbol{\lambda_1}$= -0.0121 bits/orbit

Load number 2 leads to the same conclusion as load number 1. The displacement curve, phase plane trajectory, PSD plot, and Lyapunov convergence are nearly identical to those of load number 1. Again, there is a periodic steady state oscillation present after the load is applied resulting in a fixed orbit shown in the phase plane trajectory. The PSD is smooth and has a clearly identifiable natural frequency, while the Lyapunov exponent converges to a negative value. The input parameters for the Lyapunov exponent calculations were the same as those used in load number 1. All of the information presented indicates non-chaotic behavior.

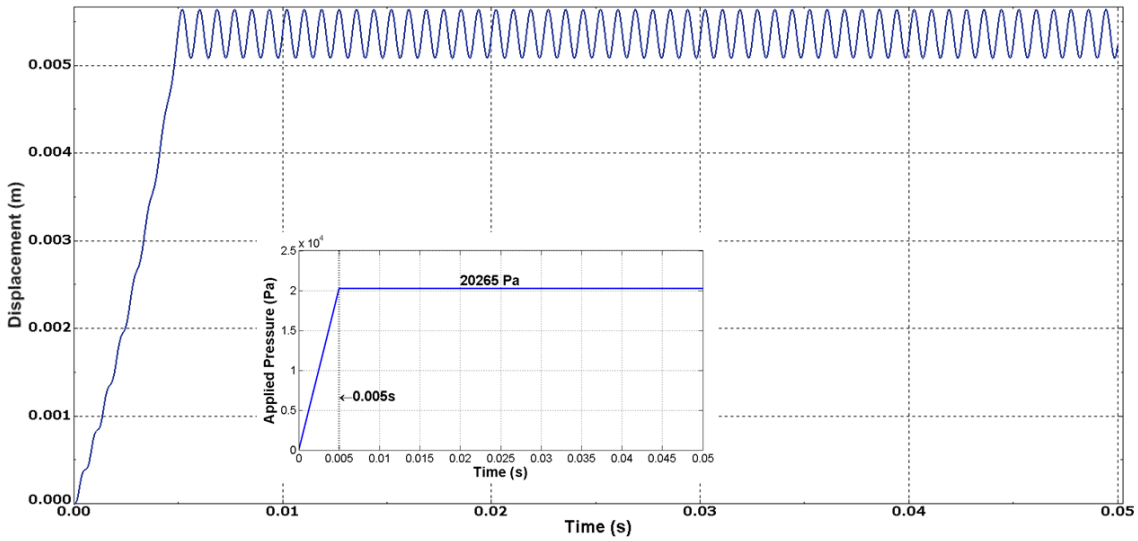

Figure 48: Load 2, BC3, $\boldsymbol{\lambda_1}$= -0.0137 bits/orbit, Displacement Curve

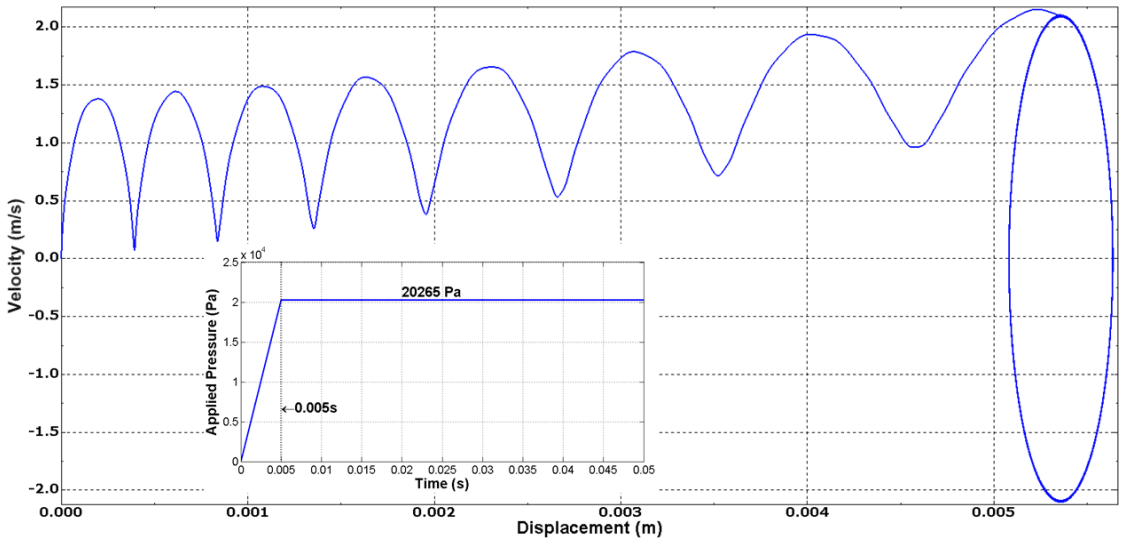

Figure 49: Load 2, BC3, $\boldsymbol{\lambda_1}$= -0.0137 bits/orbit, Phase Plane Trajectory

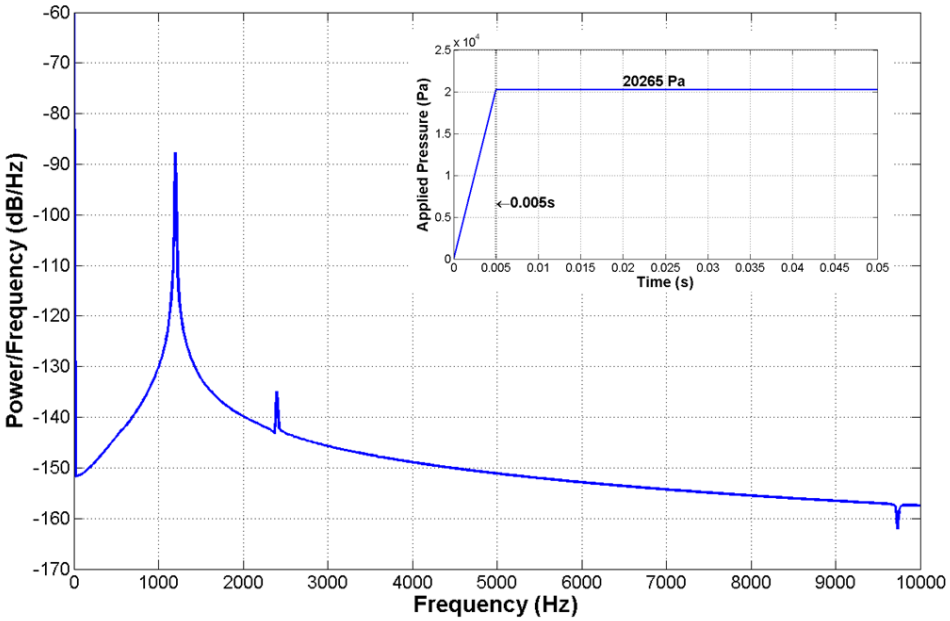

Figure 50: Load 2, BC3, $\boldsymbol{\lambda_1}$= -0.0137 bits/orbit, PSD

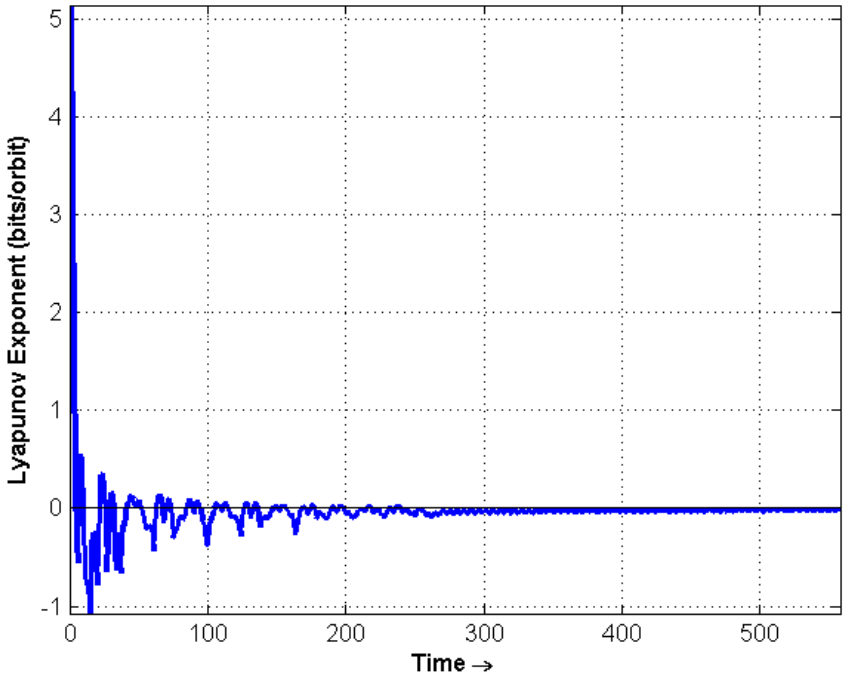

Figure 51: Load 2, BC3, $\boldsymbol{\lambda_1}$= -0.0137 bits/orbit, Lyapunov Exponent Convergence Plot

Load number 3 is applied above the *snapping* load pressure, and presents extremely different results, both quantitatively and qualitatively. The displacement curve is no longer purely periodic, but instead seems to vibrate disorderly, and it has amplitude approximately 100 times that of load number 2. The *snapback* behavior can be seen as the displacement instantaneously changing direction. Furthermore, the phase plane trajectory has no apparent repeated pattern, but does generally remain within an elliptical envelope. The orbits of the trajectory appear to fill up a portion of the phase space, indicating chaotic behavior as stated in Chapter II. The frequency response has changed character from load number 1 and 2, becoming noisy, and not clearly showing a peak frequency. Finally, the convergence of the Lyapunov exponent is well above zero bits/orbit, indicating significantly chaotic behavior occurring above the dynamically applied *snapping* load. The bits/orbit unit is carried over from Wolf's information theory terms, where bits references amount of information. Specifically, "the exponents measure the rate at which system processes create or destroy information… Hence if an initial point were specified with an accuracy of one part per million (20 bits), the future behavior could not be predicted after about" 0.0018 seconds, corresponding to less than one quarter of a single orbit. "After this time the small uncertainty will essentially cover the entire *attractor,* reflecting 20 bits of new information that can be gained from an additional measurement of the system" [25]. In short, load number 3 displays chaotic behavior such that after only a quarter of a single orbit predictability is lost.

Values of the input parameters to the algorithm for load number 3 were *tau = 80, evolve = 80, dismin = 1e-8* and *dismax = 2e-2.* The change is largely attributed to the change in amplitude in the displacement curve, as well the decrease in time step used in

obtaining the solution. As discussed in Chapter III, the time step had to be decreased to 1e-6 seconds for Abaqus to converge on a solution to the problem, instead of the value of 1e-5 seconds used in the simpler problems using load number 1 and 2.

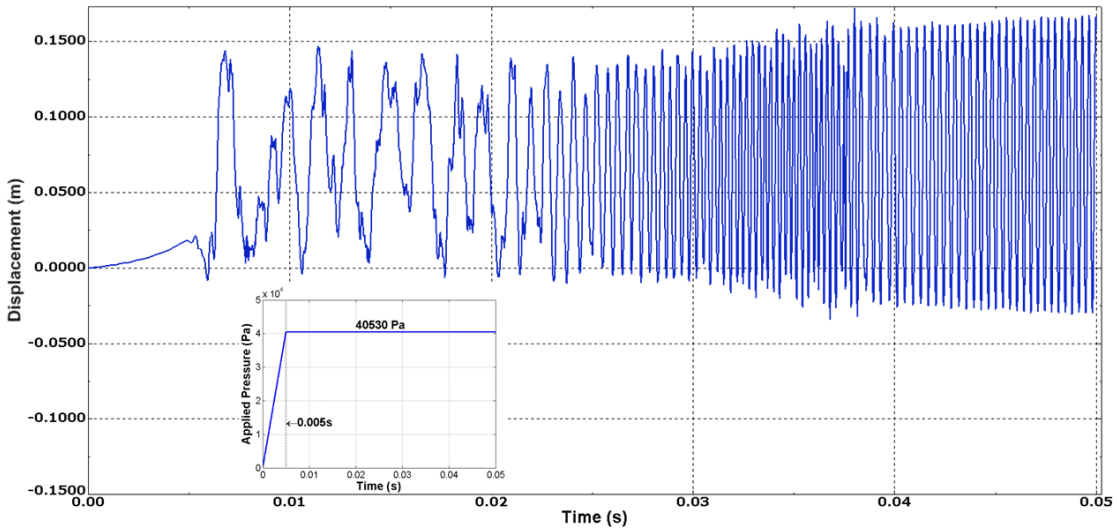

Figure 52: Load 3, BC3, $\boldsymbol{\lambda_1}$= 3.8814 bits/orbit, Displacement Curve

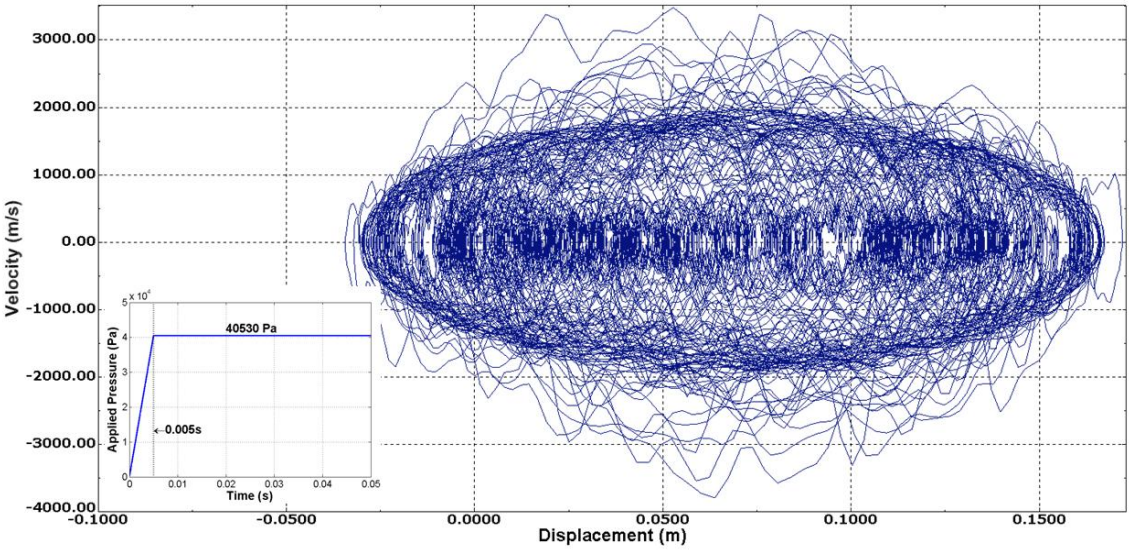

Figure 53: Load 3, BC3, $\boldsymbol{\lambda_1}$= 3.8814 bits/orbit, Phase Plane Trajectory

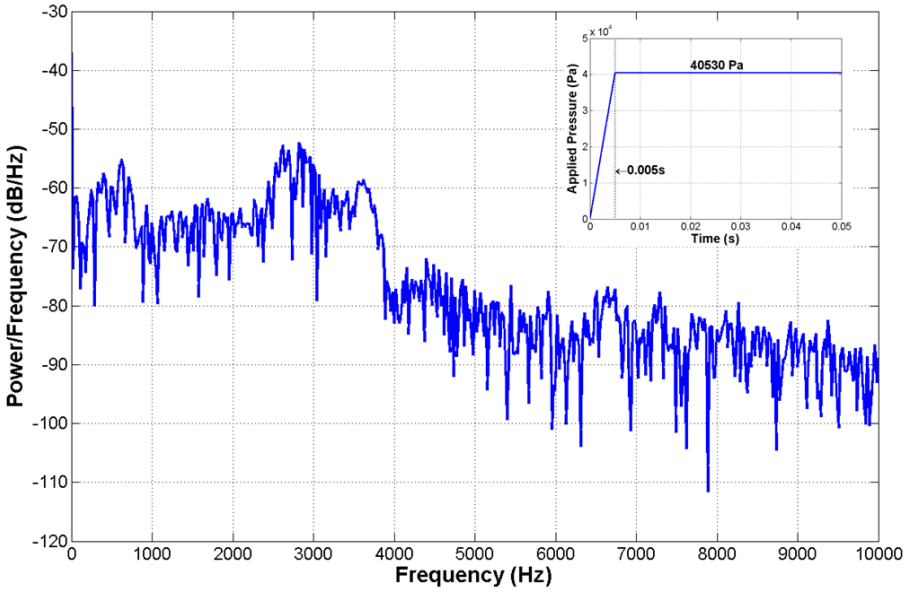

Figure 54: Load 3, BC3, $\boldsymbol{\lambda_1}$= 3.8814 bits/orbit, PSD

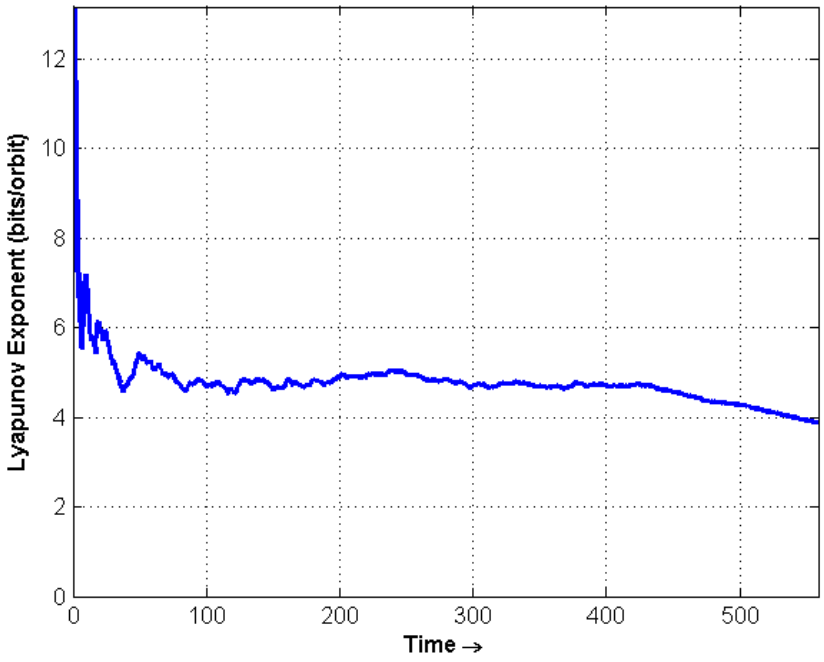

Figure 55: Load 3, BC3, $\boldsymbol{\lambda_1}$= 3.8814 bits/orbit, Lyapunov Exponent Convergence Plot

Icosahedron Frame Boundary Condition Two

The same loads applied to BC3 were applied to BC2 to confirm the *snapback* behavior originally presented in the static analysis. Figure 56 through Figure 59 show the results of load number 4, Figure 60 through Figure 63 show the results for load number 5, and Figure 64 through Figure 67 are from load number 6.

Load 4 and 5 create responses similar in each of the plots analyzed. Figure 56 and Figure 60 reveal the most periodic displacement curves with small disturbances occurring throughout the response. The displacement curve of load number 5 grows more erratic, and the number of non-periodic disturbances increases as the applied load increases. The phase plane trajectories of the two responses are also similar, settling into an elliptical orbit of varying size. These variations in the orbit size correspond to the disturbances shown in the displacement plots. As the force increases in load number 5, the disturbances become larger and more numerous, which gives rise to larger variations in the orbits of the phase plane trajectory. The PSD plot of the two loads looks similar, with peak frequencies at 1556 Hz and 1200 Hz, respectively. However, the increased pressure of load number 5 is responsible for more peaks being present than in the PSD plot of load number 4. The Lyapunov exponent convergence plot shown in Figure 59 and Figure 63 share the same characteristics, with the final convergence settling at a slightly positive number. Returning to the example given in the previous section on the interpretation of the final value for the Lyapunov exponent, predictability is lost after 65.9 orbits, and 53.95 orbits for load numbers 4 and 5, respectively (assuming 20 bits of "good" data initially). The input parameters for the Lyapunov exponent code were the same for load

number 4 and load number 5; specifically, they were *tau = 15*, *evolve = 10*, *dismin = 1e-8* and *dismax = 2e-4*.

All of the response plots from load number 4 and load number 5 indicate that BC2 presents a slightly chaotic behavior, decreasing in predictability as the load rate is increased. While the *snapback* behavior associated with the unsymmetrical boundary condition is not identified by applying load number 4 or 5, the structure seems to respond in a chaotic fashion below the dynamically applied *snapping* load. This indicates small changes in the initial conditions cause significant changes in the response of the structure under BC2.

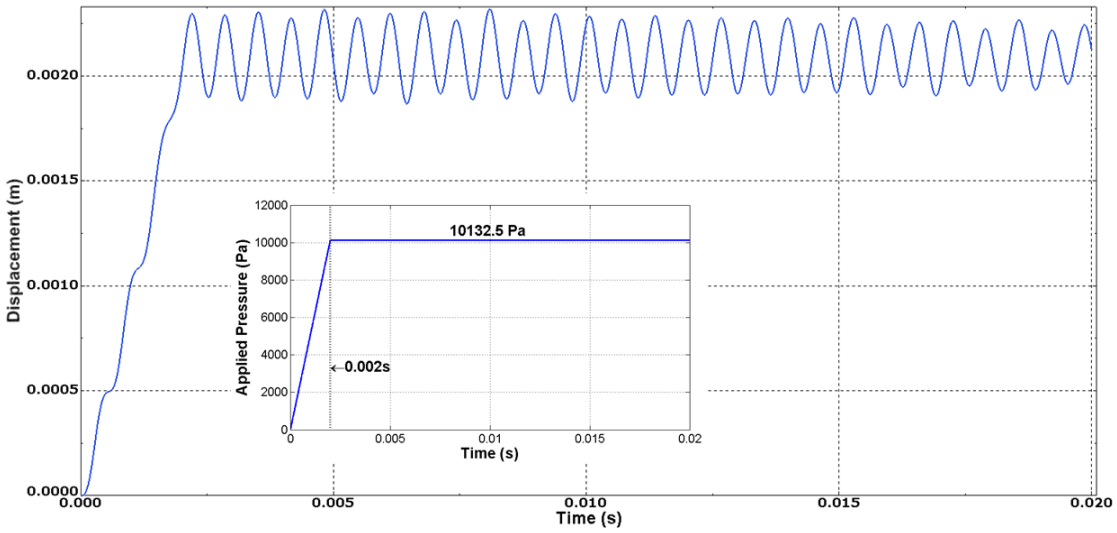

Figure 56: Load 4, BC2, $\boldsymbol{\lambda_1}$= 0.303 bits/orbit, Displacement Curve

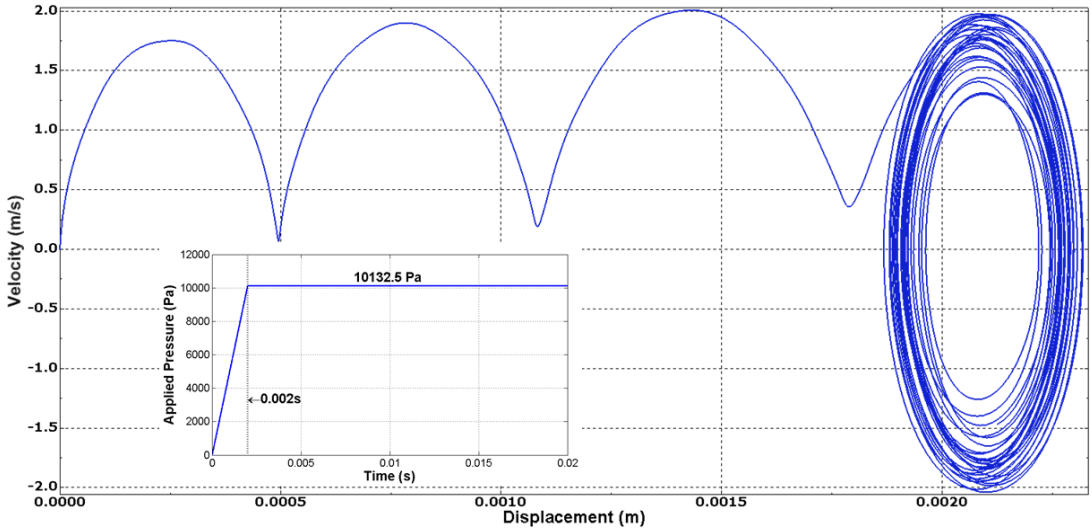

Figure 57: Load 4, BC2, $\boldsymbol{\lambda_1}$= 0.303 bits/orbit, Phase Plane Trajectory

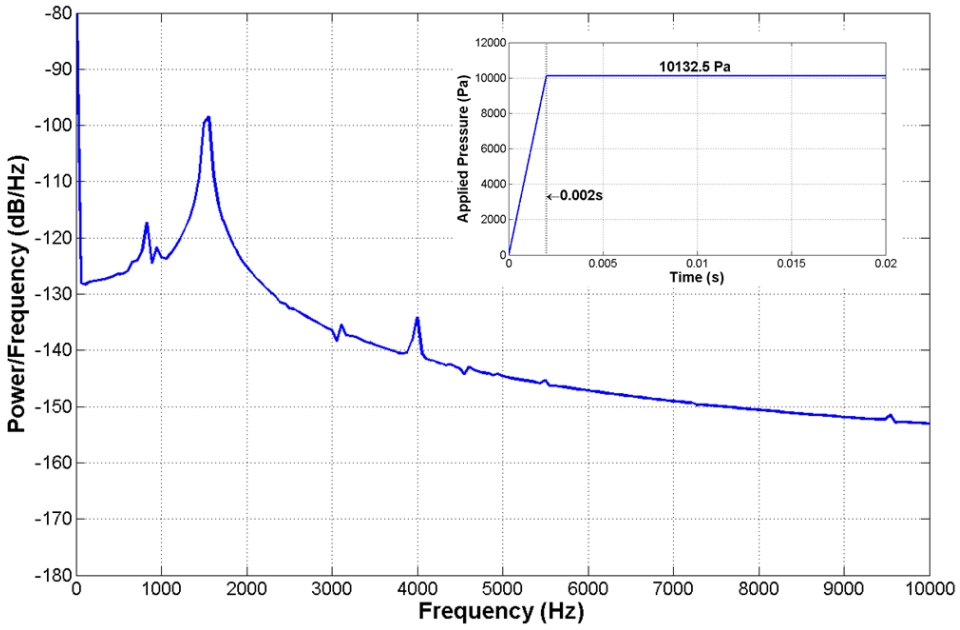

Figure 58: Load 4, BC2, $\boldsymbol{\lambda_1}$= 0.303 bits/orbit, PSD

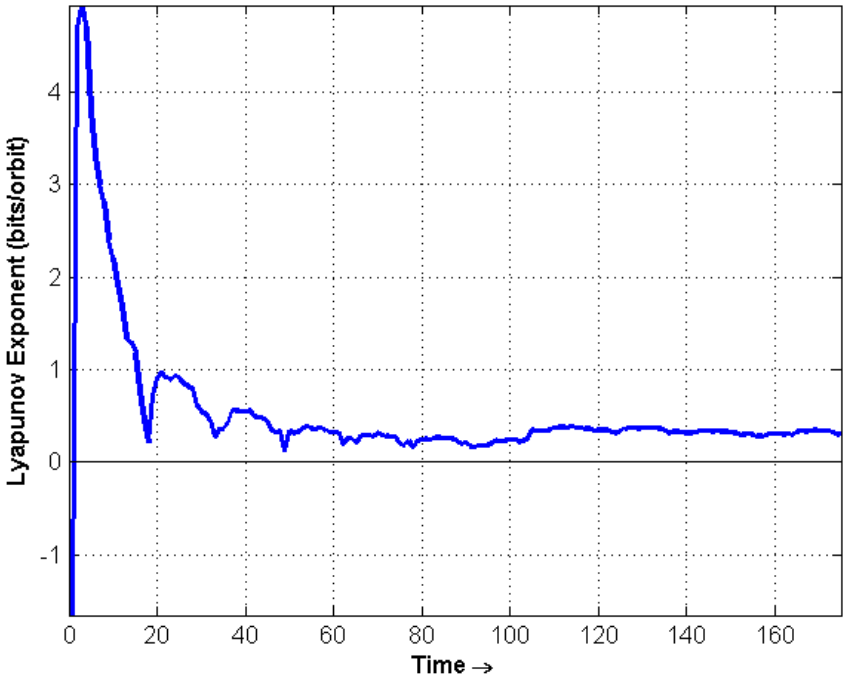

Figure 59: Load 4, BC2, $\boldsymbol{\lambda_1}$= 0.303 bits/orbit, Lyapunov Exponent Convergence Plot

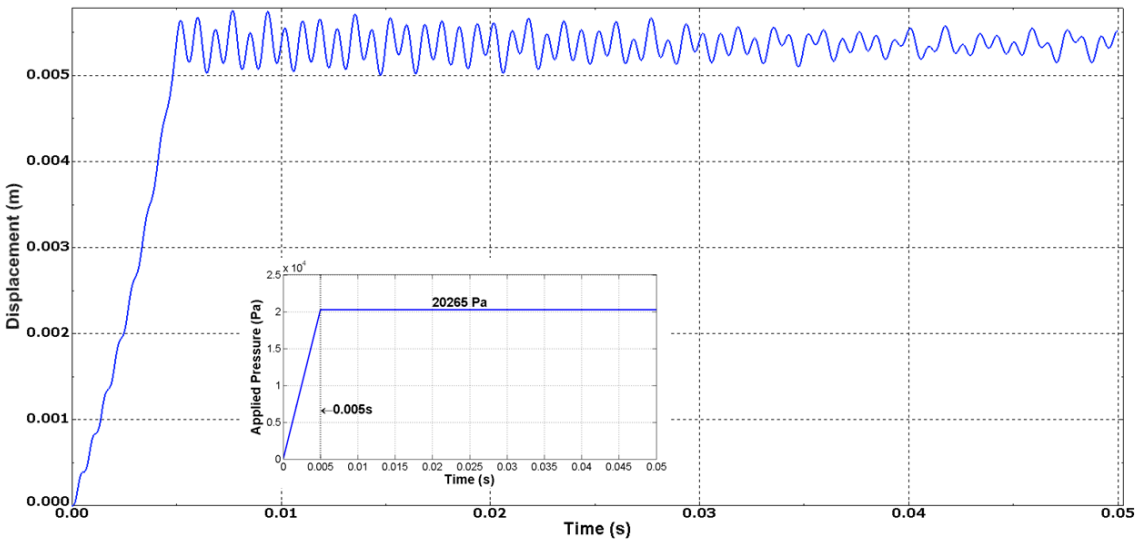

Figure 60: Load 5, BC2, $\boldsymbol{\lambda_1}$= 0.371 bits/orbit, Displacement Curve

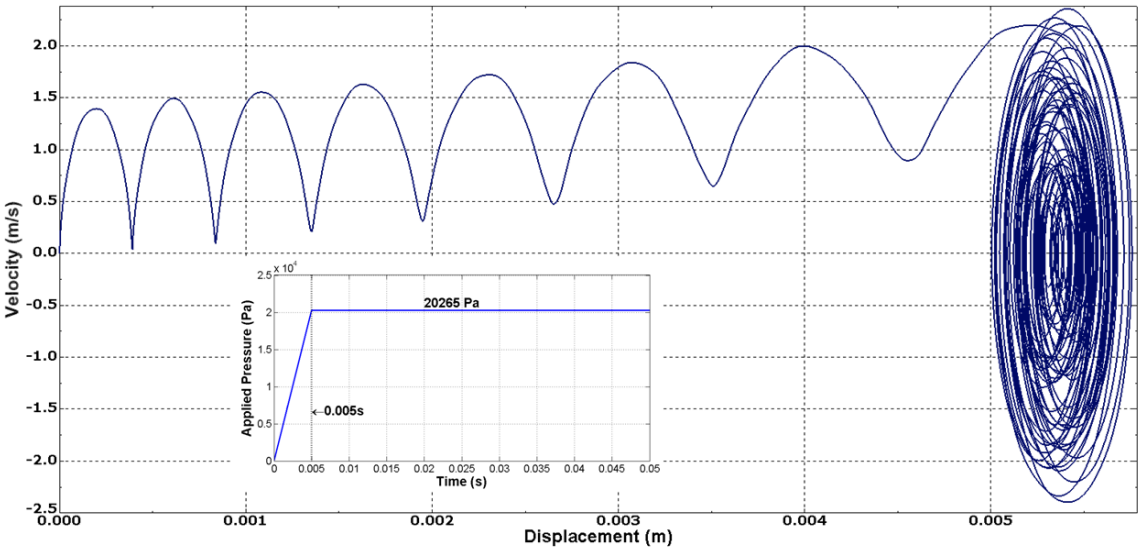

Figure 61: Load 5, BC2, $\boldsymbol{\lambda_1}$= 0.371 bits/orbit, Phase Plane Trajectory

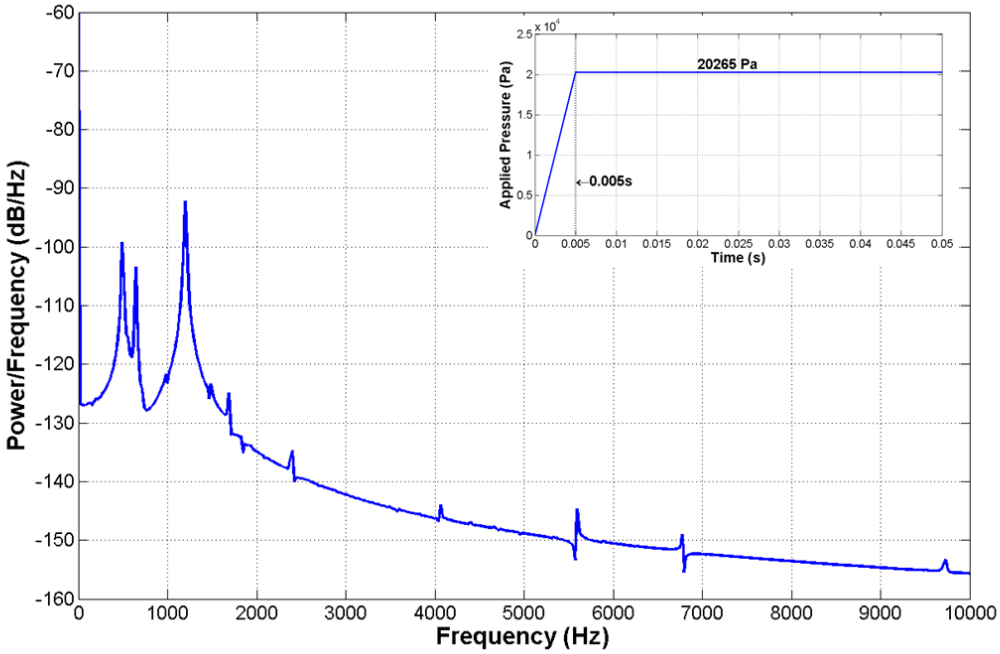

Figure 62: Load 5, BC2, $\boldsymbol{\lambda_1}$= 0.371 bits/orbit, PSD

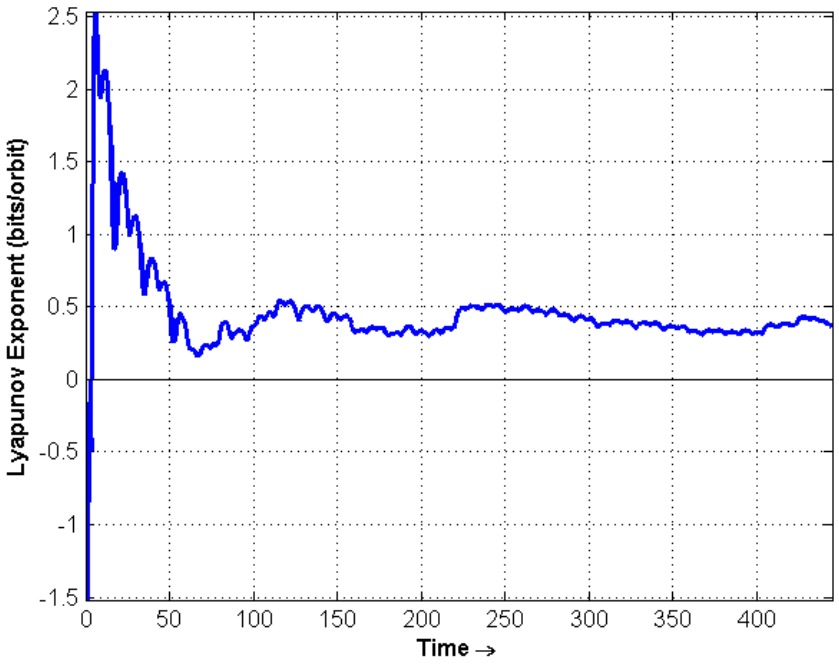

Figure 63: Load 5, BC2, $\boldsymbol{\lambda_1}$= 0.371 bits/orbit, Lyapunov Exponent Convergence Plot

Load number 6 is applied to BC2 just as load number 3 was applied to BC3. The dynamically applied load is above the pressure required to create the *snapback* behavior for the symmetrical BC3, therefore, it is expected to produce similar, if not more chaotic results for BC2. Figure 64 through Figure 67 shows the results of the loading scenario, and show the response is more chaotic than the response to load number 3 applied to BC3. Specifically, the Lyapunov exponent converges to a significantly higher value for load number 6, corresponding to lost predictability after a single orbit. The input parameters for the Lyapunov exponent code were: *tau = 150, evolve = 80, dismin = 1e-8* and *dismax = 2e-2.*

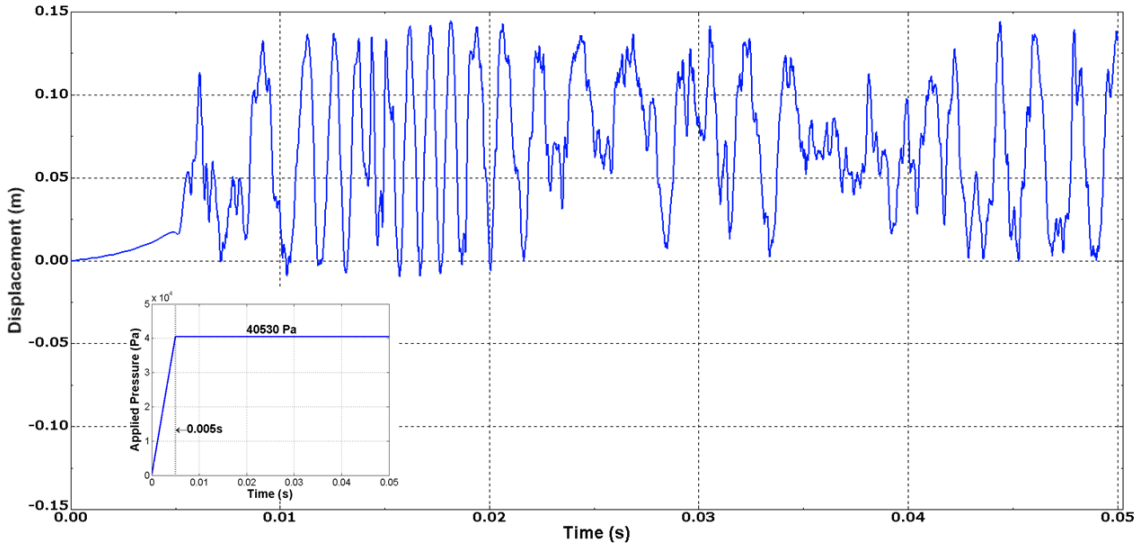

Figure 64: Load 6, BC2, $\boldsymbol{\lambda_1}$= 19.67 bits/orbit, Displacement Curve

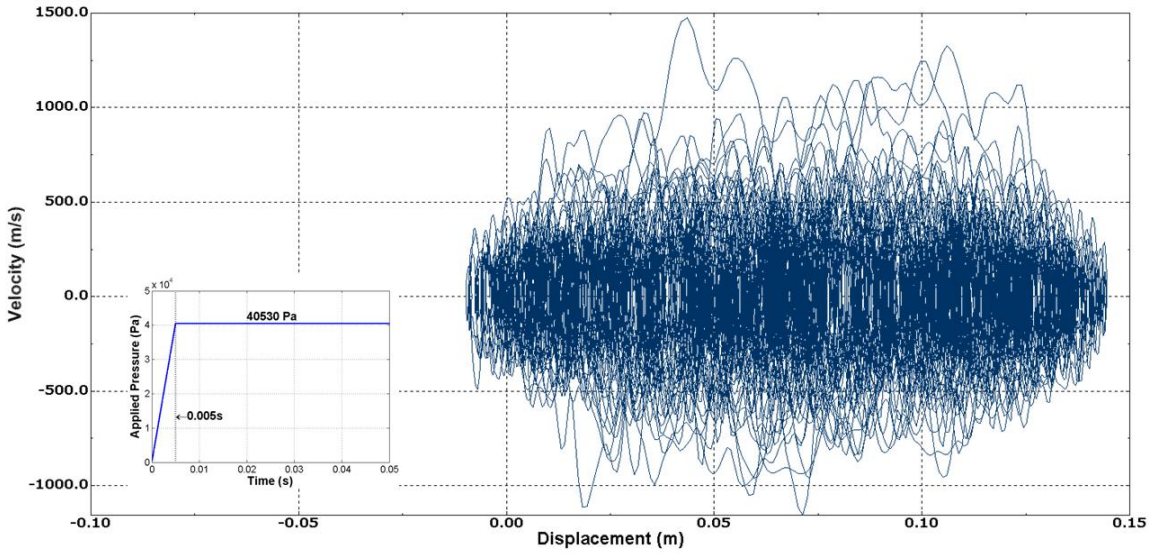

Figure 65: Load 6, BC2, $\boldsymbol{\lambda_1}$= 19.67 bits/orbit, Phase Plane Trajectory

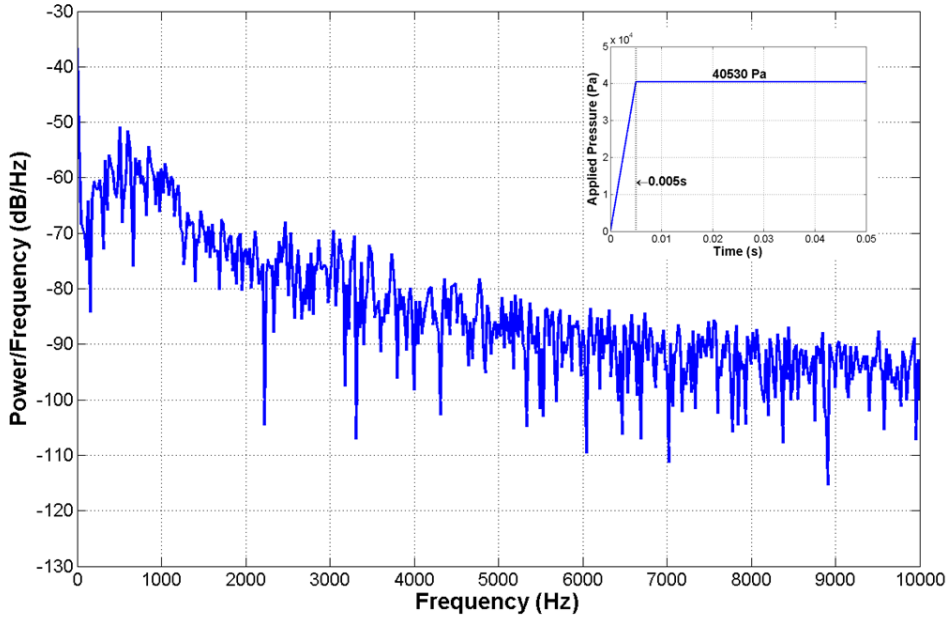

Figure 66: Load 6, BC2, $\boldsymbol{\lambda_1}$= 19.67 bits/orbit, PSD

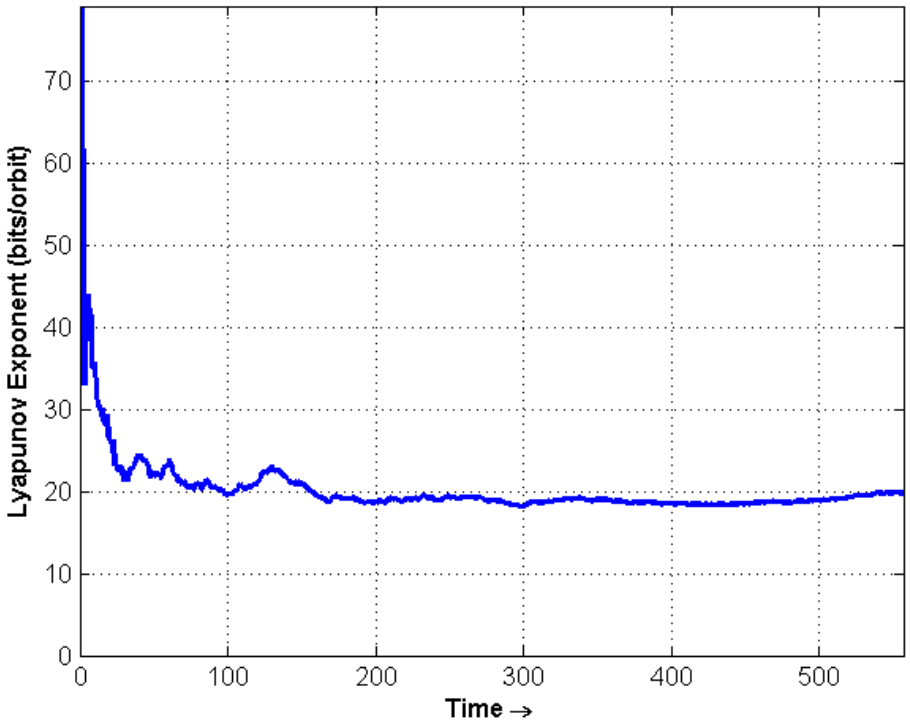

Figure 67: Load 6, BC2, $\boldsymbol{\lambda_1}$= 19.67 bits/orbit, Lyapunov Exponent Convergence Plot

Icosahedron Frame and Skin Boundary Condition Three

Previous research indicated the frame itself exhibited a *snapback* behavior. The same behavior was not predicted to occur when the skin was placed on the frame to create the full icosahedron LTAV design. However, with the knowledge a dynamic *snapping* load is observed below the static load, and the *snapback* behavior is present in the frame for the symmetric BC3 when subject to the dynamic load, the dynamic load above the *snapping* load was applied to the entire icosahedron model to determine if the *snapback* occurred.

Figure 68 through Figure 71 represent the response of the full icosahedron LTAV design to load number 7, which caused the *snapback* behavior to occur in the frame. Additionally, Figure 72 through Figure 75 show the response to load number 8, which reaches 60% SL pressure. Interestingly, both loading scenarios result in very similar responses which are somewhat different from the responses seen in the frame alone. The displacement curves shown in Figure 68 and Figure 72 show highly periodic behavior, even as the load rises to its steady state level. The phase plane trajectories of the loads also achieve a common orbit at steady state. The size of the orbit varies, but it is unlike the variations seen in load number 4 and 5, where the size and center of the orbit seem to change sporadically. Instead, the orbits change size in a predictable fashion, and the center of the elliptical orbit remains nearly constant. The decrease in orbit size implies the membrane applied to the icosahedron frame introduces system level damping, and if the solution was carried out further, the reconstructed *attractor* would likely decay to a single point. The reconstructed *attractor* for load number 7 is shown in Figure 76, and it can be seen that a torus shaped *attractor* is reconstructed.

The PSD of the two loading scenarios is fairly smooth with clearly established peaks. Finally, the Lyapunov exponent calculated is negative for both loading cases applied to the icosahedron frame and skin model. All of the indicators utilized establish the full icosahedron LTAV design behaves non-chaotically when the sudden vacuum is applied. The input parameters for the Lyapunov exponent code were the same for load number 7 and load number 8, except *tau*; specifically, they were: *tau = 15 (8 for load 8) , evolve = 8, dismin = 1e-8* and *dismax = 2e-3.*

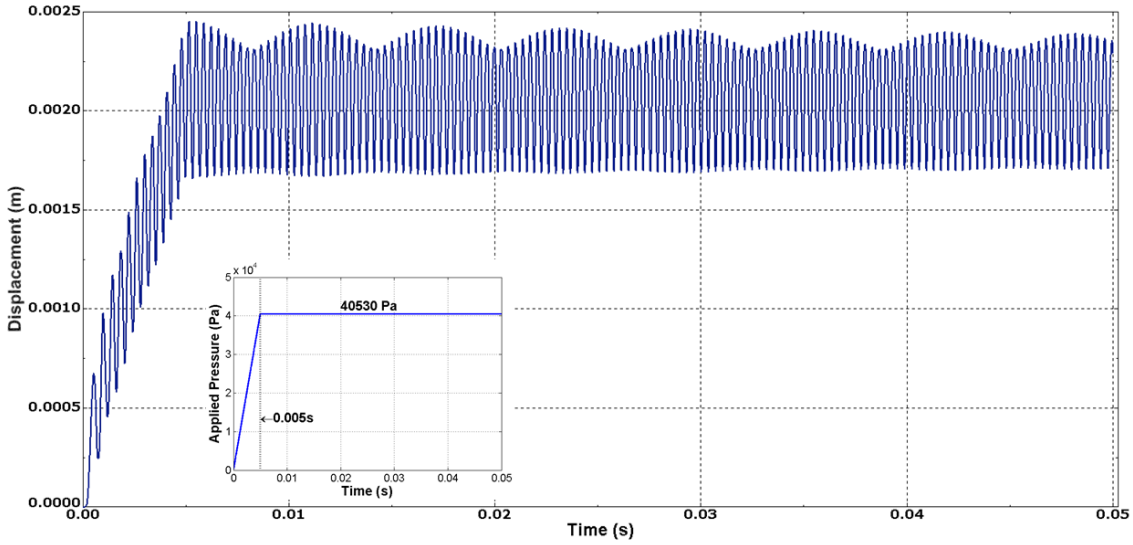

Figure 68: Load 7, BC3, $\boldsymbol{\lambda_1}$= -0.00291 bits/orbit, Displacement Curve

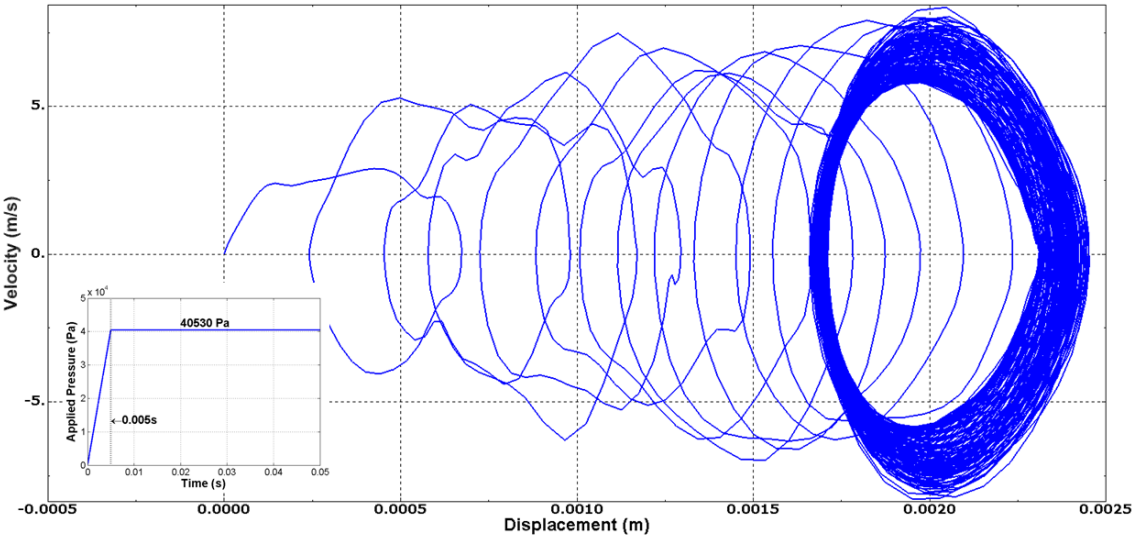

Figure 69: Load 7, BC3, $\boldsymbol{\lambda_1}$= -0.00291 bits/orbit, Phase Plane Trajectory

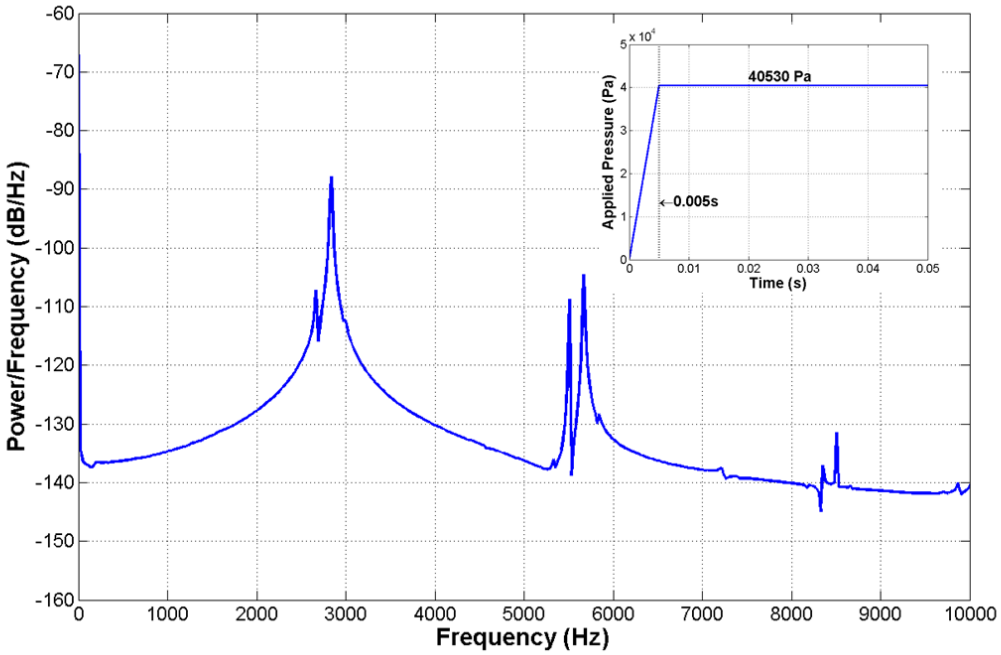

Figure 70: Load 7, BC3, $\boldsymbol{\lambda_1}$= -0.00291 bits/orbit, PSD

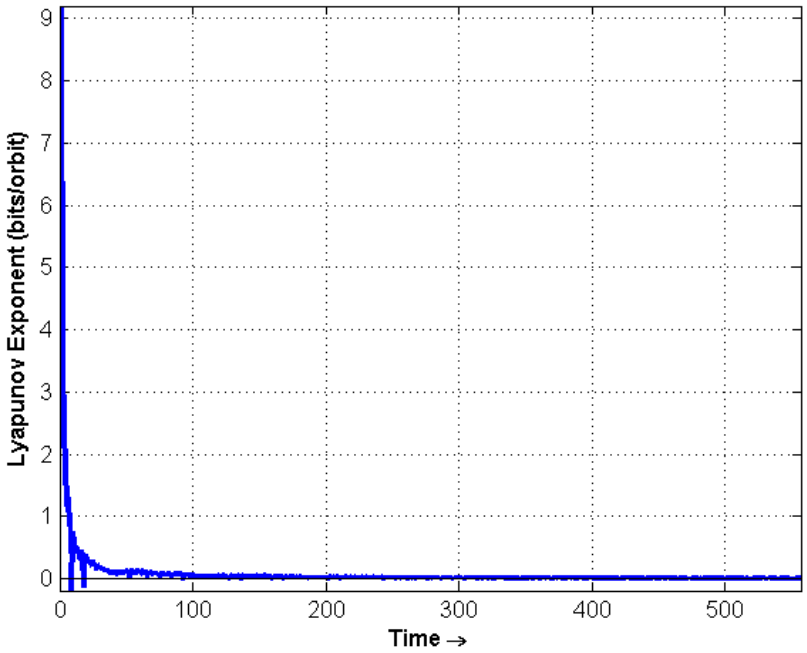

Figure 71: Load 7, BC3, λ_1= -0.00291 bits/orbit, Lyapunov Exponent Convergence Plot

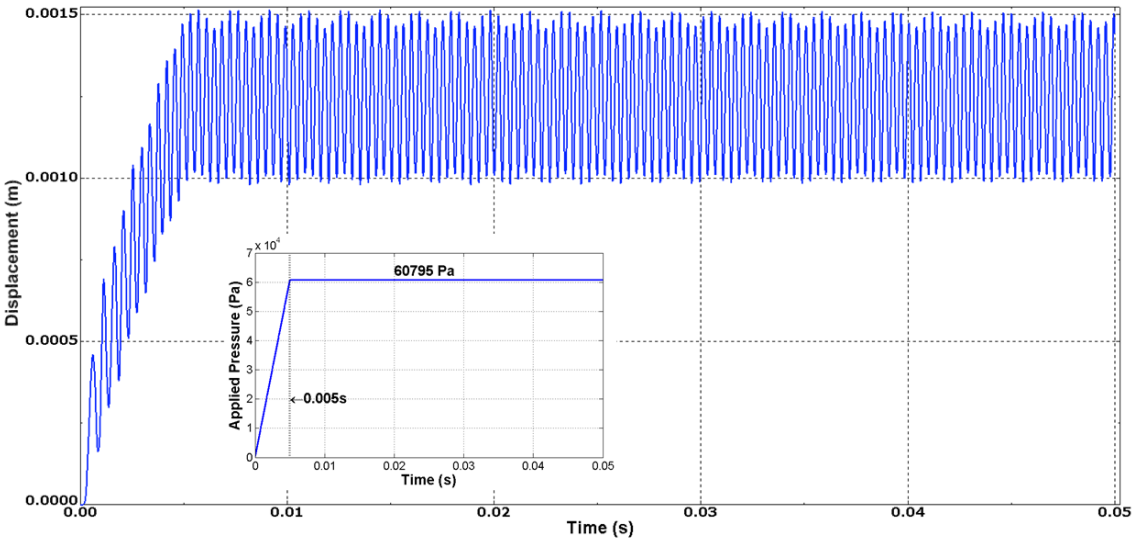

Figure 72: Load 8, BC3, λ_1= -0.0119 bits/orbit, Displacement Curve

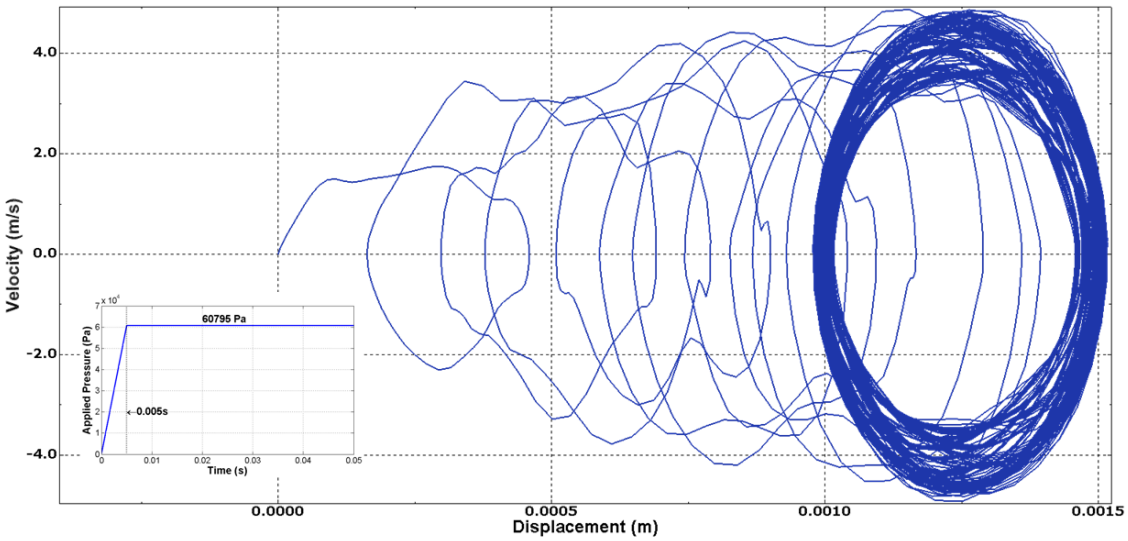

Figure 73: Load 8, BC3, λ_1= -0.0119 bits/orbit, Phase Plane Trajectory

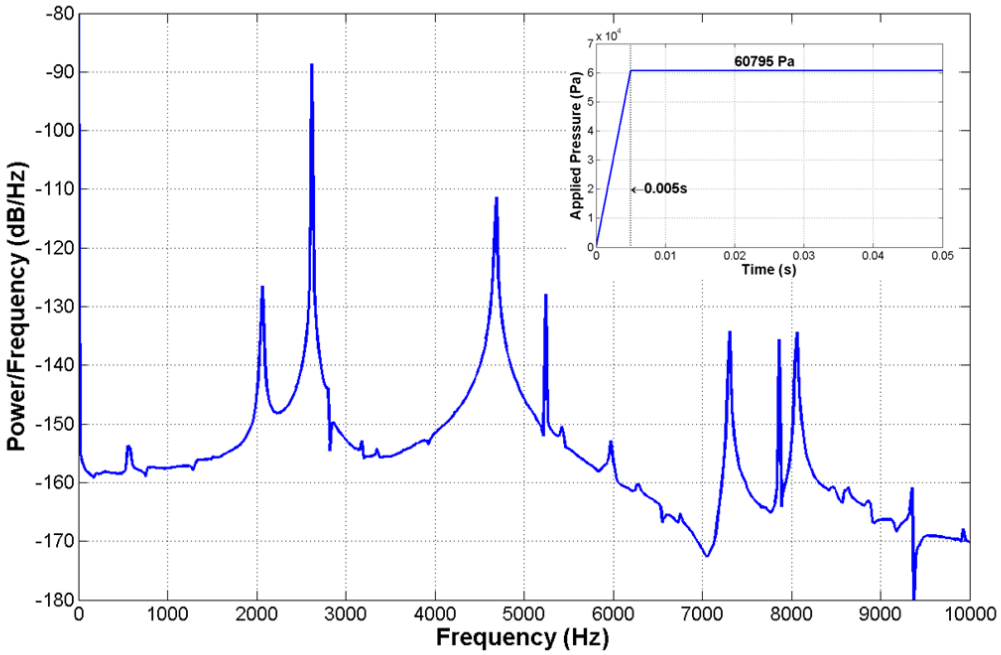

Figure 74: Load 8, BC3, λ_1= -0.0119 bits/orbit, PSD

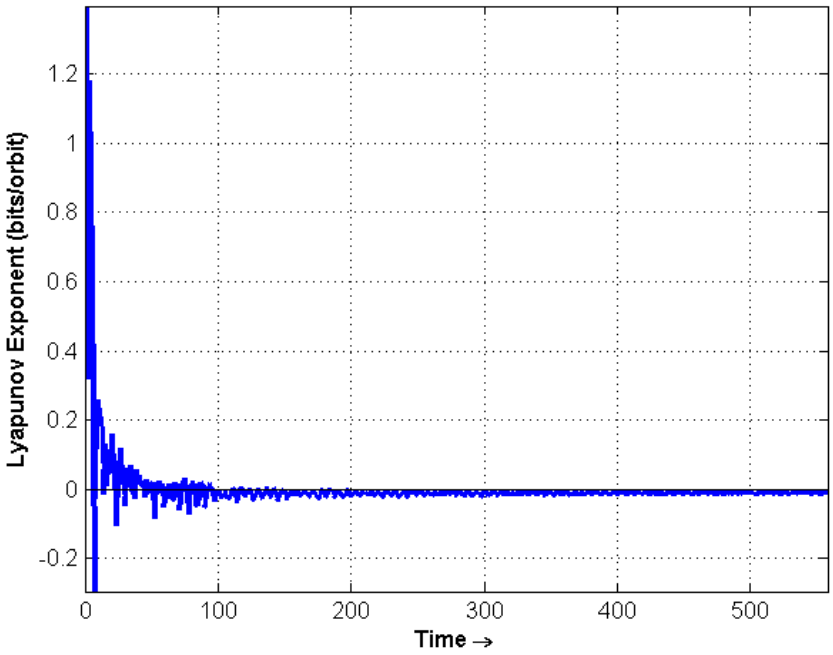

Figure 75: Load 8, BC3, $\boldsymbol{\lambda_1}$= -0.0119 bits/orbit, Lyapunov Exponent Convergence Plot

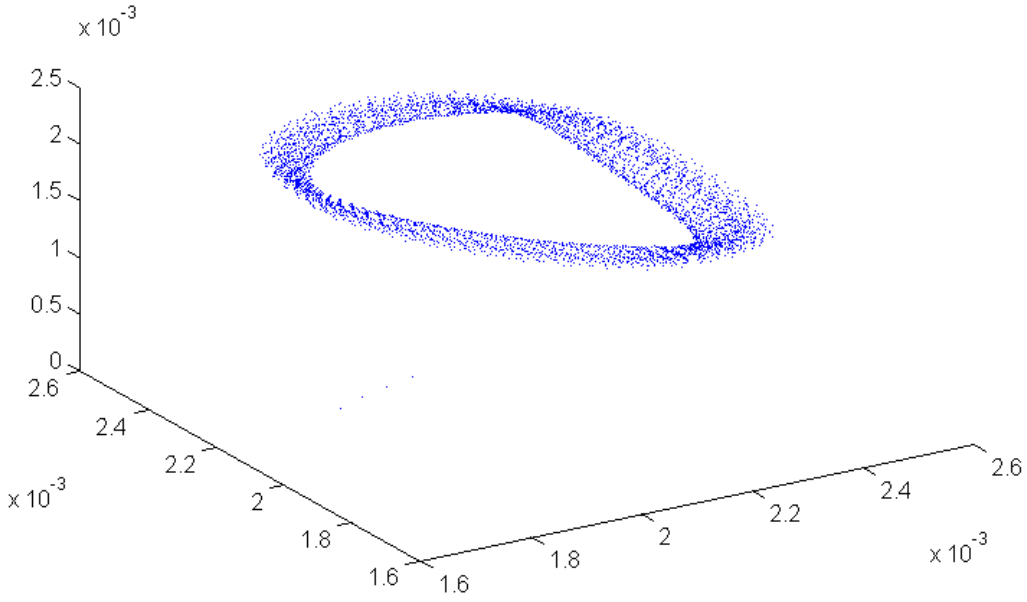

Figure 76: Delay Reconstructed *Attractor* for Load 7, BC3, $\boldsymbol{\lambda_1}$= -0.00291 bits/orbit

The results of the Lyapunov exponent calculations are displayed in Table 13. Positive value Lyapunov exponents indicate chaotic dynamics associated with the *snapback* behavior exhibited by the frame during loading scenarios above the snapping load, or resulting from applying BC2, and are highlighted in bold italic font. Higher positive values correspond to higher levels of chaotic motion.

Table 13: Lyapunov Exponent for Different Applied Loads

Load Number	% of Sea Level Pressure Applied	λ_1 (bits/s)	Dominant Orbital Period (s)	λ_1 (bits/orbit)
1	10	-18.08	6.67e-04	-0.0121
2	20	-16.39	8.33e-04	-0.0137
3	***40****	***10953.2***	***3.54e-04***	***3.8814***
4	***10***	***471.72***	***6.43e-04***	***0.303***
5	***20***	***444.84***	***8.33e-04***	***0.371***
6	***40****	***10051.5***	***1.96e-03***	***19.67***
7	40	-8.269	3.52e-04	-0.00291
8	60	-31.16	3.81e-04	-0.0119

**Above dynamic snapping load for frame determined for the applied load rate*

Summary

An experimental verification of the FEA model was conducted by testing a representable portion of the icosahedron LTAV. The results confirmed the modeling techniques used in Abaqus, and established a segment of the model can be used to determine how the entire structure behaves. A loading rate analysis developed the types of loads that were necessary to produce significant dynamic effects. Also, a *snapping* load was considered for all of the boundary conditions presented in previous research,

beyond which the response of the icosahedron frame becomes erratic and unpredictable. The different methods for determining if chaotic behavior is present in the structure were applied to characterize the response and investigate the *snapback* phenomenon exhibited under certain circumstances.

V. Conclusions and Recommendations

Chapter Overview

The previous chapters in this document have discussed the background, theory, and motivation of LTAVs; developed the techniques necessary to accurately model the icosahedron design; and presented the results of the experiments conducted and simulations run in a dynamic analysis of the structure. This chapter intends to report the important developments that transpired during the research, and the relevance it has in the creation of an icosahedron LTAV.

Conclusions of Research

- Decomposition of the FEA icosahedron structure into individual parts indicates under the properly applied boundary conditions, a single triangle of the complex structure can match the natural frequencies and modes shapes of the entire model. This finding can help cut simulation run times significantly when studying the dynamics of the icosahedron LTAV.
- An equivalent stiffness method was developed to compare the icosahedron frame to simple beam with equal mass. The natural frequencies calculated for the two structures revealed some similarities; however, the mode shapes were not readily comparable, and the method proved to be non-practical.
- A fixed time step of at least 1e-5 seconds is required to study the dynamic response of the icosahedron structure and obtain accurate results. Also, the implicit direct integration method was determined to be the best solution technique for the dynamic problems presented.

- A dynamic response of the icosahedron shaped LTAV requires a dynamically applied load, and is highly dependent on the initial conditions. The magnitude of the load and the rate at which the load is applied was critical in characterizing the response of the structure. Specifically, a pressure of ~35% of Sea Level applied at a rate of 4.053 $MPa\text{-}s^{-1}$ was found to cause a dynamic *snapping* load for all boundary conditions. This *snapping* load occurred at ~45% of Sea Level pressure for the statically applied load, and only occurred for BC1 and BC2.
- The *snapback* displacement seen in the frame was determined to be chaotic behavior confirmed by the Lyapunov exponent calculation and a series of plots shown in Chapter IV. This behavior occurred in BC2 regardless of the load or load rate, indicating significant differences in the response with small changes in initial conditions. The chaotic behavior was present in BC3, but only when the load applied was above the dynamic *snapping* load.
- No chaotic behavior was determined in the frame with skin model. This indicates the membrane increases the strength of the design significantly and it eliminates the instability present with only the frame. Furthermore, the membrane added some measure of damping to the structure which was indicated in the response plots of Chapter IV.
- An experimental triangle was designed, built, and tested that is representative of the icosahedron for both the frame and the frame-skin configurations. The experimental triangle verified the FEA model, and this test will be instrumental in future construction considerations of an icosahedron shaped LTAV.

- Natural Frequencies and mode shapes of the icosahedron shaped LTAV are driven by geometry and boundary conditions, rather than materials and beam cross-section.

Significance of Research

The nonlinear dynamic response related to a complex structure has been evaluated and the computer FEA model used in researching the structure has been verified. An experimental test setup was developed which will allow future design considerations to be tested. Such considerations include the use of composite materials, metals, and plastics, and the method used in tying the frame to the skin. The dynamic behavior exhibited by the icosahedron frame was characterized as chaotic for certain loads and boundary conditions. This development will help establish an operating envelope future vacuum icosahedron LTAVs will have to remain within to prevent collapse.

Recommendations for Future Research

- The experimental triangle analysis was conducted using only one laser vibrometer set up to calculate displacement perpendicular to the plane of the triangle. The use of three laser vibrometers setup to detect displacement in three dimensions would provide more accurate results, and a better correlation to mode shapes could be established. Also, the number of measurement points used in the experimental setup could be increased to better determine higher mode shapes which were undetectable with the number of points used in this research. Finally, the signal input parameters used to calculate the frequency response plots of the

experimental triangle could be better optimized to eliminate any coupling of modes.

- The icosahedron model under consideration did not have any damping associated with it. Adding the membrane to the frame involuntarily incorporates a level of damping to the model, but the addition of a correct damping coefficient for the material under consideration will result in a more accurate response prediction.
- Parameters for the Lyapunov exponent code were selected in a somewhat trial-and-error approach. A parameter study for the Lyapunov exponent calculation would lead to a more accurate final value of the Lyapunov exponent, and therefore give more confidence in the level of chaos present in the system.
- The only loads applied to the structure were sudden pressure loads expected to be applied by evacuating the air out of the structure. However, numerous other loading scenarios will be presented in actual operations of the LTAVs, such as aerodynamics, motor rotational unbalance, and impact with other structures. A dynamic analysis of these loads would develop an understanding of the operating constraints required for the vehicle.

Appendix

This is the Lyapunov exponent calculation code from which all of the exponent convergence plots were created and Table 13 data was developed. The first script, *lyapunov.m*, sends Abaqus dynamic response displacement data to *basegen.m*, *fet.m*, and *search.m*. From the data calculated through those functions, *makeplot.m* and *Lyapunov_expEst.m* are called to produce the final plots desired. These scripts and functions were originally created by Wolf, et al. and modified for the icosahedron analysis with the exception of *Lyapunov_expEst.m* [25]. Additionally, the PSD plot generating code, *PSD.m*, is provided at the end of the Lyapunov code.

lyapunov.m

```
clc; clear all; close all; format compact;

%%%%%%%%%%%%%%%%%%%%%%%%%%%%%%%%%%%%%%%%%%%%%%%%%%%%%%%%%%%%%%%%%%%%%%%%%%%
% Matlab version of the algorithm by Wolf et al. for estimating the
% dominant Lyapunov exponent from a 1-D time series.
%
% Physica 16D (1985) 285-317 "Determining Lyapunov Exponents
% from a Time Series"
% Alan Wolf, Jack B. Swift, Harry L. Swinney, and John A. Vastano
%
% Appendix B of the Physica D article contains Fortran code for a
% concise, but highly inefficient version of the algorithm. I have
% been distributing a Fortran and C version of the efficient version
% of the algorithm since the 1980's. The efficient version of the
% code was converted to Matlab by Taehyeun Park, The Cooper Union,
% EE'15 in September, 2014.
%
% Detailed instructions for the use of this code will be posted at
% Matlab Central's File Exchange.
%%%%%%%%%%%%%%%%%%%%%%%%%%%%%%%%%%%%%%%%%%%%%%%%%%%%%%%%%%%%%%%%%%%%%%%%%%%

% After reporting out xy (displacement/velocity) data from ABAQUS,
% need to save the data of interest as a single column and save as
% a text file to send into basegen
fid = uigetfile('.txt');
% Enter which load case to run calculation for
load_case = str2num(fid(end-5));
rawdata = importdata(fid,' ');
% Cut off the transient response data
```

```
[m,~] = size(rawdata);
time = rawdata(round(0.1*m)+2:end,1);
disp = rawdata(round(0.1*m)+2:end,2);

% input the dominant frequency as calculated using PSD
domFreqs = [1500 1200 2822 1556 1200 511.1 2844 2622];
domFreq = domFreqs(load_case); %Changes for load case
save Disp_Data.txt disp -ASCII
fname = 'Disp_Data.txt';

datcnt = length(disp);
taus = [8 8 80 15 15 150 15 8];
tau = taus(load_case); %Changes for load case
ndim = 3;
ires = 10;
maxbox = 6000;

db = basgen(fname, tau, ndim, ires, datcnt, maxbox);

dt = time(2)-time(1);
evolves = [8 8 80 10 10 80 8 8];
evolve = evolves(load_case); %Changes for load case
dismin = 0.00000001;
dismaxs = [0.0002 0.0002 0.02 0.0002 0.0002 0.02 0.002 0.002];
dismax = dismaxs(load_case); %Changes for load case
thmax = 30;

[out, SUM] = fet(db, dt, evolve, dismin, dismax, thmax);

makeplot(db, out, evolve, 'NorthWest')

[exp_bps,exp_bpo] = lyapunov_expEst(domFreq)
```

basegen.m

```
function db = basgen(fname, tau, ndim, ires, datcnt, maxbox)
% Database generator for fet.m function
% Taehyeun Park, The Cooper Union, EE'15

x = fileread(fname);
data = zeros(1,datcnt);
trck = 1;
start = 1;
fin = 0;

for ii = 1:length(x)
    if strcmp(x(ii), char(32)) || strcmp(x(ii), char(13)) ||
strcmp(x(ii), char(10)) || strcmp(x(ii), char(26))
        if fin >= start
            data(trck) = str2num(x(start:fin));
            trck = trck + 1;
            if trck > 8*floor(datcnt/8)
```

```
                break
            end
        end
        start = ii + 1;
    else
        fin = ii;
    end
end

delay = 0:tau:(ndim-1)*tau;

nxtbox = zeros(maxbox, ndim);
where = zeros(maxbox, ndim);
datptr = zeros(1,maxbox);
nxtdat = zeros(1,datcnt);

datmin = min(data);
datmax = max(data);

datmin = datmin - 0.01*(datmax - datmin);
datmax = datmax + 0.01*(datmax - datmin);
boxlen = (datmax - datmin)/ires;

boxcnt = 1;

for ii = 1:(datcnt-(ndim-1)*tau)
    target = floor((data(ii+delay)-datmin)/boxlen);
    runner = 1;
    chaser = 0;

    jj = 1;
    while jj <= ndim
        tmp = where(runner,jj)-target(jj);
        if tmp < 0
            chaser = runner;
            runner = nxtbox(runner,jj);
            if runner ~= 0
                continue
            end
        end
        if tmp ~= 0
           boxcnt = boxcnt + 1;

           if boxcnt == maxbox
               error('Grid overflow, increase number of box count')
           end

           for kk = 1:ndim
               where(boxcnt,kk) = where(chaser,kk);
           end
           where(boxcnt,jj) = target(jj);
           nxtbox(chaser,jj) = boxcnt;
           nxtbox(boxcnt,jj) = runner;
```

```
            runner = boxcnt;
        end
        jj = jj + 1;
    end
    nxtdat(ii) = datptr(runner);
    datptr(runner) = ii;
end

used = 0;
for ii = 1:boxcnt
    if datptr(ii) ~= 0;
        used = used + 1;
    end
end
display(['Created: ', num2str(boxcnt)]);
display(['Used: ', num2str(used)]);

db.ndim = ndim;
db.ires = ires;
db.tau = tau;
db.datcnt = datcnt;
db.boxcnt = boxcnt;
db.datmax = datmax;
db.datmin = datmin;
db.boxlen = boxlen;

db.datptr = datptr(1:boxcnt);
db.nxtbox = nxtbox(1:boxcnt, 1:ndim);
db.where = where(1:boxcnt, 1:ndim);
db.nxtdat = nxtdat(1:datcnt);
db.data = data;
```

fet.m

```
function [out, SUM] = fet(db, dt, evolve, dismin, dismax, thmax)
% Computes Lyapunov exponent of given data and parameters, generates
output
% textfile, exact replica of Fortran 77 version of fet
% Taehyeun Park, The Cooper Union, EE'15

out = [];

ndim = db.ndim;
ires = db.ires;
tau = db.tau;
datcnt = db.datcnt;
datmin = db.datmin;
boxlen = db.boxlen;

datptr = db.datptr;
nxtbox = db.nxtbox;
where = db.where;
```

```
nxtdat = db.nxtdat;
data = db.data;

delay = 0:tau:(ndim-1)*tau;
datuse = datcnt-(ndim-1)*tau-evolve;

its = 0;
SUM = 0;
savmax = dismax;

oldpnt = 1;
newpnt = 1;

fileID = fopen('fetout.txt', 'w');

goto50 = 1;
while goto50 == 1;
    goto50 = 0;
    [bstpnt, bstdis, thbest] = search(0, ndim, ires, datmin, boxlen,
nxtbox, where, ...
        datptr, nxtdat, data, delay, oldpnt, newpnt, datuse, dismin,
dismax,...
        thmax, evolve);

    while bstpnt == 0
        dismax = dismax * 2;
        [bstpnt, bstdis, thbest] = search(0, ndim, ires, datmin,
boxlen, nxtbox, where, ...
            datptr, nxtdat, data, delay, oldpnt, newpnt, datuse,
dismin, dismax,...
            thmax, evolve);
    end

    dismax = savmax;
    newpnt = bstpnt;
    disold = bstdis;
    iang = -1;

    goto60 = 1;
    while goto60 == 1;
        goto60 = 0;

        oldpnt = oldpnt + evolve;
        newpnt = newpnt + evolve;

        if oldpnt >= datuse
            return
        end

        if newpnt >= datuse
            oldpnt = oldpnt - evolve;
            goto50 = 1;
            break
```

```
        end

        p1 = data(oldpnt + delay);
        p2 = data(newpnt + delay);
        disnew = sqrt(sum((p2 - p1).^2));

        its = its + 1;

        SUM = SUM + log(disnew/disold);
        zlyap = SUM/(its*evolve*dt*log(2));
        out = [out; its*evolve, disold, disnew, zlyap, (oldpnt-evolve),
(newpnt-evolve)];

        if iang == -1
            fprintf(fileID, '%-d\t\t\t%-8.6f\t\t%-8.6f\t\t%-8.6f\n',
out(end,1:4)');
        else
            fprintf(fileID, '%-d\t\t\t%-8.6f\t\t%-8.6f\t\t%-8.6f\t\t%-
d\n', [out(end,1:4), iang]');
        end

        if disnew <= dismax
            disold = disnew;
            iang = -1;
            goto60 = 1;
            continue
        end

        [bstpnt, bstdis, thbest] = search(1, ndim, ires, datmin,
boxlen, nxtbox, where, ...
            datptr, nxtdat, data, delay, oldpnt, newpnt, datuse,
dismin, dismax,...
            thmax, evolve);

        if bstpnt ~= 0
            newpnt = bstpnt;
            disold = bstdis;
            iang = floor(thbest);
            goto60 = 1;
            continue
        else
            goto50 = 1;
            break;
        end
    end
end
fclose(fileID);
```

search.m

```
function [bstpnt, bstdis, thbest] = search(iflag, ndim, ires,
datmin,...
    boxlen, nxtbox, where, datptr, nxtdat, data, delay, oldpnt,
newpnt,...
    datuse, dismin, dismax, thmax, evolve)
% Searches for the most viable point for fet.m
% Taehyeun Park, The Cooper Union, EE'15

target = zeros(1,ndim);
oldcrd = zeros(1,ndim);
zewcrd = zeros(1,ndim);

oldcrd(1:ndim) = data(oldpnt+delay);
zewcrd(1:ndim) = data(newpnt+delay);
igcrds = floor((oldcrd - datmin)./boxlen);
oldist = sqrt(sum((oldcrd - zewcrd).^2));

irange = round(dismin/boxlen);
if irange == 0;
    irange = 1;
end

thbest = thmax;
bstdis = dismax;
bstpnt = 0;

goto30 = 1;
while goto30 == 1
    goto30 = 0;
    for icnt = 0:((2*irange+1)^ndim)-1
        goto140 = 0;
        icounter = icnt;
        for ii = 1:ndim;
            ipower = (2*irange+1)^(ndim-ii);
            ioff = floor(icounter./ipower);
            icounter = icounter - ioff*ipower;
            target(ii) = igcrds(ii) - irange + ioff;

            if target(ii) < 0
                goto140 = 1;
                break;
            end
            if target(ii) > ires-1
                goto140 = 1;
                break
            end
        end

        if goto140 == 1;
```

```
    continue
end

if irange ~= 1
    iskip = 1;
    for ii = 1:ndim
        if abs(round(target(ii) - igcrds(ii))) == irange
            iskip = 0;
        end
    end
    if iskip == 1
        continue
    end
end

runner = 1;
for ii = 1:ndim
    goto80 = 0;
    goto70 = 1;
    while goto70 == 1;
        goto70 = 0;
        if where(runner,ii) == target(ii)
            goto80 = 1;
            break
        end
        runner = nxtbox(runner, ii);
        if runner ~= 0
            goto70 = 1;
        end
    end

    if goto80 == 1
        continue
    end
    goto140 = 1;
    break
end

if goto140 == 1
    continue
end

if runner == 0
    continue
end
runner = datptr(runner);
if runner == 0
    continue
end
goto90 = 1;
while goto90 == 1
    goto90 = 0;
    while 1;
        if abs(round(runner - oldpnt)) < evolve
```

```
                    break
                end
                if abs(round(runner - datuse)) < (2*evolve)
                    break
                end

                bstcrd = data(runner + delay);

                abc1 = oldcrd(1:ndim) - bstcrd(1:ndim);
                abc2 = oldcrd(1:ndim) - zewcrd(1:ndim);
                tdist = sum(abc1.*abc1);
                tdist = sqrt(tdist);
                dot = sum(abc1.*abc2);

                if tdist < dismin
                    break
                end
                if tdist >= bstdis
                    break
                end
                if tdist == 0
                    break
                end
                goto120 = 0;
                if iflag == 0
                    goto120 = 1;
                end
                if goto120 == 0
                    ctheta = min(abs(dot/(tdist*oldist)),1);
                    theta = 57.3*acos(ctheta);
                    if theta >= thbest
                        break
                    end
                    thbest = theta;
                end
                bstdis = tdist;
                bstpnt = runner;
                break;
            end
            runner = nxtdat(runner);

            if runner ~= 0
                goto90 = 1;
            end
        end
    end
    irange = irange + 1;
    if irange <= (0.5 + round((dismax/boxlen)))
        goto30 = 1;
        continue;
    end
    return
end
```

makeplot.m

```
function [] = makeplot(db, out, evolve, loc)
% Plots 2D or 3D attractor evolution by evolution, 4th parameter is the
% location of legend
% Taehyeun Park, The Cooper Union, EE'15

datcnt = db.datcnt;
ndim = db.ndim;
tau = db.tau;
dataplot = [];
freerun = 0;

delay = 0:tau:(ndim-1)*tau;
data = db.data;

for ii = 1:(datcnt-(ndim-1)*tau)
    dataplot = [dataplot; data(ii+delay)];
end

figure, bar(out(:,1),out(:,3)), hold on;
mle = max(dataplot(:)) - min(dataplot(:));
plot([0, out(end,1)], [mle, mle], 'r', 'LineWidth', 1.5), hold off;
set(gca,'YTick', [0, mle])
axis([0, out(end,1), 0, 1.1*mle])
title('d_f of evolutions scaled to the maximum linear extent of the
attractor')

if ndim == 2
    figure('Position', [100, 100, 800, 500]);
    plot(dataplot(:,1), dataplot(:,2), '.', 'MarkerSize', 3), hold on;
    display('To see the next evolution, press enter')
    display('To clear the screen and then see the next evolution, type
c and press enter')
    display('To proceed without stopping, type r and press enter')
    display('To terminate plot generating, type g and press enter')

    for ii = 1:size(out,1)
        if freerun == 0
%             RESET = input('Next evolution?  ', 's');
            RESET = 'g';
            if strcmp(RESET, 'c')
                display('Screen cleared')
                hold off;
                clf;
                plot(dataplot(:,1), dataplot(:,2), '.', 'MarkerSize',
3), hold on;
            elseif strcmp(RESET, 'r')
                display('Evolving without stopping...')
                display('Press ctrl+c to terminate')
                freerun = 1;
```

```
            elseif strcmp(RESET, 'g')
                display('Plot generating stopped')
                return;
            else
                if ii > 1
                    delete(ann)
                end
            end
        end

        tmpold = out(ii,5);
        oldpnt = tmpold + evolve;
        tmpnew = out(ii,6);
        newpnt = tmpnew + evolve;

        plot(data(tmpold:oldpnt), data((tmpold+tau):(oldpnt+tau)), 'r',
'LineWidth', 1);
        plot(data(tmpnew:newpnt), data((tmpnew+tau):(newpnt+tau)), 'g',
'LineWidth', 1);
        for aa = 0:evolve;
            plot([data(tmpold+aa), data(tmpnew+aa)],
[data(tmpold+aa+tau), data(tmpnew+aa+tau)], 'LineWidth', 1)
        end


        ann = legend(['Iteration: ', num2str(out(ii,1)), '/',
num2str(out(end,1)), char(10)...
                      'd_i:', num2str(out(ii,2)), char(10)...
                      'd_f:', num2str(out(ii,3)), char(10)...
                      'Current Estimate:' num2str(out(ii,4))], ...
                      'location', loc);
        if freerun == 1
            drawnow
        end
    end

elseif ndim == 3
    figure('Position', [100, 100, 800, 500]);
    plot3(dataplot(:,1), dataplot(:,2), dataplot(:,3), '.',
'MarkerSize', 3), hold on;
    display('To see the next evolution, press enter')
    display('To clear the screen and then see the next evolution, type
c and press enter')
    display('To proceed without stopping, type r and press enter')
    display('To terminate plot generating, type g and press enter')

    for ii = 1:size(out,1)
        if freerun == 0
%             RESET = input('Next evolution?  ', 's');
            RESET = 'g';
            if strcmp(RESET, 'c')
                display('Screen cleared')
                hold off;
                clf;
```

```
                plot3(dataplot(:,1), dataplot(:,2), dataplot(:,3), '.',
'MarkerSize', 3), hold on;
            elseif strcmp(RESET, 'r')
                display('Evolving without stopping...')
                display('Press ctrl+c to terminate')
                freerun = 1;
            elseif strcmp(RESET, 'g')
                display('Plot generating stopped')
                return;
            else
                if ii > 1
                    delete(ann)
                end
            end
        end

        tmpold = out(ii,5);
        oldpnt = tmpold + evolve;
        tmpnew = out(ii,6);
        newpnt = tmpnew + evolve;

        plot3(data(tmpold:oldpnt), data((tmpold+tau):(oldpnt+tau)),
data((tmpold+(2*tau)):(oldpnt+(2*tau))), 'r', 'LineWidth', 1);
        plot3(data(tmpnew:newpnt), data((tmpnew+tau):(newpnt+tau)),
data((tmpnew+(2*tau)):(newpnt+(2*tau))), 'g', 'LineWidth', 1);
        for aa = 0:evolve;
            plot3([data(tmpold+aa), data(tmpnew+aa)],
[data(tmpold+aa+tau), data(tmpnew+aa+tau)], [data(tmpold+aa+(2*tau)),
data(tmpnew+aa+(2*tau))], 'LineWidth', 1)
        end


        ann = legend(['Iteration: ', num2str(out(ii,1)), '/',
num2str(out(end,1)), char(10)...
                      'd_i:', num2str(out(ii,2)), char(10)...
                      'd_f:', num2str(out(ii,3)), char(10)...
                      'Current Estimate:' num2str(out(ii,4))], ...
                      'location', loc);
        if freerun == 1
            drawnow
        end
    end
end
```

Lyapunov_expEst.m

```
function [LyaExp_b_sec,LyaExp_b_orb] = lyapunov_expEst(domFreq)

close all;
% Mean Orbital Period from PSD
meanPeriod = 1/domFreq;
```

```
% Output data fetout.txt from lyapunov.m code
bitsPerSec_Data = importdata('fetout.txt');
% Estimate of lyapunov exponent for each increment
bitsPerSec_Exp = bitsPerSec_Data(:,8);

i = 1;
ind = 1;
while i <= length(bitsPerSec_Exp)
    if isnan(bitsPerSec_Exp(i)) ~= 1
        BPS(ind) = bitsPerSec_Exp(i);
        ind = ind + 1;
    end
    i = i + 1;
end

BPS = BPS';
bitsPerOrbit = BPS.*meanPeriod;
plot(bitsPerOrbit,'linewidth',2)
hold on; plot([1 length(BPS)],[0 0],'-k')
grid on;
axis([0 length(BPS) -inf inf])

xlabel('Time \rightarrow')
ylabel('Lyapunov Exponent (bits/orbit)')
figureHandle = gcf;
set(findall(figureHandle,'type','text'),'fontSize',18,'fontWeight','bol
d')

LyaExp_b_sec = BPS(end);
LyaExp_b_orb = bitsPerOrbit(end);

end
```

PSD.m

```
data = importdata('60percSL_Icos005Tab_BC3(8).txt');

% Sampling frequency is 1/dt. dt is the time step increment
Fs = 1/1e-5;
% cutoff any transient response data
t = data(502:end,1);
x = data(502:end,2);

N = length(x);
xdft = fft(x);
xdft = xdft(1:N/2+1);
% xdft = xdft(1:round(N/2));
psdx = (1/(Fs*N)) * abs(xdft).^2;
psdx(2:end-1) = 2*psdx(2:end-1);
freq = 0:Fs/length(x):Fs/2;

figure('position',[100 100 1400 875])
```

```
plot(freq,10*log10(psdx),'LineWidth',2)
set(gca,'FontSize',14)
grid on

xlabel('Frequency (Hz)')
ylabel('Power/Frequency (dB/Hz)')
axis([0 10000 -inf inf])
figureHandle = gcf;
set(findall(figureHandle,'type','text'),'fontSize',18,'fontWeight',…
'bold')
```

Bibliography

[1] C. Freudenrich, "HowStuffWorks.com," 26 February 2001. [Online]. Available: http://science.howstuffworks.com/transport/flight/modern/blimp2.htm. [Accessed 16 July 2014].

[2] K. Thompson, "Airship of Dreams: Lighter-Than-Air Travel Is Back," *Popular Mechanics*, vol. 190, no. 11, pp. 88-129, 2014.

[3] "https://www.aiaa.org/SecondaryTwoColumn.aspx?id=5720," 2014. [Online]. [Accessed 15 July 2014].

[4] F. Lana-Terzi, The Aerial Ship, The Aeronautical Society of Great Britain, 1910.

[5] A. M. Akhmeteli and A. V. Gavrilin, "Layered Shell Vacuum Balloons". US Patent 11/127,613, 12 May 2005.

[6] T. T. Metlen, "Design of a Lighter than Air Vehicle that Achieves Positive Buoyancy in Air Using a Vacuum," Air Force Institute of Technology, Wright-Patterson Air Force Base, Ohio, 2013.

[7] R. Adorno-Rodriguez, "Nonlinear Structural Analysis of an Icosahedron and its Application to Lighter than Air Vehicles Under a Vacuum," Air Force Institute of Technology, Wright-Patterson Air Force Base, Ohio, 2014.

[8] A. Bedford and W. Fowler, Engineering Mechanics: Statics (4th ed.), Upper Saddle River, NJ: Pearson Prentice Hall, 2005.

[9] A. Kaplan and Y. C. Fung, "A Nonlinear Theory of Bending and Buckling of Thin Elastic Shallow Spherical Shells," National Advisory Committe for Aeronautics, Washington, 1954.

[10] U.S. Standard Atmosphere, Washington, D.C.: National Aeronautics and Space Administration, 1976.

[11] C. Lee, X. Wei, J. W. Kysar and J. Honel, "Measurement of the Elastic Properties and Intrinsic Strength of Monolayer Graphene," *Science,* vol. 321, no. 5887, pp.

385-388, 2008.

[12] "Applied Nanotech Holdings, Inc.," 2013. [Online]. Available: http://www.appliednanotech.net/tech/graphene_films.php. [Accessed 04 August 2014].

[13] D. J. Inman, Engineering Vibration (3rd ed), Upper Saddle River, New Jersey: Pearson Education, Inc., 2008.

[14] R. D. Cook, D. S. Malkus, M. E. Plesha and R. J. Witt, Concepts and Applications of Finite Element Analysis (4th ed), New York, NY: John Wiley & Sons, Inc., 2002.

[15] N. F. Rieger, "The Relationship Between Finite Element Analysis and Modal Analysis," Stress Technology Incorporated, Rochester, New York.

[16] J. He and Z.-F. Fu, Modal Analysis, Oxford: Butterworth-Heinemann, 2001.

[17] Dassault Syste'mes, *Abaqus Analysis User's Manual,* 2011.

[18] P. Avitable, "Experimental Modal Analysis: A Simple Non-Mathematical Presentation," *Sound and Vibration,* no. January, 2001.

[19] L. Meirovitch, Fundamentals of Vibrations, New York, NY: McGraw-Hill, 2001.

[20] G. L. Baker and J. P. Gollub, Chaotic Dynamics: An Introduction, New York, NY: Cambridge University Press, 1990.

[21] T. Shinbrot, C. Grebogi, J. Wisdom and J. A. Yorke, "Chaos in a Double Pendulum," *American Journal of Physics,* vol. 60, no. 6, p. 491, 1992.

[22] J. P. Crutchfield, J. D. Farmer, N. H. Packard and R. S. Shaw, "Chaos," *Scientific American,* vol. 254, no. 12, pp. 46-57, 1986.

[23] The Wolfram|Alpha Team, "WolframAlpha Blog," Wolfram Alpha LLC, 3 March 2011. [Online]. Available: http://blog.wolframalpha.com/2011/03/03/from-simple-to-chaotic-pendulum-systems-in-wolframalpha/. [Accessed 19 February

2015].

[24] A. E. Forral, "Comparison of the Dynamic Behavior of Composite Plates and Shells Incorporatiing Green's Strain Terms with th von Karman and Donnell Models," Air Force Institute of Technology, Wright-Patterson AFB, OH, 1993.

[25] A. Wolf, J. B. Swift, H. L. Swinney and J. A. Vastano, "Determining Lyapunov Exponents from a Time Series," *Physica D: Nonlinear Phenomena,* vol. 16, no. 3, pp. 285-317, 1985.

[26] Polytec, Inc., *Polytec Scanning Vibrometer, Theory Manual,* Germany: Polytec, Inc..

REPORT DOCUMENTATION PAGE

Form Approved
OMB No. 074-0188

1. REPORT DATE *(DD-MM-YYYY)*	2. REPORT TYPE	3. DATES COVERED *(From – To)*
26-03-2015	Master's Thesis	October 2013 – March 2015

4. TITLE AND SUBTITLE

Dynamic Response Analysis of an Icosahedron Shaped Lighter Than Air Vehicle

5a. CONTRACT NUMBER

5b. GRANT NUMBER

5c. PROGRAM ELEMENT NUMBER

6. AUTHOR(S)

Just, Lucas W., Captain, USAF

5d. PROJECT NUMBER

5e. TASK NUMBER

5f. WORK UNIT NUMBER

7. PERFORMING ORGANIZATION NAMES(S) AND ADDRESS(S)

Air Force Institute of Technology
Graduate School of Engineering and Management (AFIT/ENY)
2950 Hobson Way, Building 640
WPAFB OH 45433-8865

8. PERFORMING ORGANIZATION REPORT NUMBER

AFIT-ENY-MS-15-M-216

9. SPONSORING/MONITORING AGENCY NAME(S) AND ADDRESS(ES)

Dr. David Stargel
875 N. Randolph Street
Suite 325, Room 3112
Arlington VA, 22203-1768
(703)-696-6961 (DSN 426-)

10. SPONSOR/MONITOR'S ACRONYM(S)

AFOSR/RTA

11. SPONSOR/MONITOR'S REPORT NUMBER(S)

12. DISTRIBUTION/AVAILABILITY STATEMENT

Distribution Statement A. Approved for Public Release; Distribution Unlimited.

13. SUPPLEMENTARY NOTES

14. ABSTRACT

The creation of a lighter than air vehicle using an inner vacuum instead of a lifting gas is considered. Specifically, the icosahedron shape is investigated as a design that will enable the structure to achieve positive buoyancy while resisting collapse from the atmospheric pressure applied. This research analyzes the dynamic response characteristics of the design, and examines the accuracy of the finite element model used in previous research by conducting experimental testing. The techniques incorporated in the finite element model are confirmed based on the experimental results using a modal analysis. The experimental setup designed will allow future research on the interaction between the frame and skin of icosahedron like structures using various combinations of materials and construction methods. Additionally, a *snapback* behavior observed in previous static response analysis is further investigated to determine nonlinear instability issues with the design. Dynamic analysis of the structure reveals chaotic motion is present in the frame of the icosahedron under certain loads and boundary conditions. These findings provide information critical to the design of an icosahedron shaped lighter than air vehicle using an inner vacuum.

15. SUBJECT TERMS

finite element analysis, modal analysis, structural analysis, lighter than air vehicles, icosahedron

16. SECURITY CLASSIFICATION OF:			17. LIMITATION OF ABSTRACT	18. NUMBER OF PAGES	19a. NAME OF RESPONSIBLE PERSON
a. REPORT	b. ABSTRACT	c. THIS PAGE			Dr. Anthony Palazotto, AFIT/ENY
U	U	U	UU	145	19b. TELEPHONE NUMBER *(Include area code)* (937) 255-3636 x4599 anthony.palazotto@afit.edu

Standard Form 298 (Rev. 8-98)
Prescribed by ANSI Std. Z39-18